

DISSERTATION

MULTI-FREQUENCY DUAL-POLARIZED PLATFORM FOR VALIDATION OF SATELLITE
PRECIPITATION MEASUREMENTS

Submitted by

Manuel A. Vega

Department of Electrical and Computer Engineering

In partial fulfillment of the requirements

For the Degree of Doctor of Philosophy

Colorado State University

Fort Collins, Colorado

Summer 2017

Doctoral Committee:

Advisor: V. Chandrasekar

Anura Jayasumana

Margaret Cheney

Paul Mielke

Copyright by Manuel A. Vega 2017

All Rights Reserved

ABSTRACT

MULTI-FREQUENCY DUAL-POLARIZED PLATFORM FOR VALIDATION OF SATELLITE PRECIPITATION MEASUREMENTS

Satellite missions such as the Tropical Rainfall Measuring Mission (TRMM) and the Global Precipitation Measurement (GPM) mission have demonstrated the value of rainfall measurements at a global scale. Both missions use a multi-frequency, active/passive (i.e. radar/radiometer) suite of instruments to achieve their measurement goals. Calibration and validation of these instruments has a vital role in the success of the mission since quantitative characterization of precipitation is the primary goal. Furthermore, these missions have also extended the understanding of the synergy between radar/radiometer observations within the atmospheric science community. From a ground validation (GV) perspective, active/passive observations are typically achieved with co-located, but independent instruments. In some cases, this has introduced radio frequency interference (RFI) between adjacent active/passive frequencies of operation, asynchronous scanning strategies and unmatched observation volumes. The work presented focuses on the following topics: 1) engineering aspects in the design of an active/passive remote sensing platform, 2) the design of a solid-state, dual-polarized, multi-frequency, Doppler radar system and performance characterization and 3) calibration approach for a ground based, multi-frequency, radar/radiometer system and first calibrated observations in this mode of operation.

ACKNOWLEDGEMENTS

I would to thank my family for their support and patience throughout this period of our lives. I am grateful to my advisor, Prof. V. Chandrasekar for his guidance and encouragement throughout this work. Dr. Mathew Schwaller, for his support and encouragement. My supervisors throughout this period at the Microwave Instrument and Technology Branch (MITB) at Goddard Space Flight Center (GSFC), Catherine Long, Terence Doiron, Diep Nguyen, Dr. Jeffrey Piepmeier and Jared Lucey, thank you so much for believing in me. Fellow graduate students from the radar design laboratory at CSU, in particular Dr. Robert Beauchamp, Haonan Chen, Dr. Cuong Nguyen and Dr. Joseph Hardin, thank you for your support and many conversations. I am also grateful to the CHILL radar facility and its staff members, Dr. Patrick Kennedy, David Brunkow, Jim George, Dr. Francesc Junyent and Bob Bowie for their support during the integration and testing of the D3R system. Thanks to the GSFC Academic Investment for Mission Success (AIMS) program for its support during the majority of this journey. Last, but not least, there are many friends and colleagues whom I have not mentioned, but I am grateful and acknowledge their support.

DEDICATION

*To my three sons Diego, Sebastian and Matteo whom with their endless love and patience made
this work a reality.*

TABLE OF CONTENTS

ABSTRACT	ii
ACKNOWLEDGEMENTS	iii
DEDICATION	iv
List of Tables	vii
List of Figures	viii
Chapter 1. Dissertation Introduction	1
1.1. Introduction	1
1.2. Problem Statement	2
1.3. Research Questions	2
1.4. Focus of Dissertation	4
1.5. Overview of Dissertation	4
Chapter 2. Background Theory	6
2.1. Introduction	6
2.2. Polarimetric Scattering Covariance Matrix	6
2.3. Weather Radar Signals from Distributed Scatterers	8
2.4. Polarimetric Radar Observables	14
2.5. Passive Microwave Remote Sensing	20
Chapter 3. Radar-Radiometer System: Engineering Aspects in the Design of a Combined Platform	28
3.1. Antennas	28
3.2. Basic receiver architecture	37

3.3. Initial tests using the passive channels on the D3R	43
Chapter 4. Dual-frequency Dual-polarized Doppler Radar System (D3R) - Engineering and Field Performance	48
4.1. Introduction.....	48
4.2. System Architecture	49
4.3. D3R Subsystems	54
4.4. System Calibration	71
4.5. Sample Observations.....	80
4.6. Summary	84
Chapter 5. Multi-frequency Active/Passive Instrument Calibration	88
5.1. Radar calibration	88
5.2. Radiometric channel calibration	105
Chapter 6. Summary, conclusions and future work	126
6.1. Summary and conclusions.....	126
6.2. Future work.....	128
Bibliography	129

LIST OF TABLES

4.1	Specifications of the Dual-frequency, Dual-polarized, Doppler Radar (D3R)	52
-----	---	----

LIST OF FIGURES

2.1	Received voltage due to scattering from random distribution of particles located within a shell extending from r to $r + \Delta r$ and bounded by antenna beam pattern parameters θ_B and ϕ_B and $\vec{r}_k (k = 1, 2, \dots)$ where represents the particle locations with respect to the radar.	9
2.2	Complex plane plot of "instantaneous" summation of individual particle contributions to $V_R(t)$	9
2.3	Illustration of the continuous range-time axis (τ) and the discrete sample-time axis t_s . Adapted from Bringi and Chandrasekar (2001)	10
2.4	Probability density function for normalized amplitude ratio u for various values of $ \rho_{co} $. 13	13
2.5	Joint probability density function of phases θ_v and θ_h in terms of phase difference $\theta_v - \theta_h - \bar{\theta}_0$ for various values of $ \rho_{co} $	14
2.6	Spectral brightness B_f from Planck's black-body radiation law for $T = 300, 150$ and $75K$	21
2.7	Spherical coordinate system showing definition of differential solid angle $d\Omega$. Azimuth ($\theta = 90 \text{ deg}$) and elevation ($\phi = 45 \text{ deg}$) planes shaded in light grey.	25
2.8	Atmospheric gas, oxygen plus water vapor, absorption coefficient for water vapor content of 7.5 gm^{-3} , surface level temperature and pressure of 290 K and 1013 mbar respectively.	26
2.9	Simulated brightness temperatures from 10 to 1000 GHz for five atmospheric and cloud conditions (from Hou et al. (2008)).	27
3.1	Depiction of antenna side lobe contributions to main lobe brightness temperature.	30

3.2	Antenna side lobe contribution to main lobe brightness temperature based on beam efficiency η_b and side lobe scene brightness temperature.	31
3.3	Ku-band wide angle (A) and narrow (B) measured and modeled co-polarized H-port principal plane patterns.	33
3.4	Ka-band wide angle (A) and narrow (B) measured and modeled co-polarized H-port principal plane patterns.	34
3.5	Ku-band (A), Ka-band (B) antenna high resolution models from combination of simulations using HFSS and GRASP.	35
3.6	Ku-band antenna model resolution effect on beam efficiency computation. Colorbar represents the ratio $\Omega_m(4\pi)^{-1}$	36
3.7	Antenna self emission contribution to main lobe temperature with estimated D3R Ku and Ka radiation efficiency ξ and beam efficiency η_b bounds.	37
3.8	Superheterodyne receiver configuration for total-power radiometer measurements.	38
3.9	Ku (A) and Ka-band (B) receiver Allan variance for zenith pointing data collection.	44
3.10	Ku-band reflectivity Z (a) and passive channel system temperature T_{SYS} in total-power mode (b) for a PPI scan at elevation angle of 2.36 deg on June 11th, 2014 at 17:42:31 UTC.	46
3.11	Ku-band reflectivity Z (a) and passive channel system temperature T_{SYS} in total-power mode (b) for a PPI scan at elevation angle of 5.27 deg on June 11th, 2014 at 17:42:57 UTC.	47
4.1	D3R system deployed in North Carolina for IPHEX GPM-GV field campaign.	53
4.2	D3R system architecture diagram.	54
4.3	Ku, Ka-band H-port antenna co-polarized power (normalized) antenna patterns.	56

4.4	Ku-band H and V port antenna co- and cross-polarized power (normalized) antenna patterns for worst case cross-polarization plane.	57
4.5	Ka-band H and V port antenna co- and cross-polarized power (normalized) antenna patterns for worst case cross-polarization plane.	58
4.6	Ku-band differential phase (normalized) antenna patterns for $\phi = 0, 45, 90$ and 135 degree planes.	59
4.7	Ka-band differential phase (normalized) antenna patterns for $\phi = 0, 45, 90$ and 135 degree planes.	60
4.8	Ku, Ka-band transceiver architecture block diagram.	61
4.9	System timing and clock generation block diagram.	64
4.10	D3R software system diagram. Dark gray boxes represent hardware or firmware devices. Light gray boxes represent software modules running on general purpose servers.	65
4.11	Ku-band pulse compression waveform and filter response for the medium pulse illustrating range sidelobes.	68
4.12	Ka-band pulse compression waveform and filter response for the medium pulse illustrating range sidelobes.	69
4.13	D3R pulse schemes for simultaneous mode with both uniform PRT (A) and staggered two-thirds PRT (B). The uniform PRT and staggered two-thirds PRT waveforms yield the same effective sampling rate over a ray integration cycle. The alternate mode staggered PRT pulse timing for D3R is illustrated in (C).	70
4.14	D3R real-time display control panel. Two control panels are provided; one for Ku and one for Ka.	72
4.15	Example real-time display of Ku-band reflectivity for an RHI scan.	72

4.16	Ku- (left) and Ka-band (right) solar received power with position relative to the center of the sun.	74
4.17	3 dB contour lines of the 5 parameter model fitted to the Ku- and Ka-band solar received power. The azimuth and elevation are relative to the center of the sun during the scan. This plot provides information on the absolute pedestal position error as well as co-alignment of the Ku and Ka antennas.	74
4.18	Conductive sphere radar cross section at D3R wavelengths.....	76
4.19	Ku-band sphere calibration from June 14th, 2013 starting at 00:00UTC. The graph shows measured sphere reflectivity and the theoretical reflectivity curve of a metal sphere of the same diameter. No corrections were made to this data based on calibration results.	76
4.20	Ka-band sphere calibration from June 14th, 2013 starting at 00:00UTC. The graph shows measured sphere reflectivity and the theoretical reflectivity curve of a metal sphere of the same diameter. No corrections were made to this data based on calibration results.	77
4.21	Ku-band short-pulse observed Z_{dr} vs. azimuth angle on 2013-05-04 at 07:09 UTC during a vertically pointing scan. Z_{dr} observations are from a height of 1.8 km above the radar. The mean $ \rho_{hv} $ of observation is 0.994. The Z_{dr} mean is 0.4359 dB and standard deviation is 0.1784 dB.	79
4.22	Ka-band short-pulse observed Z_{dr} vs. azimuth angle on 2013-05-04 at 07:09 UTC during a vertically pointing scan. Z_{dr} observations are from a height of 1.8 km above the radar. The mean $ \rho_{hv} $ of observation is 0.993. The Z_{dr} mean is 0.3439 dB and standard deviation is 0.0755 dB.....	80

4.23	Ku- and Ka-band observations collected on May 8th, 2013 at 21:53 UTC. Panels are arranged with Ku-band products on the left and Ka-band on the right. Panels (a) and (b) show measured reflectivity's, (c) and (d) show mean Doppler velocities, (e) and (f) show differential reflectivities, finally, (g) and (h) show the magnitude of the co-polar correlation coefficient.	82
4.24	Ku- and Ka-band PPI observations collected on May 19th, 2013 at 09:18 UTC of a line of convection. Panels are arranged with Ku-band products on the left and Ka-band on the right. Panels (a) and (b) show measured reflectivities, (c) and (d) show differential phase, (e) and (f) show differential reflectivities, finally, (g) and (h) show the magnitude of the co-polar correlation coefficient.	83
4.25	Ku (a) and Ka-band (b) Z_h standard deviation as a function of integration time for the short-pulse (SC) and medium-pulse (MC) channels.....	85
4.26	Ku (a) and Ka-band (b) Z_{dr} standard deviation as a function of integration time for the short-pulse (SC) and medium-pulse (MC) channels.	85
4.27	Ku (a) and Ka-band (b) $ \rho_{hv} $ standard deviation as a function of integration time for the short-pulse (SC) and medium-pulse (MC) channels.....	86
4.28	Ku (a) and Ka-band (b) ϕ_{dp} standard deviation as a function of integration time for the short-pulse (SC) and medium-pulse (MC) channels.....	86
4.29	Ku (a) and Ka-band (b) histograms of measured $ \rho_{hv} $	87
5.1	Trihedral corner reflector model showing inside edge dimension, simulation coordinate system and spatial pattern cuts computed from Marrero (2015a).	91

5.2	Ku (A) and Ka (B) 6.4 inch trihedral corner reflector HFSS simulation results ($\phi = (0, 350)$ in 10 deg increments) for co (solid lines) and cross-polarized (dashed lines) cross sections from Marrero (2015a)	92
5.3	Radar calibration setup at Wallops Flight Facility. D3R system indicated by yellow pin on top and calibration tower located at bottom yellow pin.	94
5.4	Radar calibration tower at Wallops Flight Facility. Target height is approximately 30 meters.	95
5.5	Calibration error bounds vs signal to clutter ratio. Equivalent result to that shown in Bharadwaj et al. (2011)	96
5.6	Ku (A) and Ka (B) maximum reflectivity observations from calibration exercise at WFF April, 2015.	97
5.7	DFRm vs Z_{Ku} histogram for beginning of snow event in February 26th, 2015 using RHI observations from 06:00 to 06:16 UTC.	98
5.8	Sample of Ku reflectivity (left) and Ku/Ka measured dual-frequency ratio (DFRm) (right) RHIs for snow event in February 26th, 2015. Used to generate histogram.	99
5.9	Ku (top) and Ka (bottom) Doppler velocity from calibration exercise. Note a slight mean negative bias $< 0.05m.s^{-1}$ for both systems.	100
5.10	Ku (top) and Ka (bottom) spectral width from calibration exercise.	101
5.11	Ku (top) and Ka (bottom) $ \rho_{HV} $ from calibration exercise. Both systems exhibit a mean $ \rho_{HV} \approx 0.999$	102
5.12	Ku (top) and Ka (bottom) ϕ_{dp} from calibration exercise.	103
5.13	Ku (top) and Ka (bottom) Z_{dr} from calibration exercise.	104

5.14	Seasonal zenith mean radiating temperature T_{mr} from radiosonde soundings at D3R frequencies. Ku-band (top) and Ka-band (bottom). Seasons defined as: spring - March 1st to May31st, summer - June 1st to August 31st, fall - September 1st to November 30th and winter - December 1st to February 28th or 29th.....	111
5.15	GOES-13 or East visible image for April 20th, 2016 at 16:00 UTC.	112
5.16	D3R transceiver system thermal zones.	113
5.17	Ku (A) and Ka-band (B) RF front-end component temperatures during tipping curve calibration experiment at WFF April, 2016.	114
5.18	Ku (A) and Ka-band (B) H and V polarized channel linear fit parameters derived from tipping curve calibration experiment at WFF April, 2016.	117
5.19	Ku (A) and Ka-band (B) H and V polarized channel calibration functions, $r_H(t)$ and $r_V(t)$, derived from tipping curve calibration experiment at WFF April, 2016.	118
5.20	Ku (A) and Ka-band (B) H and V polarized channel brightness temperatures after calibration.	119
5.21	Ku (A) and Ka-band (B) H and V polarized channel calibrated brightness temperatures derived from tipping curve calibration experiment at WFF April, 2016.	120
5.22	Ku (A) and Ka-band (B) RF front-end component temperatures during April 22-23rd, 2016 event.	121
5.23	Ku reflectivity, H and V polarized brightness temperatures, kurtosis and skewness for April 22-23rd, 2016 case. Passive channel calibration function derived from system temperatures and neural network.	122

5.24	Ka reflectivity, H and V polarized brightness temperatures, kurtosis and skewness for April 22-23rd, 2016 case. Passive channel calibration function derived from system temperatures and neural network.	123
5.25	Ku reflectivity, measured dual-frequency ratio (DFRm), Ku H and Ka HV polarized brightness temperatures for April 22-23rd, 2016 case.	124
5.26	Ku, and Ka differential phase and Ku H and Ka HV polarized brightness temperatures for April 22-23rd, 2016 case.	125

CHAPTER 1

DISSERTATION INTRODUCTION

1.1. INTRODUCTION

Characterization of the space-time variability of precipitation at a global scale plays a vital role in understanding the impacts of climate change in the global energy and water cycle (GWEC) [Hou et al. \(2008\)](#). For decades, distributed in situ sensor networks such as tipping bucket rain gauges and radar networks have provided high time resolution precipitation measurements. However, these are not practical in providing oceanic or global coverage. For these reasons, space borne measurements remain as the primary method of achieving global coverage.

The work described in this document is aimed primarily towards ground-based precipitation measurements in support of the Global Precipitation Measurement (GPM) mission Ground Validation (GV). To this date, several combined radar-radiometer airborne and space-based instrument systems such as the Tropical Rain Measurement Mission (TRMM) and GPM have been developed for precipitation measurements. More importantly, the scientific community has highlighted the synergistic value of combined radar-radiometer datasets in precipitation estimation ([Meneghini et al. \(1997\)](#), [Marzano et al. \(1999\)](#), [Skofronick-Jackson et al. \(2003\)](#), [Grecu and Anagnostou \(2008\)](#), [Grecu and Olson \(2008\)](#), [Olson et al. \(2010\)](#), [Saavedra et al. \(2012\)](#)). However, a limited amount of work has been done in the development of a combined ground-based platform. A clear division among the ground-based radar and radiometer communities seems present. Consequently, a major focus of this work is in the definition a of combined radar-radiometer instrument platform for ground-based precipitation measurements.

1.2. PROBLEM STATEMENT

The ideal radar-radiometer system would perform co-incident precipitation measurements of matched volumes at multiple frequency bands, especially on the radiometric side, with high spatial resolution. However, meeting all of these goals, would lead to a complex and unpractical system design. Mainly, since an adequate single antenna design with sufficient bandwidth to cover all desired bands, possessing high beam efficiency, and matched beams would be very difficult to achieve. This work focuses on the development of efficient (with respect to size and complexity) system design concepts for a combined multi-frequency radar-radiometer platform for ground-based precipitation measurements in support of GPM GV and future cloud missions.

Historically, when ground-based active passive measurements of precipitation measurements are needed, individual radar and radiometer systems are co-located in the field. Typical limitations arising from this development/deployment approach are: unsynchronized sampling and scanning, unmatched beams resulting from a completely separate design approach not considering combined retrievals, parallax errors resulting from large instrument baseline separation and radio frequency interference (RFI) of systems which may not have been tested together previously. Many of these issues can be minimized if not completely mitigated if both platforms are combined and designed as one.

1.3. RESEARCH QUESTIONS

The Dual-frequency Dual-polarized Doppler Radar (D3R) system has been designed as a Ku, Ka-band dual-polarized system which provides the redundant capability of estimating two parameters of the drop size distribution (DSD) through Ku-band polarimetry and dual-frequency algorithms. However, the operation at shorter wavelengths also gives rise to the problem of attenuation correction of received power derived products such as reflectivity and differential reflectivity. The main contributors to the attenuation problem are: 1) the precipitation filled medium, 2) atmospheric

water vapor, and 3) cloud liquid water (CLW) content. At Ku-band, the differential phase obtained from polarimetric measurements provides a good method for precipitation attenuation correction; water vapor may be neglected in many cases but CLW also attenuates the signal as it propagates through clouds with very low backscatter signals produced due to the size of the water particles. At Ka-band, the problem becomes more complex since the presence of Mie scattering complicates the use differential phase in the correction of attenuation [Baldini et al. \(2012\)](#) due to precipitation and water vapor as well as CLW both make significant contributions to the total attenuation. These items lead to the following questions with regards to a ground-based system that would provide a means for the study of these effects through long term observations that are difficult to achieve with airborne system.

- (1) What radiometric frequencies could be added to the existing D3R system to gain sensitivity to both water vapor and CLW?
- (2) How can these be added to the system in a practical way that makes for a robust and easily deployable system?

Architecture: shared aperture and receivers, shared aperture and separate receivers, dual-polarized?

What RFI mitigation and detection methods will be used?

- (3) What are suitable characterization, operational and calibration methods for such an instrument (e.g. sphere, tipping curve, light stratiform precipitation, vertically pointing scans for calibration)?

1.4. FOCUS OF DISSERTATION

The focus of this dissertation can be divided into three main topics 1) engineering aspects in the design of an active/passive remote sensing platform, 2) the design of a solid-state, dual-polarized, multi-frequency, Doppler radar system and performance characterization and 3) calibration approach for a ground based, multi-frequency, radar/radiometer system and first calibrated observations in this mode of operation.

1.5. OVERVIEW OF DISSERTATION

Chapter 2 begins by providing a review of polarimetric Doppler weather radar measurements. The polarimetric scattering covariance matrix is presented as well as a description of the statistics of signals received from hydrometeors and the definition of typical products measured by such radar systems. The following sections provide a review of the area of passive remote sensing of the atmospheric constituents. It begins by stating Planck's radiation law and approximations valid for lower and upper regions of the spectrum. The explanation of grey-body radiation and the power-temperature correspondence follows. Finally, examples on the emissions from atmospheric constituents such as water vapor, oxygen and hydrometeors are provided with remarks on how these are modeled.

The design and engineering performance of the D3R system is covered in chapter 4. It begins with a brief description of the GPM mission and the role of the D3R instrument within the GPM GV program. The instrument architecture and reasoning behind the decisions made are presented followed by detailed descriptions of each subsystem. Finally, sample observations, calibration results and validation of errors in measurement estimates are presented.

Engineering aspects in the design of a combined radar-radiometer are covered in chapter 3. The difference between the antenna weighting function between radar and radiometer observations is explained. Emphasis is put into the impact of antenna radiation and beam efficiencies on

brightness temperature measurements along with a discussion on practical issues in determining these parameters. The superheterodyne receiver is described within the context of a total-power radiometer. Finally, initial measurements using the D3R system as a shared-aperture active/passive instrument is presented with a short discussion of preliminary results.

Chapter 5 discusses absolute radar calibration using a point target of known cross section and the tipping curve calibration approach for the radiometric channels. The radar calibration section describes the experimental setup at Wallops Flight Facility (WFF) consisting of 30 meter tower equipped with a trihedral corner reflector. Electromagnetic simulation results of radar cross section for the trihedral corner reflector employed are presented. Finally the calibration results are presented and tested against theoretical simulations of snow particles using observations of DFRm in snow. On the passive side, the tipping curve method is explained and applied to the D3R system. Consistency checks on the calibration results are presented and verified against clear air brightness temperatures derived from soundings. The application of a neural network to predict the system calibration based on system temperatures is discussed with performance results on the training of the net. Kurtosis and skewness calculations are also included to aid in the detection of radio frequency interference (RFI). Finally data from a rain event is presented and results discussed.

Chapter 6 closes the dissertation with a summary of results, conclusions and future work.

CHAPTER 2

BACKGROUND THEORY

2.1. INTRODUCTION

This chapter summarizes some of the theory behind dual-polarized radar and radiometric measurements. It can be divided into two main areas; radar and radiometric remote sensing of atmospheric constituents. Sections 2.2 to 2.4 cover the radar side while section 2.5 covers the radiometric side. It is intended as a review of concepts to be used in the following chapters.

2.2. POLARIMETRIC SCATTERING COVARIANCE MATRIX

In essence, polarimetric Doppler weather radar systems provide estimates of the full or a subset of the full backscattering matrix $\Sigma_{\mathbf{F}}$, of a volume containing an ensemble of scatterers [Bringi and Chandrasekar \(2001\)](#)

$$(1) \quad \Sigma_{\mathbf{F}} = \left\langle \begin{bmatrix} |S_{hh}|^2 & S_{hh}S_{hv}^* & S_{hv}S_{hh}^* & |S_{hv}|^2 \\ S_{hh}S_{vh}^* & S_{hh}S_{vv}^* & S_{hv}S_{vh}^* & S_{hv}S_{vv}^* \\ S_{vh}S_{hh}^* & S_{vh}S_{hv}^* & S_{vv}S_{hh}^* & S_{vv}S_{hv}^* \\ |S_{vh}|^2 & S_{vh}S_{vv}^* & S_{vv}S_{vh}^* & |S_{vv}|^2 \end{bmatrix} \right\rangle$$

where the angle braces represent the ensemble average over particle states (i.e. size, shape, orientation) within the observation volume. In the case of weather radar systems, the particles of interest are hydrometeors which consist of water generated as a product of condensation or deposition of atmospheric water vapor.

In $\Sigma_{\mathbf{F}}$ is defined as the Kronecker product $\langle \mathbf{S} \otimes \mathbf{S}^* \rangle$ of the scattering matrix \mathbf{S}_{BSA} (or Sinclair matrix), [Wang et al. \(2006\)](#), defined in 2, using the H-V linear polarization basis and where

the subscript BSA represents the backscatter alignment convention. The matrix \mathbf{S}_{BSA} serves the purpose of relating the incident and scattered fields $\mathbf{E}^r = \mathbf{S}_{\text{BSA}}\mathbf{E}^i$ (spherical wave factor dropped), in matrix form in 3 from [Bringi and Chandrasekar \(2001\)](#). It is worth mentioning that the definition of \mathbf{S}_{BSA} is consistent with the Stokes' vector definition of an electromagnetic wave, where the Mueller matrix \mathbf{M} serves the same purpose of \mathbf{S}_{BSA} , which is to relate the incident and scattered fields. [Mott \(1992\)](#) shows the the Mueller matrix \mathbf{M} in terms of the elements of the scattering matrix \mathbf{S}_{FSA} (forward scattering alignment) which is directly related to the matrix \mathbf{S}_{BSA} (shown in 2). [Bringi and Chandrasekar \(2001\)](#) also show the scattered Stokes' vector in terms of the matrix \mathbf{R} (\mathbf{Q} in [Mott \(1992\)](#)) and a vector containing elements of the coherency matrix \mathbf{J} defined in [Born and Wolf \(2002\)](#).

$$(2) \quad \mathbf{S}_{\text{BSA}} = \begin{bmatrix} S_{hh} & S_{hv} \\ S_{vh} & S_{vv} \end{bmatrix} = \begin{bmatrix} -1 & 0 \\ 0 & 1 \end{bmatrix} \mathbf{S}_{\text{FSA}}$$

$$(3) \quad \begin{bmatrix} E_h^r \\ E_v^r \end{bmatrix} = \begin{bmatrix} S_{hh} & S_{hv} \\ S_{vh} & S_{vv} \end{bmatrix}_{\text{BSA}} \begin{bmatrix} E_h^i \\ E_v^i \end{bmatrix}$$

[Tragl \(1990\)](#) shows that for targets that exhibit reciprocity (i.e. $S_{hv} = S_{vh}$), a reduced, 3 x 3 matrix Σ , represented as the outer product $\langle \Omega \otimes \Omega^* \rangle$ (i.e. covariance matrix) of a "feature" vector $\Omega = [S_{hh}\sqrt{2}S_{hv}S_{vv}]^T$ can be used in the derivation of the polarization dependence of averaged scattered power and signal correlations. Σ is conjugate symmetric (i.e. Hermitian) and composed of nine independent parameters, three real and corresponding to P_{hh} , $2P_{hv}$ and P_{vv} and six complex inter-channel correlation coefficients that fully characterize the polarimetric response of a target (in this case hydrometeors).

$$(4) \quad \Sigma = \left\langle \begin{bmatrix} |S_{hh}|^2 & \sqrt{2}S_{hh}S_{hv}^* & S_{hh}S_{vv}^* \\ \sqrt{2}S_{hv}S_{hh}^* & 2|S_{hv}|^2 & \sqrt{2}S_{hv}S_{vv}^* \\ S_{vv}S_{hh}^* & \sqrt{2}S_{vv}S_{hv}^* & |S_{vv}|^2 \end{bmatrix} \right\rangle$$

2.3. WEATHER RADAR SIGNALS FROM DISTRIBUTED SCATTERERS

2.3.1. Single Polarized Weather Radar Signals

The signal received from a single point scatterer moving at a fixed velocity for a single polarized weather radar system (typically horizontally polarized), is essentially a scaled copy of the transmitted waveform, $U_{tr}(t)$, with the addition of a time delay associated with the range to the target (t_0) and frequency shift associated with the Doppler effect ($f_D = -2\hat{i} \cdot \vec{v} / \lambda$) where \hat{i} is a unit vector in the direction of incidence, \vec{v} is the scatterer velocity vector and λ is the wavelength [Brangi and Chandrasekar \(2001\)](#). In general, the observation volume is composed of a random collection of point scatterers with a wide range of backscatter cross-sections and with different velocities as depicted in [2.1](#). The resultant received voltage $V_r(t)$ from the precipitation volume can be written as a sum of contributions from individual hydrometeors, shown in [2.2](#), as

$$(5) \quad V_r(t) = \sum_k A_k(\tau_k; t) e^{-j2\pi f_0 \tau_k} U_{tr}(t - \tau_k)$$

where A_k is the backscattering amplitude of the k^{th} particle and $U_{tr}(t)$ is the transmitted waveform.

As depicted in [figure 2.2](#), the resultant voltage $V_r(t)$ is complex with components $I + jQ$, where I and Q are the in-phase and quadrature components. For a uniform train of equally-spaced pulses with N number of pulses and at a pulse repetition time (PRT) of T_s , the received voltage at

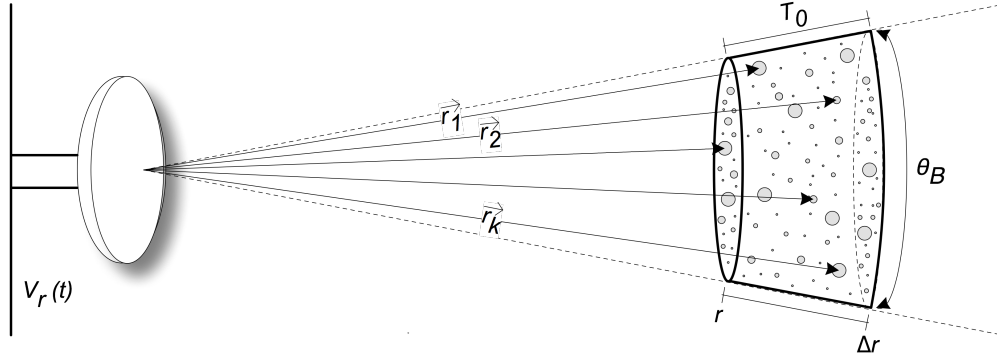


FIGURE 2.1. Received voltage due to scattering from random distribution of particles located within a shell extending from r to $r + \Delta r$ and bounded by antenna beam pattern parameters θ_B and ϕ_B and $\vec{r}_k (k = 1, 2, \dots)$ where represents the particle locations with respect to the radar.

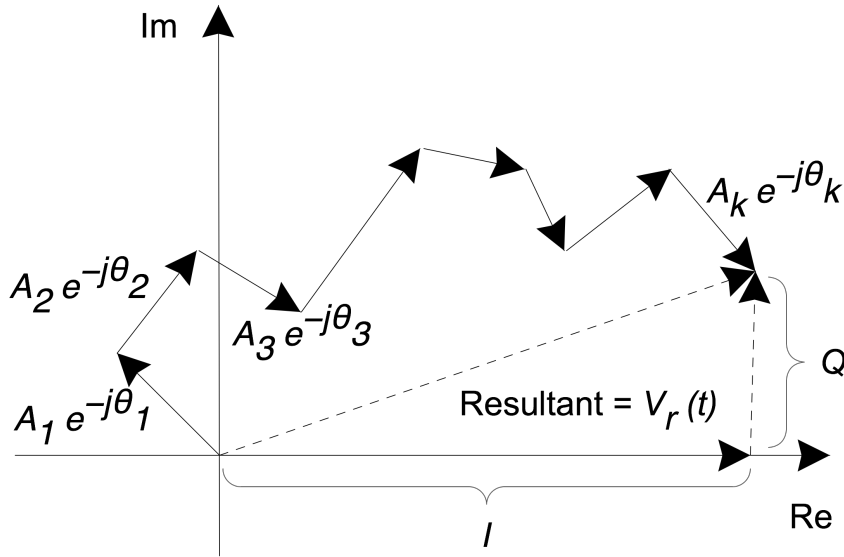


FIGURE 2.2. Complex plane plot of "instantaneous" summation of individual particle contributions to $V_R(t)$.

the same range-time (τ) can be written as $V_r(t = \tau), V_r(t = \tau + T_s), V_r(t = \tau + 2T_s), \dots, V_r(t = \tau + (N - 1)T_s)$, shown in 2.3. Now, let $\mathbf{v} = [v(1)v(2)v(3)\dots v(N)]^T$ represent the temporal sequence of N samples from the same resolution volume and assume that \mathbf{v} is a circular (i.e. complex random variable with uniform phase distribution [Schreier and Scharf \(2010\)](#)) complex Gaussian random vector $\mathcal{N}(0, \mathbf{R})$ with a multivariate probability density function given by

$$(6) \quad f(\mathbf{v}) = \frac{1}{\pi^N \det \mathbf{R}} \exp(-\mathbf{v}^H \mathbf{R}^{-1} \mathbf{v})$$

where $\mathbf{R} = \mathbb{E}[\mathbf{v}\mathbf{v}^H]$ is the covariance matrix of the complex vector \mathbf{v} and $\mathbb{E}[\cdot]$ is the expectation operator [Chandrasekar and Bharadwaj \(2010\)](#). The amplitudes of the voltages $V_r(t)$ and powers $P_r(t)$ will have the corresponding distributions derived from the complex voltage (Rayleigh and exponential distributions respectively).

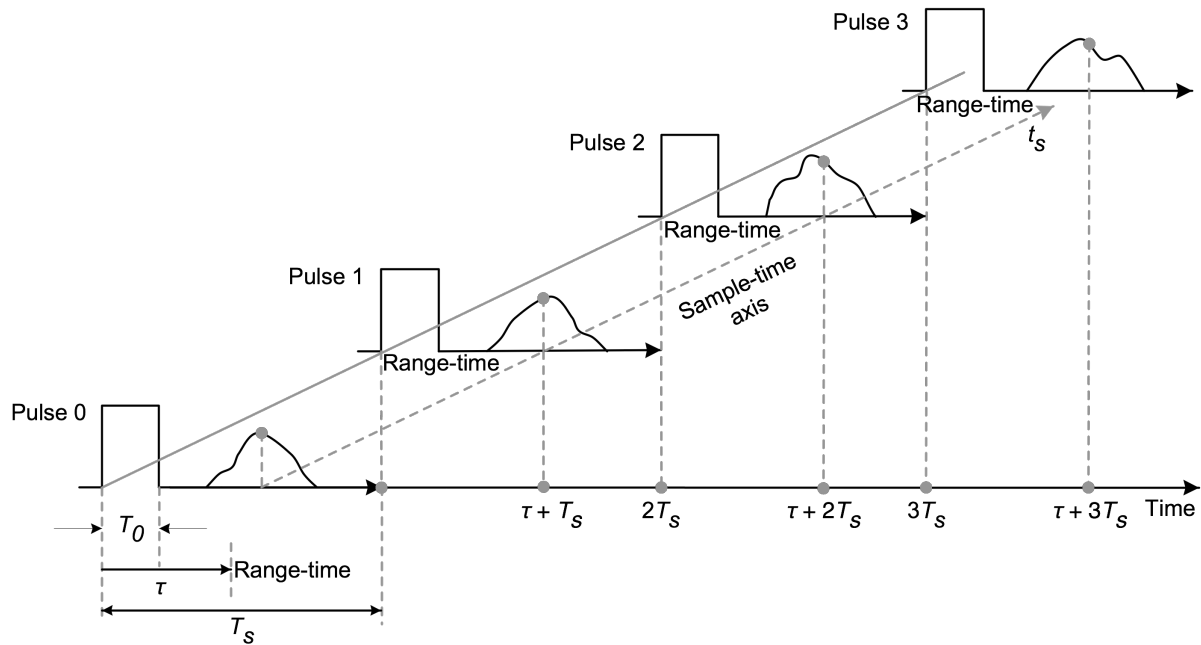


FIGURE 2.3. Illustration of the continuous range-time axis (τ) and the discrete sample-time axis t_s . Adapted from [Bringi and Chandrasekar \(2001\)](#).

2.3.2. Dual-Polarized Weather Radar Signals

In the previous section, a general description of the signal received from a single polarized Doppler (i.e. coherent) weather radar was described in terms of a sequence of temporal samples from a volume containing a random distribution of particles with different range and velocity with respect to

the radar system. Within this framework, expressions for the received signal along with underlying statistics were given. This section will now focus on the signals received in a dual-polarized Doppler weather radar and their statistical properties.

The single polarized weather radar equation is a well established scalar equation and therefore its derivation is left to the reader to review if desired. [Doviak and Zrnice \(2006\)](#) and [Bringi and Chandrasekar \(2001\)](#) are both good references which cover the subject. In the case of a dual-polarized system, the weather radar equation can be written in matrix form as

$$(7) \quad \begin{bmatrix} v_h \\ v_v \end{bmatrix} = \frac{\lambda\sqrt{P_t}G}{4\pi r^2} [\mathbf{T}][\mathbf{S}_{\text{BSA}}][\mathbf{T}] \begin{bmatrix} M_h \\ M_v \end{bmatrix}$$

where \mathbf{T} is the transmission matrix which is included twice to account for 2-way propagation effects through the medium, \mathbf{S}_{BSA} is the backscattering matrix defined in 2, M_h and M_v are the transmitter excitation states of a dual-polarized antenna with horizontal (h) and vertically (v) polarized ports, P_t is the transmit power, G is the antenna power gain (ideal antenna), λ is the wavelength and r is the range to the target.

In a system possessing polarization agility (i.e. pulse to pulse polarization switching capability or also known as alternating mode) the excitation vectors would look like

$$(8) \quad \begin{bmatrix} M_h \\ M_v \end{bmatrix} = \begin{bmatrix} 1 \\ 0 \end{bmatrix} \text{ and } \begin{bmatrix} M_h \\ M_v \end{bmatrix} = \begin{bmatrix} 0 \\ 1 \end{bmatrix}$$

where the left side represents the "firing" of the h polarized transmitter and the right side represents the "firing" of the v polarized channel. In the case where co and cross-polarized signals can all be sampled simultaneously, the following sequence of voltages would be retrieved.

$$(9) \quad z = \begin{bmatrix} v_{hh} & v_{vh} & v_{hv} & v_{vv} \end{bmatrix}^T$$

where the notation v_{xx} , for example v_{hh} and v_{vh} represent the horizontal-transmit/horizontal-
receive and horizontal-transmit/vertical-receive configuration states.

The corresponding covariance matrix, [Bringi and Chandrasekar \(2001\)](#), can be defined as

$$(10) \quad E(zz^H) = E \begin{bmatrix} |v_{hh}|^2 & v_{hh}v_{vh}^* & v_{hh}v_{hv}^* & v_{hh}v_{vv}^* \\ v_{vh}v_{hh}^* & |v_{vh}|^2 & v_{vh}v_{hv}^* & v_{vh}v_{vv}^* \\ v_{hv}v_{hh}^* & v_{hv}v_{vh}^* & |v_{hv}|^2 & v_{hv}v_{vv}^* \\ v_{vv}v_{hh}^* & v_{vv}v_{vh}^* & v_{vv}v_{hv}^* & |v_{vv}|^2 \end{bmatrix}$$

which collapses from a 4 x 4 to a 3 x 3 matrix if reciprocity is invoked (i.e. $v_{hv} = v_{vh}$) as a result of correspondence to the backscattering covariance matrix Σ defined in 4.

The probability density function for both the amplitude ratio of simultaneously received co-polarized amplitudes and phase difference are shown in [Bringi and Chandrasekar \(2001\)](#) and repeated in 2.4 and 12. Both of these quantities are relevant to differential reflectivity and phase measurements which are two key observables in dual-polarized weather radars. The density function of the amplitude ratio is

$$(11) \quad f(u) = \frac{2u(1+u^2)(1-|\rho_{co}|^2)}{[(1+u^2)^2 - 4|\rho_{co}|^2u^2]^{3/2}}$$

where u is the normalized amplitude ratio defined as $(|v_{vv}|/\sqrt{P_{vv}})(|v_{hh}|/\sqrt{P_{hh}})^{-1}$ and $|\rho_{co}|$ is the magnitude of the correlation coefficient between v_{hh} and v_{vv} . [Figure 2.4](#) shows how the distribution

of u is very narrow for high values of $|\rho_{co}|$ which implies high values of $|\rho_{co}|$ are desired to achieve accurate estimates of differential reflectivity.

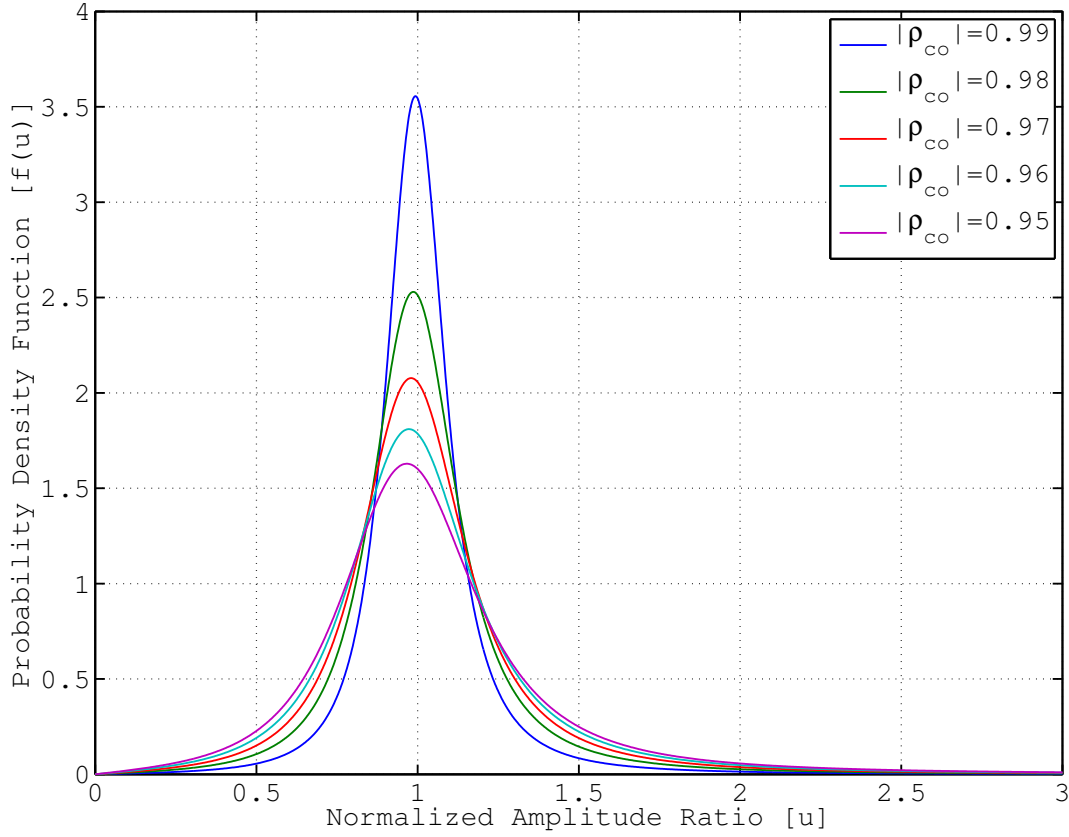


FIGURE 2.4. Probability density function for normalized amplitude ratio u for various values of $|\rho_{co}|$.

Similarly, the density function for the differential phase can be written in terms of the joint density function

$$(12) \quad f(\theta_v, \theta_h) = \frac{1 - |\rho_{co}|^2}{4\pi^2} (1 - \beta^2)^{-3/2} (\beta \sin^{-1} \beta + \frac{\pi\beta}{2} + \sqrt{1 - \beta^2}); -1 \leq \beta \leq +1$$

where $\beta = |\rho_{co}| \cos(\theta_v - \theta_h - \bar{\theta}_0)$ and $\bar{\theta}_0 = \arg(\rho_{co})$, shown in figure 2.5.

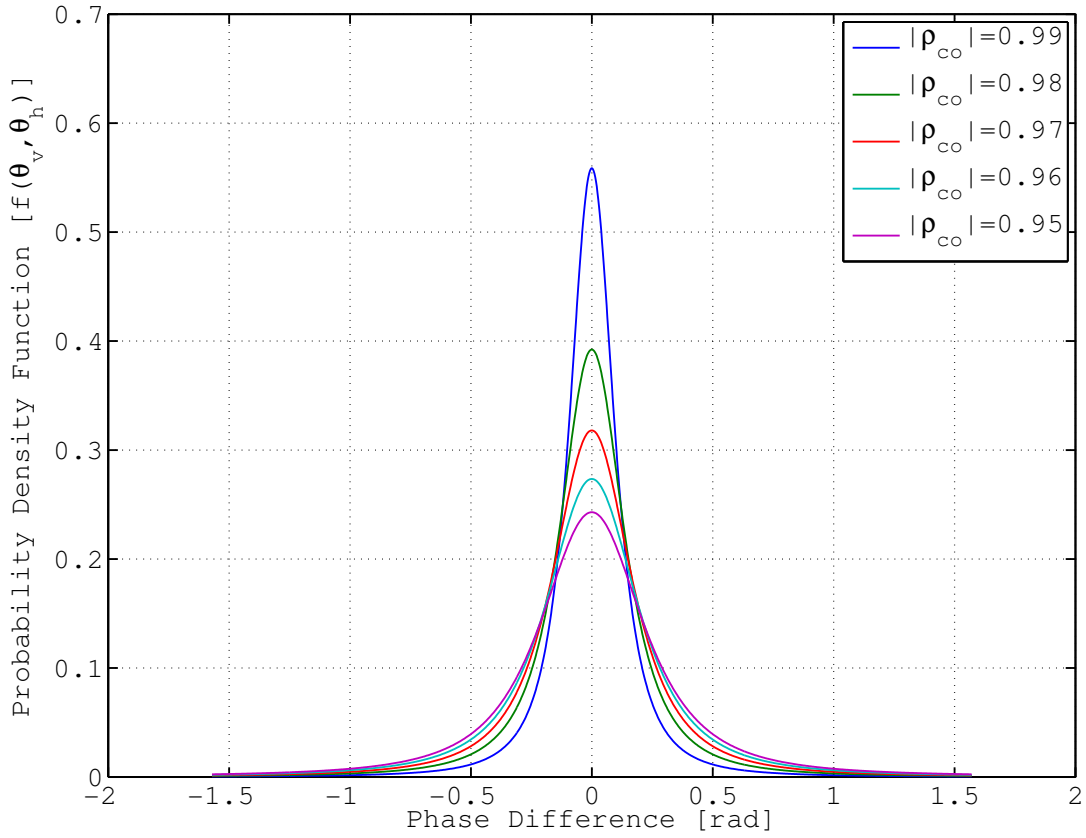


FIGURE 2.5. Joint probability density function of phases θ_v and θ_h in terms of phase difference $\theta_v - \theta_h - \bar{\theta}_0$ for various values of $|\rho_{co}|$.

2.4. POLARIMETRIC RADAR OBSERVABLES

The following section provides the definition of common polarimetric radar observables along with comments on their interpretation.

2.4.1. Equivalent Reflectivity Factor

In radar meteorology, it is conventional to express the radar equivalent reflectivity factor Z_e

$$(13) \quad Z_e = \frac{\lambda^4}{\pi^5 |K_w|^2} \eta_{hh}$$

in terms of the backscattering cross section η_{hh} or η_{vv} in the case of vertically polarized reflectivity

$$(14) \quad \eta_{hh} = 4\pi \langle n | S_{hh} |^2 \rangle$$

$$(15) \quad \eta_{vv} = 4\pi \langle n | S_{vv} |^2 \rangle$$

where n is the particle size concentration per unit volume in m^{-3} and K_w is the dielectric factor of water $(\epsilon_r - 1)(\epsilon_r + 2)^{-1}$.

$$(16) \quad Z_{e,h}[mm^6 m^{-3}] = \frac{1}{\pi^5 |K_w|^2} \left(\frac{2}{cT_0} \right) \left[\frac{(4\pi)^3}{P_t G_0^2} \right] \left[\frac{8 \ln(2)}{\pi \theta_B \phi_B} \right] \lambda^2 r_0^2 \bar{P}_r(r_0)$$

$$(17) \quad Z_h[dBZ] = \hat{P}_{co}^h[dBm] + C + 20 \log_{10}(r_0)[km]$$

$$(18) \quad C = 10 \log_{10} \left\{ \frac{10^{21}}{\pi^5 |K_w|^2} \left[\frac{2}{cT_0} \right] \left[\frac{(4\pi)^3}{P_t G_0^2} \right] \left[\frac{8 \ln(2)}{\pi \theta_B \phi_B} \right] \right\}$$

The radar constant, C , in equation 18, is scaled by 10^{21} to account for the use of km and dBm units in transmit/receive power and range respectively (all other parameters are consistent with SI units). Equation 17 shows the equivalent reflectivity Z_e in typical logarithmic units, dBZ , along with the remaining two terms (i.e. first and third) required in the computation. \hat{P}_{co}^h is the h-channel, co-polarized signal received referenced to the antenna port. It is estimated from the received signal's

autocorrelation at lag 0 (i.e. sample-time autocorrelation), shown in equation 19 and referenced to the antenna ports by the subtraction of the receiver gain, G_r , as shown in equation 20.

$$(19) \quad \hat{P}_{hh} = \frac{1}{N} \sum_{k=0}^{N-1} v_{hh}(k) v_{hh}^*(k)$$

$$(20) \quad \hat{P}_{co}^h = 10 \log_{10}(\hat{P}_{hh}) - G_r$$

2.4.2. Mean Doppler Velocity

As shown in figures 2.1 and 2.2, the received signal from a transmitted pulse is the sum of the scattered signals from an ensemble of particles within the resolution volume. For a single particle, the Doppler spectrum can be represented by a delta function located at $f = -2\vec{v} \cdot \hat{i} / \lambda$ where \vec{v} is the particle velocity vector, \hat{i} is a unit vector in the direction of incidence and λ is the wavelength. Although individual particles contribute line spectra, the presence of a large number of particles with different velocities or $\hat{i} \cdot \vec{v}$ and linearity of the spectral representation results in a continuum in the frequency domain.

Equations 21 and 22 show the typical mean velocity estimator, \hat{v} , based on the argument of the autocorrelation function, $\hat{R}[n]$, at lag 1, which is commonly known as the pulse pair estimate. This estimator arises from the assumption of symmetry in the power spectral density about some mean frequency, \bar{f} , which results in the phase of $\hat{R}[n]$ being related to \bar{f} . Please see [Bringi and Chandrasekar \(2001\)](#) and [Doviak and Zrnic \(2006\)](#) for more details on the subject.

$$(21) \quad \hat{R}[n] = \frac{1}{N} \sum_{k=0}^{N-2} v_{hh}(k+n)v_{hh}^*(k)$$

$$(22) \quad \hat{v} = -\frac{\lambda}{4\pi T_s} \text{arg}\{\hat{R}[1]\}$$

It should be clear that equation 22 applies to radar systems employing a uniform pulsing scheme (i.e. single PRT) which implies a limitation dependent on the selection of PRT and system wavelength on the maximum velocity that can be measured unambiguously. Techniques such as the use of staggered pulsing scheme aid in the improvement of unambiguous velocity measurements and will be discussed in chapter 4 in the context of the design of the Dual-frequency Dual-polarized Doppler Radar (D3R) system.

2.4.3. Doppler Spectrum Width

The estimate of the Doppler velocity spectrum width, $\hat{\sigma}_v$, of meteorological targets is affected by shear and turbulence within the measurement volume (antenna movement can affect it to a lesser extent as well). This makes it a useful parameter in the detection of both events. Equation 23 shows a typical estimator involving the magnitude of autocorrelation function at lags 0 and 1, which is based on the assumption of a Gaussian spectrum shape with mean velocity \hat{v} and width σ_v .

$$(23) \quad \hat{\sigma}_v = \frac{\lambda}{2\pi T_s \sqrt{2}} \left[\left| \frac{\hat{R}(0)}{\hat{R}(1)} \right| \right]^{\frac{1}{2}}$$

Equation 23 is valid in the absence of noise or high signal to noise ratio (SNR) (≥ 20 dB). In the presence of noise, $\hat{R}[0]$ should be replaced by $\hat{R}_{S+N}[0] - \hat{R}_N[0]$ which implies that system noise estimation is in place which may not always be true. Please see [Srivastava et al. \(1979\)](#) for a discussion on the subject.

2.4.4. Normalized Coherent Power

Since all measurements made by polarimetric Doppler weather radars are in some way or another affected by the presence of noise, it is practical to have some sort of quality index under which data can be thresholded upon. The normalized coherent power (NCP) defined in equation 24 serves this purpose. NCP will range from 0 for uncorrelated signal such as white noise to 1 for a pure tone (noise free delta function). Typical thresholding values lie within 0.4 to 0.5.

$$(24) \quad NCP = \frac{|\hat{R}(1)|}{\hat{R}(0)}$$

2.4.5. Differential Reflectivity

The differential reflectivity, Z_{dr} , is a measure of mean particle shape. It is defined as

$$(25) \quad Z_{dr}[dB] = 10 \log_{10} \left[\frac{\langle |S_{hh}|^2 \rangle}{\langle |S_{vv}|^2 \rangle} \right] = 10 \log_{10} \left[\frac{\hat{P}_{hh}}{\hat{P}_{vv}} \right]$$

where \hat{P}_{hh} and \hat{P}_{vv} are the h and v co-polarized received signal powers respectively.

As drop size increases, they tend to be oblate in shape and therefore generate Z_{dr} values greater than 0.

2.4.6. Linear Depolarization Ratio

The linear depolarization ratio (LDR) is defined as

$$(26) \quad LDR_{hv}[dB] = 10\log_{10} \left[\frac{\langle |S_{hv}|^2 \rangle}{\langle |S_{vv}|^2 \rangle} \right] = 10\log_{10} \left[\frac{\hat{P}_{hv}}{\hat{P}_{vv}} \right]$$

where the \hat{P}_{hv} is the cross-polarized power received after transmitting a v-polarized signal and \hat{P}_{vv} is the co-polarized power received after transmitting a v-polarized signal. LDR signatures are typically generated by particles composed of liquid-ice mixtures which make it useful in the classification of hydrometeor types.

2.4.7. Complex Co-polar Correlation Coefficient

The complex correlation coefficient \hat{R}_{hhvv} at lag 0 is defined as

$$(27) \quad \hat{R}_{vvhv} = \frac{1}{N} \sum_{k=0}^{N-1} v_{vv}(k)v_{hh}^*(k)$$

where v_{vv} and v_{hh} are both co-polarized, complex received voltages. From this correlation, two very useful parameters of polarimetric radars are defined. It's normalized magnitude, which is essentially the Pearson product-moment correlation coefficient of v_{hh} and v_{vv} and defined as

$$(28) \quad |\rho_{hv}(0)| = \frac{|\hat{R}_{hhvv}|}{\sqrt{\hat{P}_{hh}}\sqrt{\hat{P}_{vv}}}$$

and it's argument defined as

$$(29) \quad \arg[\hat{R}_{vvhh}] = \psi_{dp} = \phi_{dp} + \delta$$

where ϕ_{dp} is the differential propagation phase and δ the differential shift upon scattering which is ≈ 0 in the Rayleigh scattering regime.

2.5. PASSIVE MICROWAVE REMOTE SENSING

In general, passive remote sensing is based on the principle that all matter radiates electromagnetic energy (Ulaby et al. (1981)). The field of microwave radiometry is dedicated to the science and engineering of systems with the capability of measuring such energy. In particular, this work focuses on microwave measurements of the atmosphere and its constituents. This section focuses on providing the basis behind what generates such measurements.

2.5.1. Black-body Radiation

According to Planck's radiation law (equation 30), a black-body is defined as a perfectly opaque material that absorbs all incident radiation (none is reflected) at all frequencies. Moreover, when in thermodynamic equilibrium, it is also a perfect emitter since the energy absorbed would otherwise increase its temperature. The spectral brightness (specific intensity in some texts), B_f , in units of $Wm^{-2}sr^{-1}Hz^{-1}$, is given by equation 30 and shown in figure 2.6

$$(30) \quad B_f = \frac{2hf^3}{c^2} \left(\frac{1}{e^{\frac{hf}{kT}} - 1} \right)$$

where h is Planck's constant ($6.63 \times 10^{-34} \text{ Joules}$), f is frequency in Hz , k is Boltzmann's constant ($1.38 \times 10^{-23} \text{ JoulesK}^{-1}$), T is the absolute temperature in K and c is the speed of light in m/s .

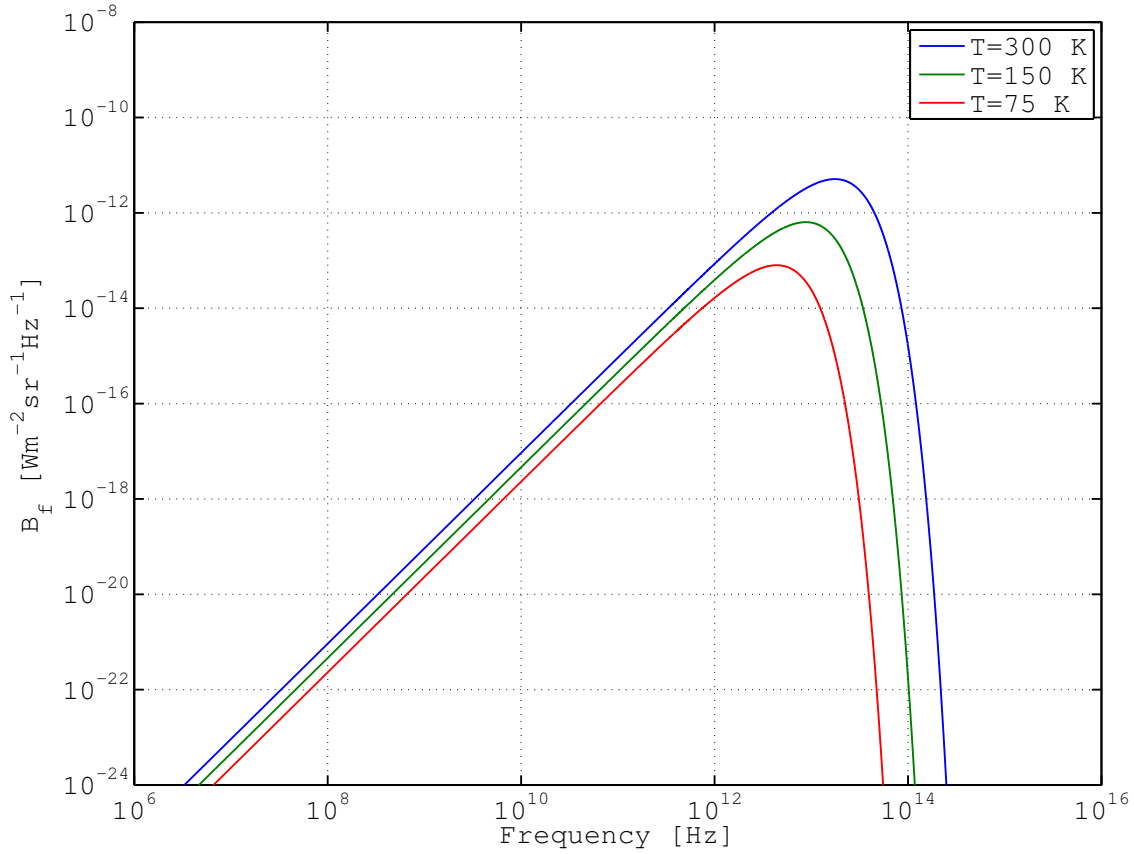


FIGURE 2.6. Spectral brightness B_f from Planck's black-body radiation law for $T = 300, 150$ and 75 K .

Two well known approximations to Planck's radiation law exist. Namely, the Rayleigh-Jeans and Wien laws, equations 33 and 32, which apply to the lower ($\frac{hf}{kT} \ll 1$) and upper ($\frac{hf}{kT} \gg 1$) ends of the spectrum B_f respectively.

$$(31) \quad B_f \approx \frac{2f^2 kT}{c^2}$$

$$(32) \quad B_f = \frac{2h}{c^2} f^3 e^{-\frac{hf}{kT}}$$

2.5.2. Grey-body Radiation

In the previous section, the ideal black-body radiation law was presented. In reality, materials do not necessarily absorb and emit all energy incident upon them and therefore are termed grey-bodies. Using equation 33 (microwave region of spectrum), the brightness of a black-body, B_{bb} , at physical temperature T over a narrow bandwidth Δf can be written as

$$(33) \quad B_{bb} = \frac{2f^2kT}{c^2} \Delta f$$

As an example, to illustrate the concept of emissivity and brightness temperature, one can consider an isothermal medium with brightness having angular dependence, $B(\theta, \phi)$, as

$$(34) \quad B(\theta, \phi) = \frac{2f^2k}{c^2} T_B(\theta, \phi) \Delta f$$

which we can now use to define the emissivity, $e(\theta, \phi)$, of the material as

$$(35) \quad e(\theta, \phi) = \frac{B(\theta, \phi)}{B_{bb}} = \frac{T_B(\theta, \phi)}{T}$$

From equation 35, we can infer that since $B(\theta, \phi) \leq B_{bb}$ it follows that $0 \leq e(\theta, \phi) \leq 1$ and therefore the brightness temperature of a material, T_B , will always be smaller than or equal to its physical temperature T .

2.5.3. Power and Temperature Correspondence

Although passive remote observations are essentially measurements of power, these are seldom expressed using units of power, but of temperature. In Nyquist (1928), it was shown that the voltage across a resistor of value R at temperature T with an ideal filter (i.e. unity gain and rectangular passband) of bandwidth B is $V_{RMS}^2 = 4RkTB$. To obtain the power delivered by the resistor to a load connected to it, the resistor can be modeled as a voltage source with V_{RMS} and source impedance $Z_S = R + jX_S$ (in series with source). For maximum power transfer, $Z_L = Z_S^* = R - jX_S$ which cancels out the reactive impedance of the source which is included for completeness (i.e. models capacitance and inductance across resistor terminals). Therefore the average noise power delivered to the load is $P_n = I_{RMS}^2 R = (V_{RMS}(2R)^{-1})^2 R = V_{RMS}^2 (4R)^{-1} = kTB$.

Alternatively, Ulaby et al. (2014a) derives the same expression as follows. Consider a lossless antenna with effective aperture A_R and radiation pattern $f(\theta, \phi)$ (coordinate system defined in figure 2.7). If a uniformly distributed blackbody with spectral brightness intensity I_f with units of $Watts\ sr^{-1}\ m^{-2}\ Hz^{-1}$ surrounds the antenna, the differential spectral power received can be written as $dP_f = I_f A_R f(\theta, \phi) d\Omega$. When integrated to compute P and dividing by a factor of two to account for a single linearly polarized measurement of unpolarized radiation, it looks as follows.

$$(36) \quad P = \frac{1}{2} A_R \int_{f_1}^{f_2} \iint_{4\pi} I_f f(\theta, \phi) d\Omega df$$

If operation within the microwave region is assumed, the Rayleigh-Jeans approximation, equation 72 introduced in section 2.5.1, can be used as I_f and if the measurement bandwidth $B = f_2 - f_1$ is small enough to treat I_f as constant (i.e $B \ll f$), equation 36 can be written as

$$(37) \quad P_{BB} = kTB \frac{A_R}{\lambda^2} \iint_{4\pi} f(\theta, \phi) d\Omega$$

where the subscript indicates the equivalent of a blackbody enclosure surrounding the antenna, the double integral represents the antenna pattern solid angle Ω_p . Finally, recall the antenna solid angle is related to the antenna effective aperture A_R by $\Omega_p = \lambda^2 A_R^{-1}$ which when substituted into equation 37 yields the classical equation of $P_{bb} = kTB$. Hence the correspondence or interchangeable use of power and temperature.

2.5.4. Emissions from Atmospheric Constituents

In classical radiative transfer theory developed by Chandrasekhar (1960), a radiating electromagnetic field is governed by the emission, absorption and scattering properties of the medium it travels through. On Earth's atmosphere, these properties are primarily defined by atmospheric constituents such as gases, mainly oxygen and water vapor, as well as water in its liquid and solid states. Figure 2.8 shows the absorption coefficient, in $dB km^{-1}$, for typical mid-latitude atmospheric conditions (hydrometeor free) due to oxygen and water vapor using expressions from Ulaby et al. (1981). It is evident that strong absorption and therefore emissions would be expected under thermodynamic equilibrium from water vapor at 22.235 GHz and 183.31 GHz and likewise, from oxygen, at 60 GHz and 118.75 GHz.

For large liquid and frozen hydrometeors, where scattering effects cannot be ignored, the differential radiative transfer equation (DRTE) for a planar-stratified atmosphere, equation 38, is solved for the brightness temperature $T_B(z, \theta, f)$

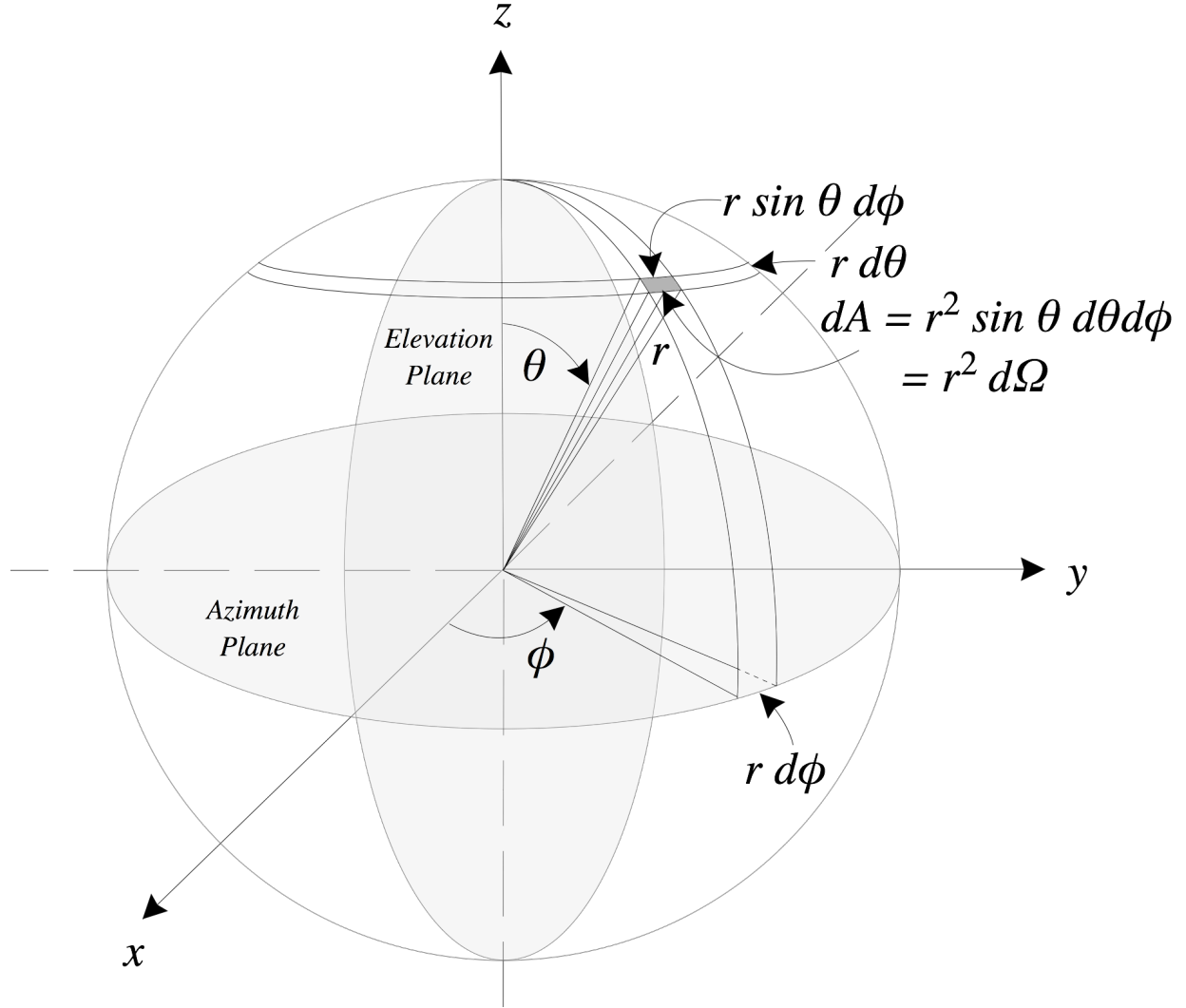


FIGURE 2.7. Spherical coordinate system showing definition of differential solid angle $d\Omega$. Azimuth ($\theta = 90 \text{ deg}$) and elevation ($\phi = 45 \text{ deg}$) planes shaded in light grey.

$$\begin{aligned}
 \cos \theta \frac{dT_B(z, \theta, f)}{dz} &= -K_e(z, f)T_B(z, \theta, f) + K_a(z, f)T(z) \\
 &+ K_s(z, f) \int_0^\pi \bar{P}(z, \theta, \theta', f)T_B(z, \pi - \theta', f) \sin \theta' d\theta'
 \end{aligned}
 \tag{38}$$

where θ and θ' are angles measured from zenith direction, f is frequency, $T(z)$ is the atmospheric temperature at height z , K_e , K_a and K_s represent the bulk layer, dz , extinction, absorption and

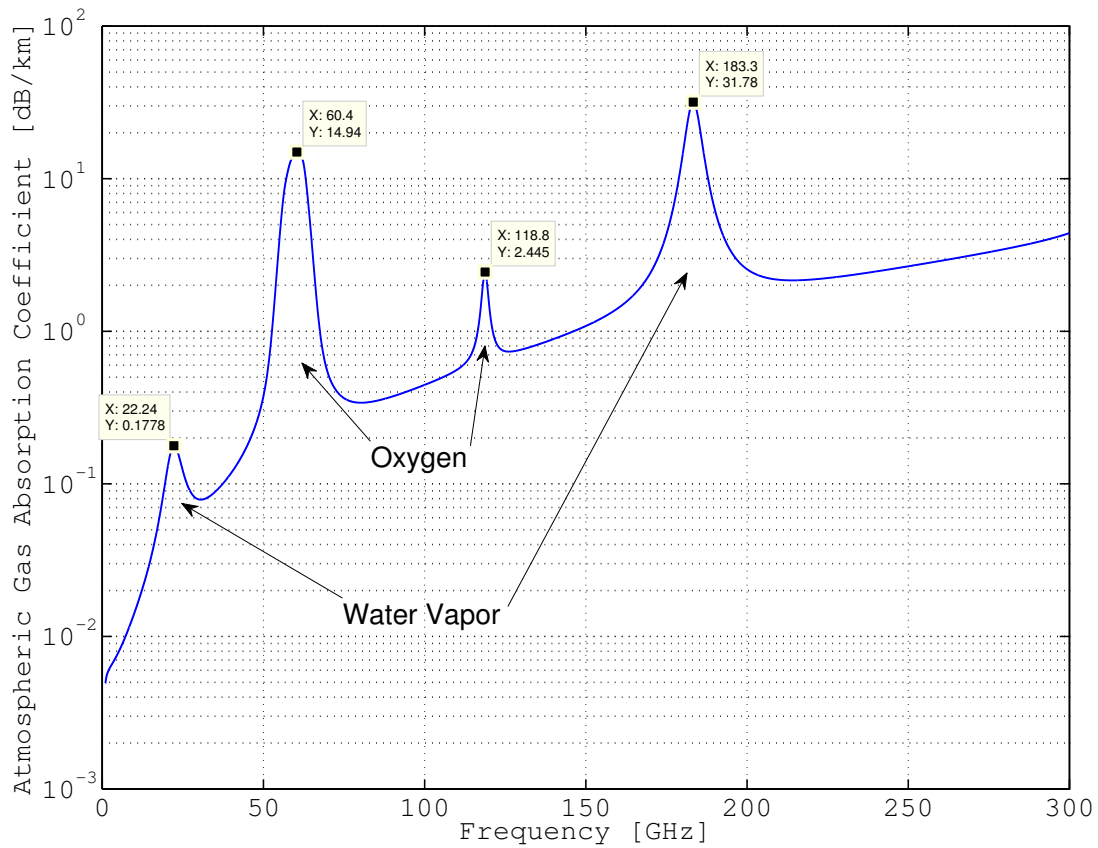


FIGURE 2.8. Atmospheric gas, oxygen plus water vapor, absorption coefficient for water vapor content of 7.5 gm^{-3} , surface level temperature and pressure of 290 K and 1013 mbar respectively.

scattering coefficients, respectively, while \bar{P} is the phase matrix which models the fraction of radiation scattered from angle θ' to θ at height z , Hou et al. (2008). Figure 2.9 highlights the variations in T_B over frequency for a set of five atmospheric conditions. From this figure, the level of sensitivity of each frequency to specific factors defining the atmospheric state is evident and hence is the driving factor for frequency choices in passive remote sensing of the atmosphere. The derivation and solution to equation 38 is beyond the scope of this work. Please see Gasiewski (1993) for a detailed description.

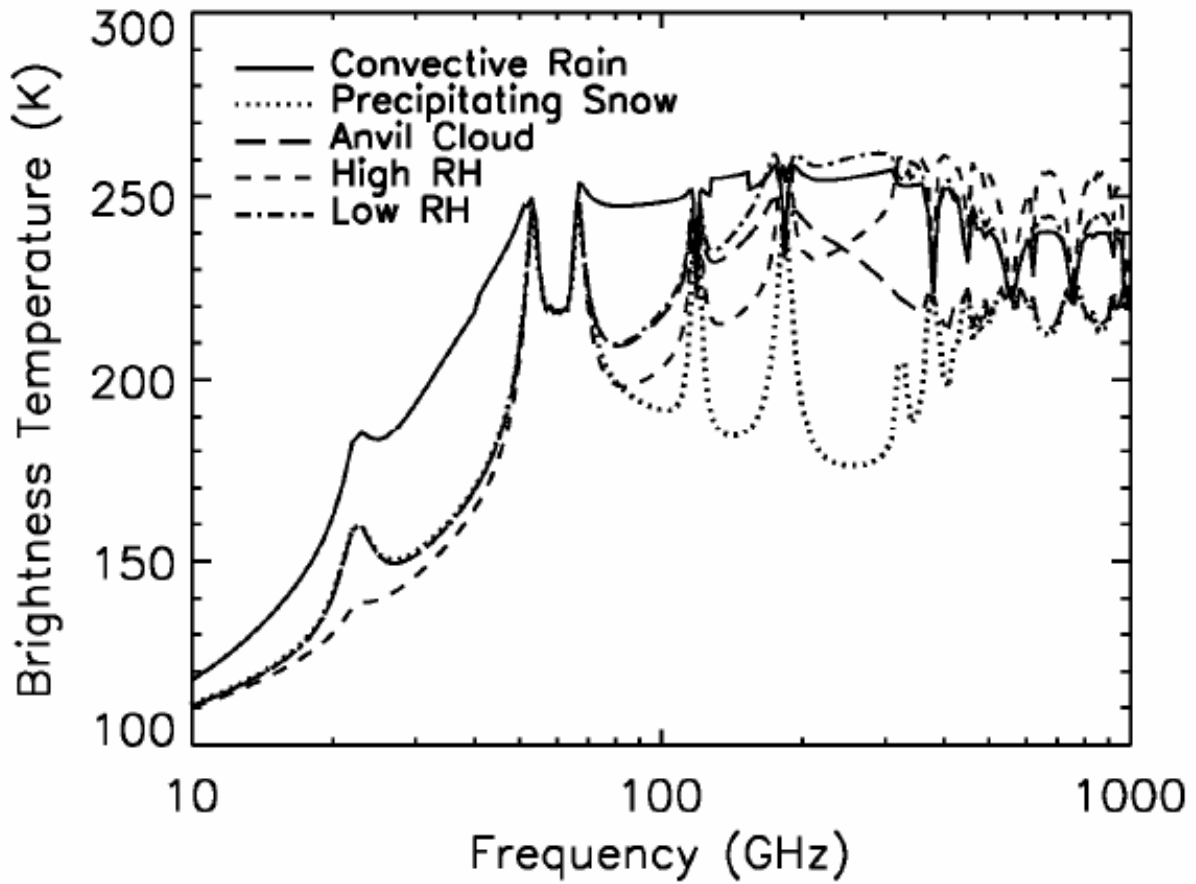


FIGURE 2.9. Simulated brightness temperatures from 10 to 1000 GHz for five atmospheric and cloud conditions (from Hou et al. (2008)).

CHAPTER 3

RADAR-RADIOMETER SYSTEM: ENGINEERING ASPECTS IN THE DESIGN OF A COMBINED PLATFORM

In this chapter focuses on important aspects in the development of a combined radar-radiometer instrument while at the same time characterizing the D3R's performance as a radiometer system. First, key performance parameters in the design of a radiometer antenna such as beam and radiation efficiencies are discussed. Second, a brief introduction to radiometer receiver architectures, corresponding sensitivity and stability measurement is presented. Last, initial observations using the D3R passive channels are presented as a proxy for the following chapters.

3.1. ANTENNAS

Regardless of type of instrument, radar or radiometer, both require antennas as an electromagnetic energy coupling mechanism between the observation scene and the instrument. Antennas are primarily characterized by properties of their spatial gain pattern distribution, which in turn sets the spatial resolution achievable by the instrument. Equations 39 and 40 show basic radar and radiometer measurement definitions, namely received power (\hat{P}_r) and lossless antenna temperature (T'_A), dependence on the normalized antenna gain pattern $f(\theta, \phi)$ defined as $G(\theta, \phi) * G_0^{-1}$ where G represents the power gain pattern and G_0 is the maximum of G .

$$(39) \quad \bar{P}_r(r_0) = \left[\frac{cT_0}{2} \right] \left[\frac{\lambda^2 P_t G_0^2}{(4\pi)^3 r_0^2} \right] \left[\iint_{4\pi} f^2(\theta, \phi) \eta(r_0, \theta, \phi) d\Omega \right]$$

$$(40) \quad T'_A = \frac{\iint T_B(\theta, \phi) f(\theta, \phi) d\Omega}{\iint_{4\pi} f(\theta, \phi) d\Omega}$$

Observations from radar and radiometers are defined by their corresponding scene function defined by $\eta(r_0, \theta, \phi)$ (backscatter coefficient per unit volume) and $T_B(\theta, \phi)$ (scene brightness temperature) weighted by the corresponding antenna pattern function, respectively. In the case of radar, the two-way propagation nature of the measurement (i.e. pulse is transmitted and backscattered towards the instrument) sets the $f^2(\theta, \phi)$ dependence of \hat{P}_r whereas in the radiometer T'_A depends on $f(\theta, \phi)$ since it is a one-way measurement. This is an interesting fact for the radar-radiometer designer to consider while designing a shared aperture system since the observation volumes for each measurement are not perfectly matched.

The measured brightness temperature attributed to the footprint or volume, typically defined by the half power points of the antenna pattern, is affected by stray radiation captured by side lobes and self emissions caused by ohmic losses within the antenna structure itself. Equation 41 defines the main lobe temperature T_{ML} with respect to the total antenna temperature T_A , side lobe temperature T_{SL} , physical temperature T_0 , radiation efficiency ξ and beam efficiency η_b .

$$(41) \quad T_{ML} = \left(\frac{1}{\xi\eta_b} \right) T_A - \left(\frac{1 - \eta_b}{\eta_b} \right) T_{SL} - \left(\frac{1 - \xi}{\xi\eta_b} \right) T_0$$

Although the estimation of T_{ML} seems straight forward, it carries some difficulties with it. Assuming that the radiation and beam efficiencies, ξ and η_b respectively, are known parameters, the contribution by the scene viewed by side lobes T_{SL} is an unknown and can vary as the instrument scans and/or travels introducing a time-varying bias on T_{ML} (see figure 3.1). Figure 3.2 illustrates this effect as a function of T_{SL} for several values of η_b . Since the typical accuracy required for

most applications is of the order of 1 K, it is very important to try to choose an antenna with η_b as close to 1 as possible. This is done in practice by minimizing the side lobes levels as much as possible, which in the case of reflector antennas, results in the use more aggressive tapering functions ending in reduced aperture efficiencies. Farrar and Jones (2012) illustrate the effects of possible antenna beam efficiency issues on the Microwave Radiometer (MWR) instrument aboard the Aquarius/SAC-D satellite mission.

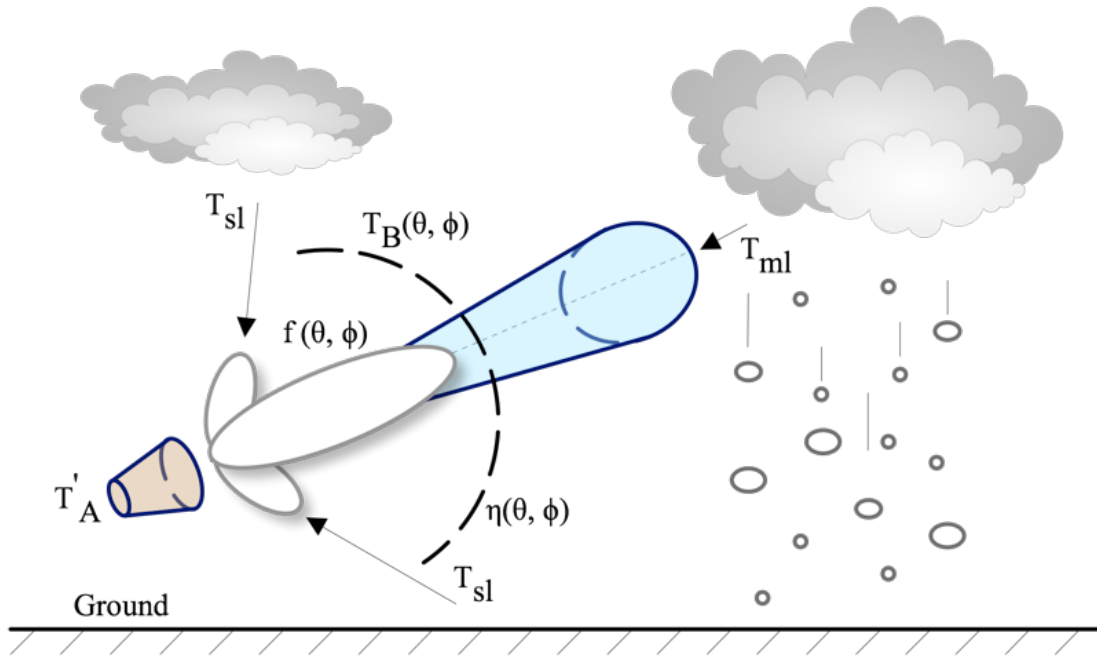


FIGURE 3.1. Depiction of antenna side lobe contributions to main lobe brightness temperature.

The antenna beam efficiency is defined in equation 42 as the ratio of the main lobe to side lobe solid angles. In practice, the accurate determination of such quantity involves the measurement of the antenna pattern over 4π steradians with high resolution and dynamic range to effectively measure all power radiated by the antenna. This can be a very time consuming task compared to the typical set of principal plane pattern measurements performed. In some cases, depending on the antenna dimensions it is simply impractical.

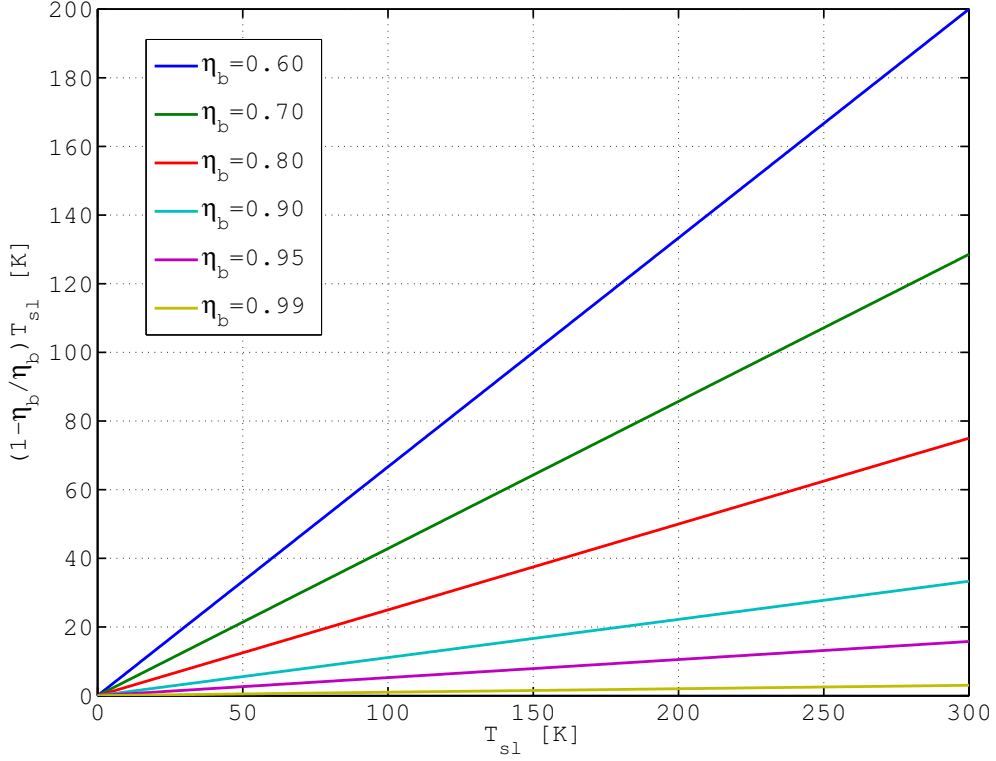


FIGURE 3.2. Antenna side lobe contribution to main lobe brightness temperature based on beam efficiency η_b and side lobe scene brightness temperature.

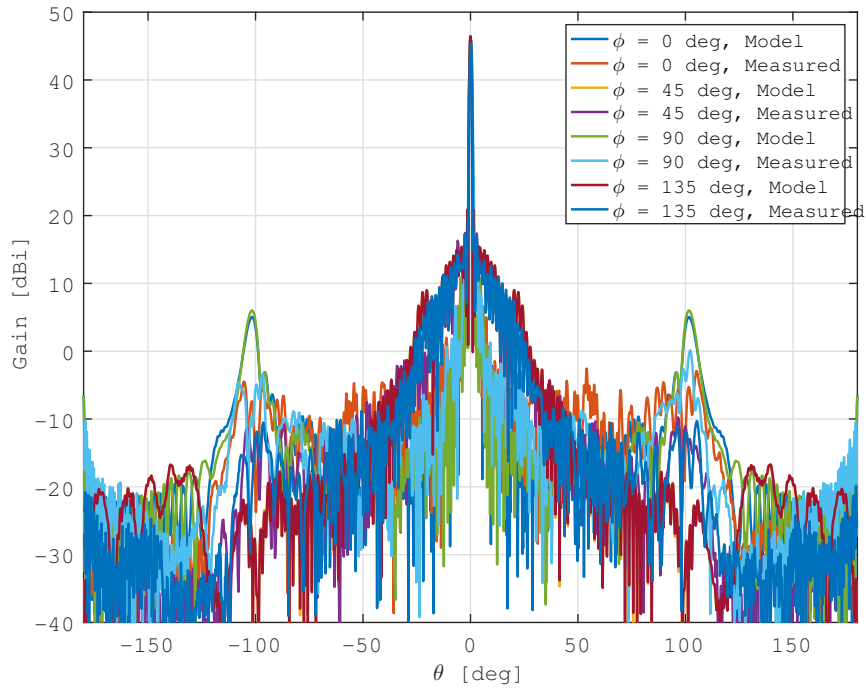
$$(42) \quad \eta_b = \frac{\iint_{main\ lobe} f(\theta, \phi) d\Omega}{\iint_{4\pi} f(\theta, \phi) d\Omega}$$

In the case of the D3R system, the antennas were modeled and simulated at a high resolution to estimate their beam-efficiencies [Marrero \(2015b\)](#). The antenna feed CAD models were used to estimate the feed patterns using the finite element method (FEM) employed in the software package High Frequency Electromagnetic Simulation Software (HFSS) by Ansoft. Note that only external features of the feeds were available, therefore cross-polarization effects due to the orthogonal mode transducer (OMT) or polarizer are not accounted for. The simulated feed patterns were then imported into GRASP (software developed by TICRA) for simulation including the struts and

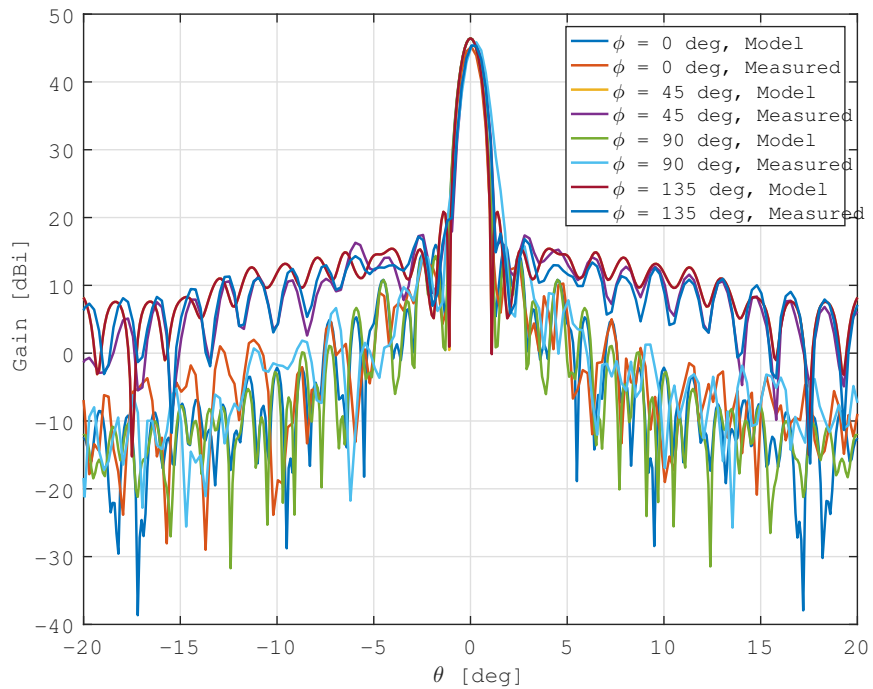
parabolic reflector surface. Patterns from the model were compared to the measured values from the actual antennas. Feed location and several model parameters were optimized until a reasonable match between patterns was reached (i.e. boresight gain within 1 dB, peak side-lobe level within 1 dB, similar side-lobe level rolloff and feed spill over radiation around the same location). Figures 3.3 and 3.4 illustrate the Ku and Ka-band modeled and measured co-polarized patterns respectively.

Once the model was finalized, simulated patterns with high resolution (e.g. $\Delta\theta = 0.1deg$ and $\Delta\phi = 1deg$) were not difficult to realize. These can then be used to carry out the integrations required to estimate η_b using equation 42. Throughout this process, the question of how much angular resolution is required to achieve a reasonable estimate of η_b arose several times. After a few iterations, it was noticed that estimates would increase and decrease without any plausible explanation other than numerical integration error. To gain some insight into the effect of the angular grid resolution in estimates of the pattern solid angle Ω_p , the main beam from a simulated model of the Ku-band antenna with $\Delta\theta = 0.01$ deg and $\Delta\phi = 1$ deg used. The main beam model was fitted using a cubic interpolant, evaluated at different grid resolutions followed by integration over the main beam to compute $\Omega_m(4\pi)^{-1}$. Figure 3.6 shows the results from this exercise. Note how for various grid resolution pairs, the ratio is over and underestimated. However, it seems to converge to a value between 78 to 80 % for grid resolutions better than 0.1 deg and 1 deg for $\Delta\theta$ and $\Delta\phi$ respectively. The final estimates were obtained from a model meeting this requirement. The results were 78.6 % and 85.1 % for the Ku and Ka-band antennas respectively.

Another alternative in the determination of η_b is defined in equation 43. This only requires detailed measurements over the main lobe, the antenna peak gain G_0 which can be obtained during

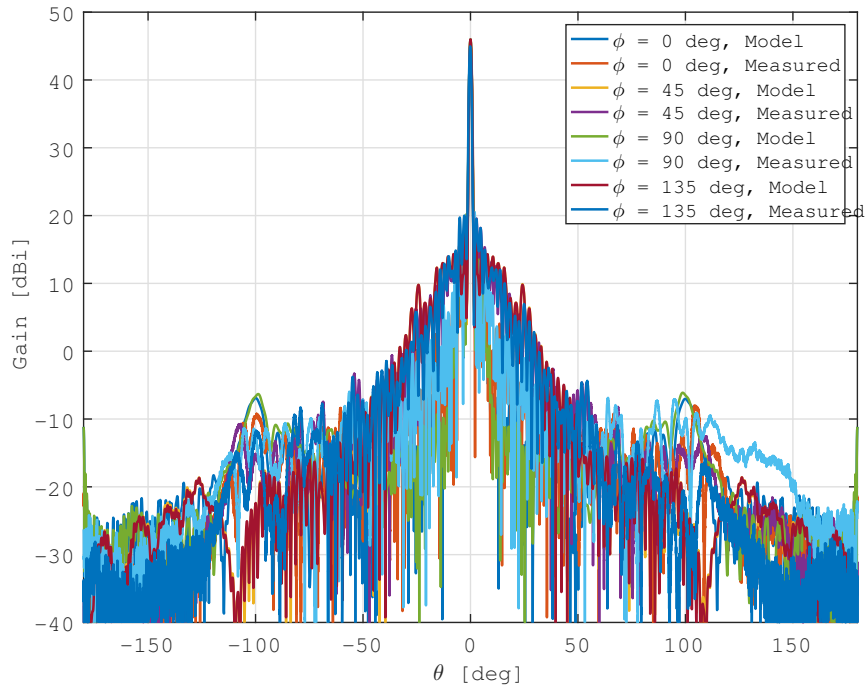


(A)

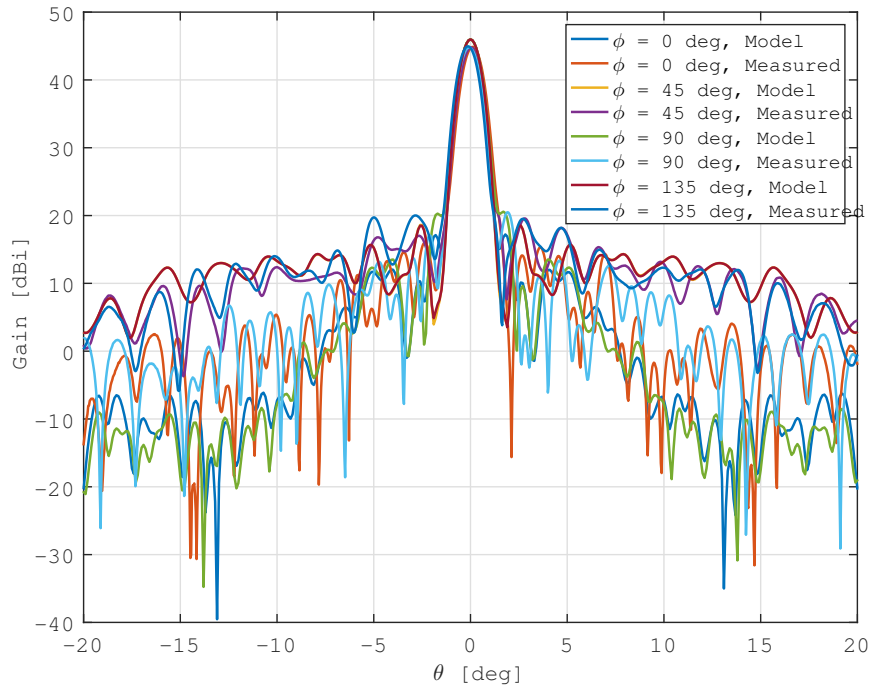


(B)

FIGURE 3.3. Ku-band wide angle (A) and narrow (B) measured and modeled co-polarized H-port principal plane patterns.

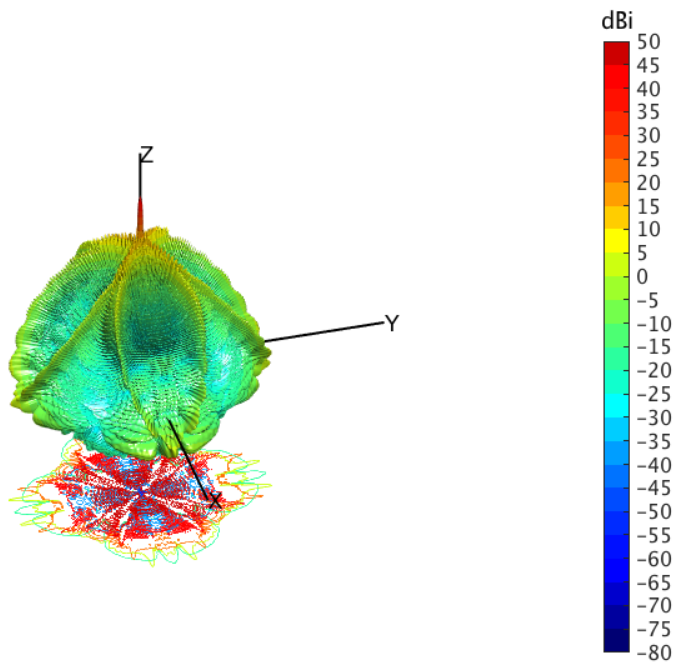


(A)

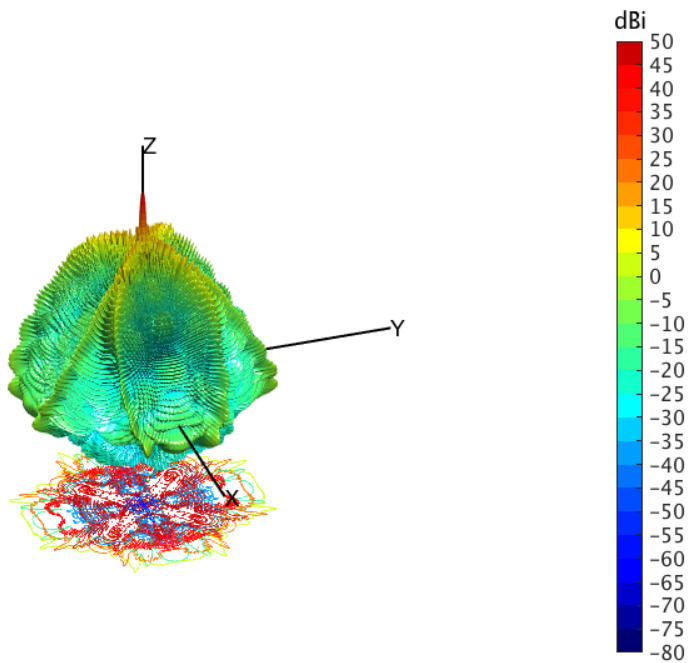


(B)

FIGURE 3.4. Ka-band wide angle (A) and narrow (B) measured and modeled co-polarized H-port principal plane patterns.



(A)



(B)

FIGURE 3.5. Ku-band (A), Ka-band (B) antenna high resolution models from combination of simulations using HFSS and GRASP.

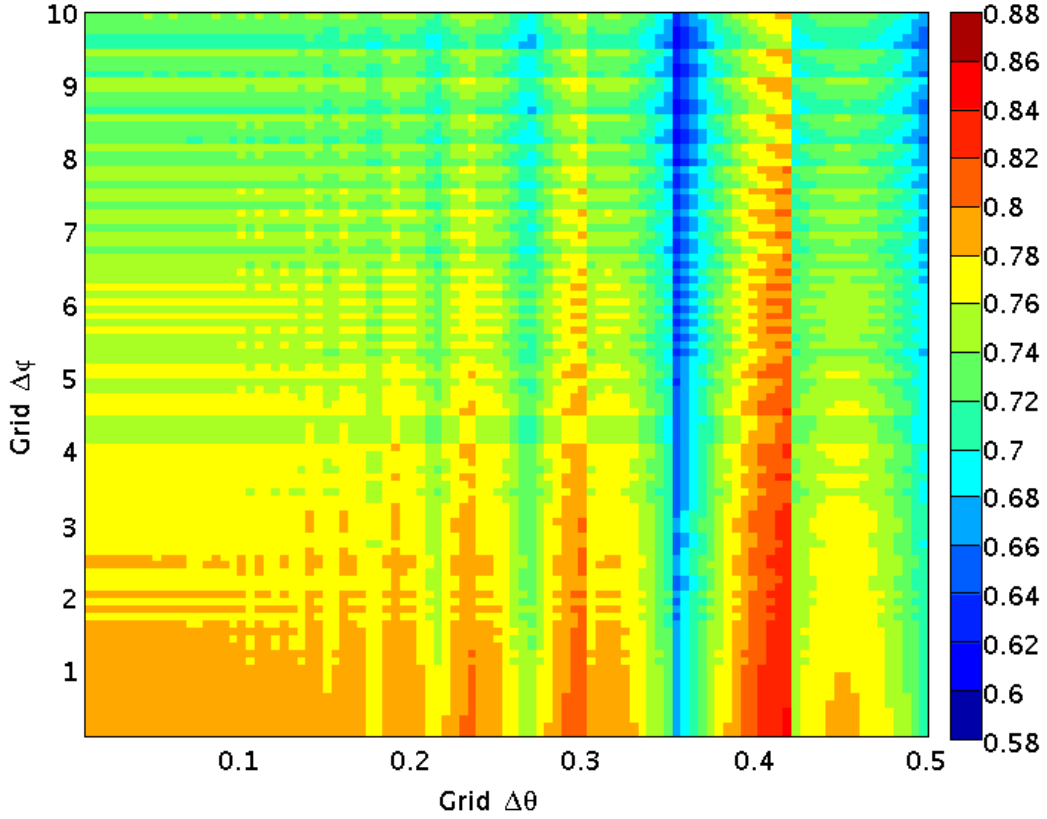


FIGURE 3.6. Ku-band antenna model resolution effect on beam efficiency computation. Colorbar represents the ratio $\Omega_m(4\pi)^{-1}$

the main lobe measurements and the antenna radiation efficiency ξ defined in equation 44. Although Ω_p appears on the denominator, alternate methods using cryogenic loads and the bucket technique have been used to determine ξ .

$$(43) \quad \eta_b = \frac{\xi}{4\pi G_0} \iint_{main\ lobe} f(\theta, \phi) d\Omega$$

$$(44) \quad \xi = \frac{G_0}{D_0} = \frac{4\pi G_0}{\iint_{4\pi} f(\theta, \phi) d\Omega}$$

Aside from contributions from T_{SL} , antenna ohmic losses will also impact T_{ML} . Figure 3.7 shows this effect over ξ for five values of η_b for a physical temperature of $T_0 = 298.65$ K. Unlike side lobe contributions, this effect can be estimated with knowledge of ξ , which is required as stated previously, and measurements of the antenna physical temperature T_0 .

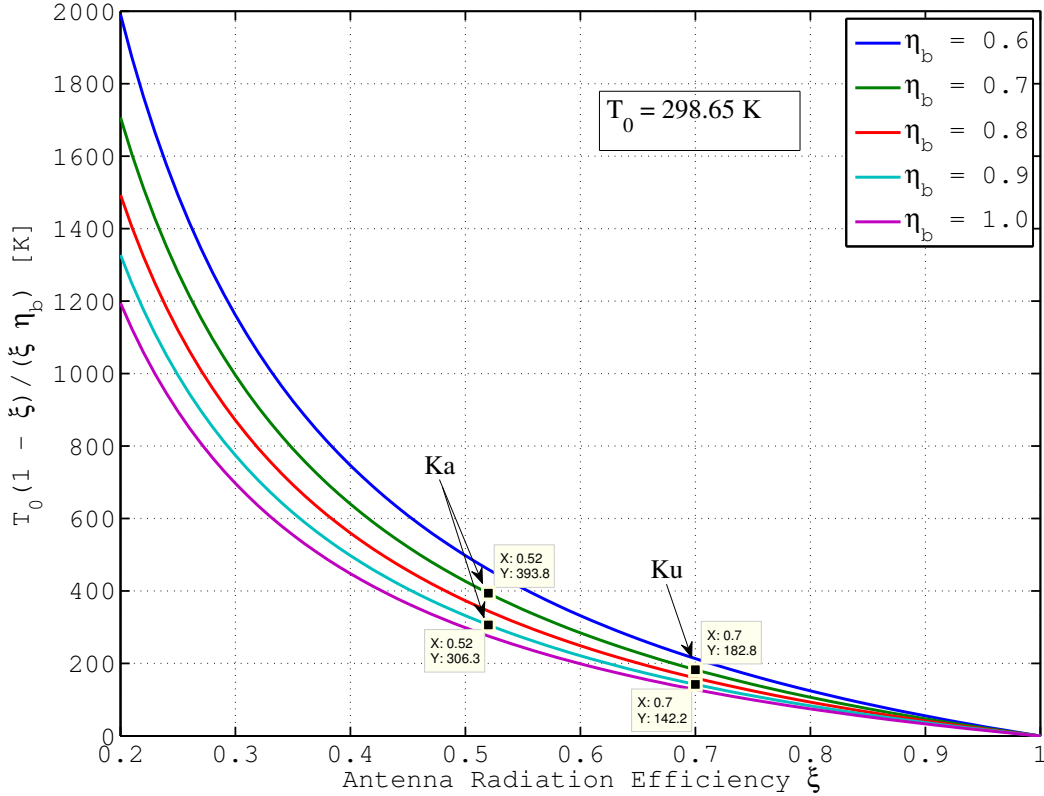


FIGURE 3.7. Antenna self emission contribution to main lobe temperature with estimated D3R Ku and Ka radiation efficiency ξ and beam efficiency η_b bounds.

3.2. BASIC RECEIVER ARCHITECTURE

Up to this point, aspects related to the measured antenna temperature T_A have been discussed. The focus is now shifted into aspects of receiving the power delivered by the antenna. In general, a superheterodyne receiver, shown in figure 3.8, is capable of providing power estimates of the signal delivered by the antenna. In summary, the signal from the antenna port is initially amplified by a

low noise amplifier stage with gain G_{RF} to reduce the effects of subsequent conditioning stages to the overall receiver noise figure F . In the case of the single-sideband receiver, filtering is performed in this stage as well to eliminate image frequencies that may have potential for interference. The signal is then mixed with the local oscillator (LO) signal to produce an intermediate frequency (IF) signal $f_{IF} = |f_{RF} - f_{LO}|$. Since a higher frequency $f = f_{RF} + f_{LO}$ will be produced as well, a bandpass filtering stage follows the mixing stage which also sets the pre-detection bandwidth B_{pre} of the receiver. The signal is then amplified once again by G_{IF} to set the level prior to being passed through a square-law detector followed by a low-pass filter. The square-law detector's output provides a voltage signal directly proportional to the input power and the final stage, low-pass filter, serves as an integrator with effective integration time $\tau = (2B_{LPF})^{-1}$, [Tiuri \(1964\)](#). This receiver configuration is capable of performing the function of a total-power radiometer.

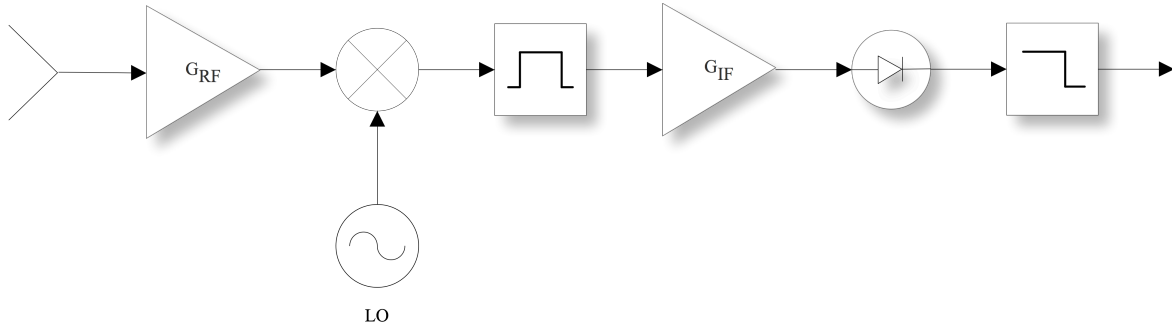


FIGURE 3.8. Superheterodyne receiver configuration for total-power radiometer measurements.

The total power radiometer receiver, is the the most sensitive (defined in equation 45) configuration and is the standard by which other configurations are measured, [Ulaby et al. \(2014a\)](#). However, it suffers from gain variations which are indistinguishable from variations on the antenna temperature T_A . Equation 46 shows the sensitivity ΔT including gain variations ΔGG^{-1} . In both equations B_{pre} is the pre-detection bandwidth, which is defined in equation 47 considering a real filter transfer function $H(f)$, and τ is the integration time.

$$(45) \quad \Delta T_{IDEAL} = \frac{T_{SYS}}{\sqrt{B_{pre}\tau}} = \frac{T_a + T'_{Rec}}{\sqrt{B_{Pre}\tau}}$$

$$(46) \quad \Delta T = T_{SYS} \sqrt{\frac{1}{B_{pre}\tau} + \left(\frac{\Delta G}{G}\right)^2}$$

$$(47) \quad B_{pre} = \frac{\left[\int_0^{\infty} H(f) df \right]^2}{\int_0^{\infty} H(f)^2 df}$$

The treatment or compensation for gain variations has given rise to various receiver configurations through the literature, including the Dicke radiometer, which introduce references through which receiver gain variations and the receiver temperature T_{rec} itself can be removed as part of the measurements process. Furthermore, in practice, the position of a reference switch, will only account for variations in components after the location of the switch and not before. In other words, antenna waveguides and the antenna itself would not be accounted for. This leads to the development of external sources or loads built-in to the instrument antenna for periodical end-to-end calibration. However, this is not always practical from an instrument size and/or complexity perspective. Please see [Ulaby et al. \(2014a\)](#) and [Camps and Tarongí \(2010\)](#) for a review on radiometer receiver architectures and respective sensitivities.

3.2.1. Receiver stability

Equation 46 states that a total power radiometer's sensitivity or ΔT is governed by the system temperature T_{SYS} , pre-detection bandwidth B_{pre} , integration time τ and receiver gain fluctuations ΔGG^{-1} . For such a system, T_{SYS} will vary with the scene under observation and system's physical temperature, B_{pre} is fixed based on the receiver design and spectrum allocation available, ΔGG^{-1} is defined by component stability, which may also depend on physical temperatures, finally leaving τ as a tuning parameter to achieve a prescribed ΔT . In the case of the D3R system, the passive channel bandwidth B is limited to 1 MHz and therefore large integration times are expected. However, one may not integrate as long one desires and continue to reduce variance or radiometric sensitivity continuously. A limit to this variance reduction exists and it varies from system to system. Typically, a system's ΔT versus integration time can be characterized using time series of experimental data and the Allan variance (Iturbide-Sanchez et al. (2007); Land et al. (2010)).

The Allan variance was first introduced by Allan (1966) in the characterization of atomic clock frequency stability, further expanded by Barnes et al. (1971) for different types of noise spectral densities and applied to radio-astronomy systems by Schieder et al. (1985). Using Schieder et al. (1985) as reference, the difference of two successive time averaged system voltages $R_n(t)$ can be written as

$$(48) \quad d(T) = R_1(T) - R_2(T)$$

where

$$(49) \quad R_1(T) = \frac{1}{T} \int_t^{t+T} s(t) dt, \quad R_2(T) = \frac{1}{T} \int_{t+T}^{t+2T} s(t) dt$$

and $s(t)$ is the system output signal at time t and T is the integration time. For a stable system, $d(T)$ is expected to be zero on average and its variance can be written as

$$(50) \quad \sigma^2(T) = \mathbf{E}[d(T)^2] - \mathbf{E}[d(T)]^2$$

where \mathbf{E} denotes the expectation operator and since $\mathbf{E}[d(T)] = 0$

$$(51) \quad \sigma^2(T) = \mathbf{E}[d(T)^2] = \mathbf{E}[(R_1(T) - R_2(T))^2]$$

which is essentially the same definition proposed by [Allan \(1966\)](#) except for the one half factor.

$$(52) \quad \sigma_A^2 = \frac{1}{2}(\sigma^2(T)) = \frac{1}{2}\mathbf{E}[(R_1(T) - R_2(T))^2]$$

For a discrete set of samples, the Allan variance is computed as

$$(53) \quad \sigma_A^2(T) = \frac{1}{2(N-1)} \sum_{n=1}^N (R_{n+1}(T) - R_n(T))^2$$

where R_n are the sample averages. [Barnes et al. \(1971\)](#) showed that for noise spectral densities modeled as a power law

$$(54) \quad S(f) = f^{-\alpha}, \alpha = [0, 3]$$

where $\alpha = 0$ represents white noise, $\alpha = 1$ represents flicker noise typical of electronics devices and $\alpha > 1$ represents low frequency noise or drift, the Allan variance is proportional to $T^{\alpha-1}$ or

$$(55) \quad \sigma_A^2(T) \propto T^{\alpha-1}$$

However, in the case of $\alpha \geq 3$ equation 55 does not hold. A more accurate representation is obtained by describing noise by a correlation function as

$$(56) \quad g(\tau) = \mathbf{E}[s(t) * s(t + \tau)]$$

The Allan variance can now be written as follows

$$(57) \quad \sigma_A^2(T) = \frac{1}{T^2} \int_{-T}^T (T - |\tau|)(g(\tau) - g(T + \tau)) d\tau$$

In the case of small integration times T , the noise correlation function $g(\tau)$ can be expanded into a power series retaining only the first few terms as

$$(58) \quad g(\tau) = g(0) - \alpha\tau^\beta \pm \dots, \beta = 1, 2, \dots$$

Using equations 57 and 58 yields

$$(59) \quad \sigma_A^2(T) \propto T^\beta$$

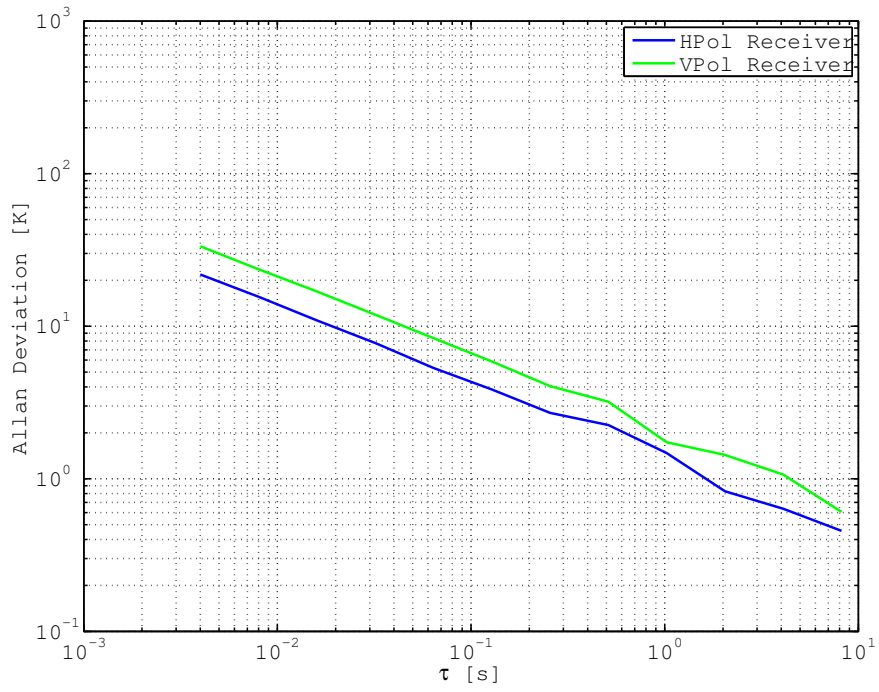
which when combined with equation 55 for a signal composed of white, flicker noise and drift results in

$$(60) \quad \sigma_A^2(T) = aT^\beta + \frac{b}{T} + c$$

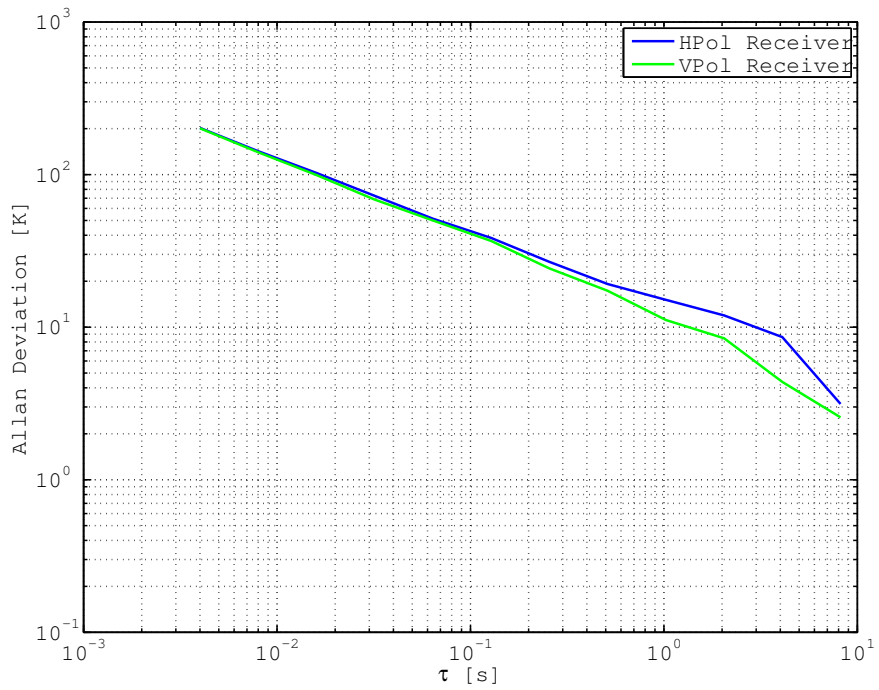
where a , b and c are constants and $\beta = \alpha - 1$. From this equation, it is easy to see how the Allan variance describes different types noise present in real world systems. For small integration times T , the variance decreases with T^{-1} as described by the radiometric sensitivity ΔT equation 46 and for larger integration times drift dominates described by the term aT^β . Flicker noise is represented by the constant c . Given these properties of σ_A , one can determine the optimal or largest integration time before flicker and drift begin to dominate. Figure 3.9 shows the results for integration up to 8 seconds for the Ku and Ka-band H and V polarized receivers. Note that the variance continues to decrease and the effects of flicker or drift noise are not evident. The observations were only carried out up $T = 8$ seconds due to limitations on the amount of data that could be transferred from the site at the time.

3.3. INITIAL TESTS USING THE PASSIVE CHANNELS ON THE D3R

Figures 3.10 and 3.11 show Ku-band reflectivity and system temperature $T_{SYS} = T_A + T_{REC}$ for data obtained during a PPI scan on June 11th, 2014 using a passive channel in total-power mode on the D3R system. Although measurements of T_{SYS} are uncalibrated, include noise contributions



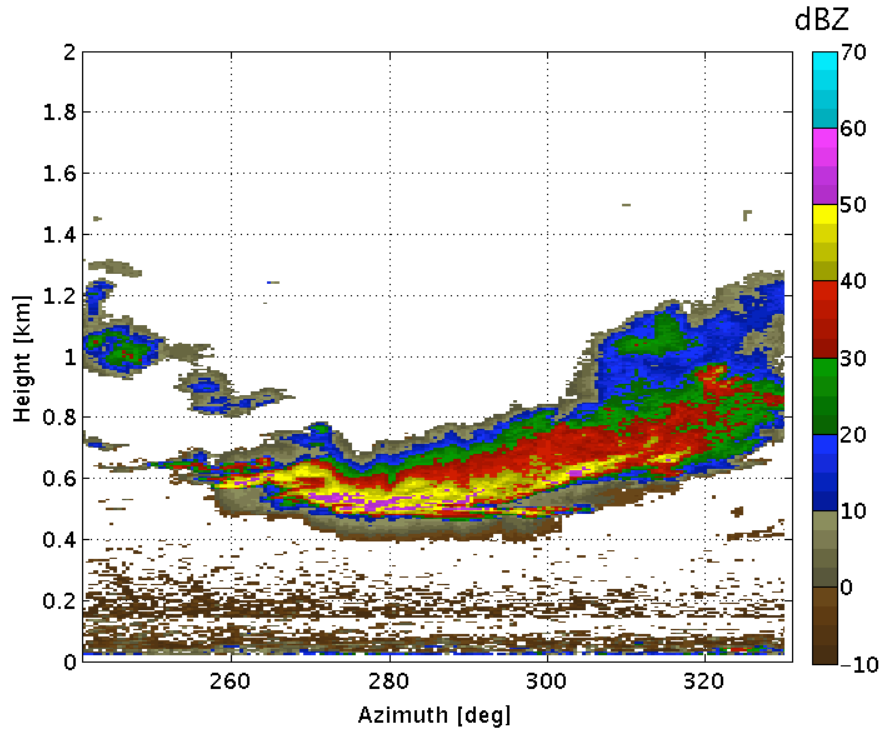
(A)



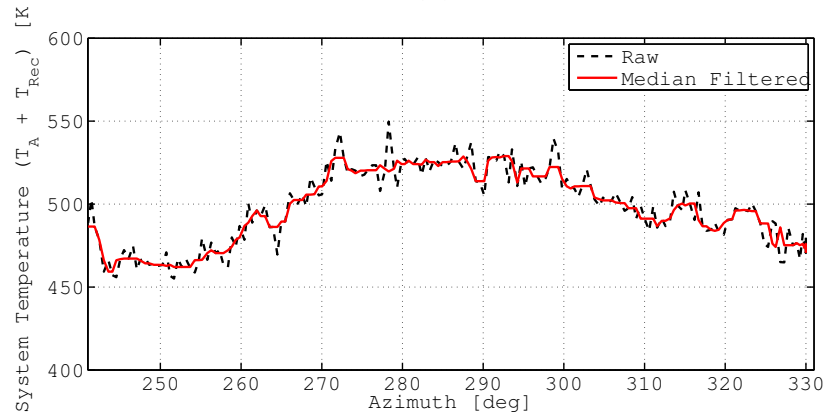
(B)

FIGURE 3.9. Ku (A) and Ka-band (B) receiver Allan variance for zenith pointing data collection.

by the receiver, T_{REC} , which need to be removed, they are encouraging. At the very least, the increase in T_{SYS} appears to follow regions of high reflectivity, the change towards a higher elevation seems to lower the overall minimum temperature which is consistent with side lobes viewing the ground and finally no major interference is easily noticeable which is a remarkable result given the measurement was made using the same receiver as the radar during regular operations but at a slightly different frequency. Chapter 5 describes the use of the D3R passive channels employing noise injection to track receiver gain changes followed by calibration and a case study.

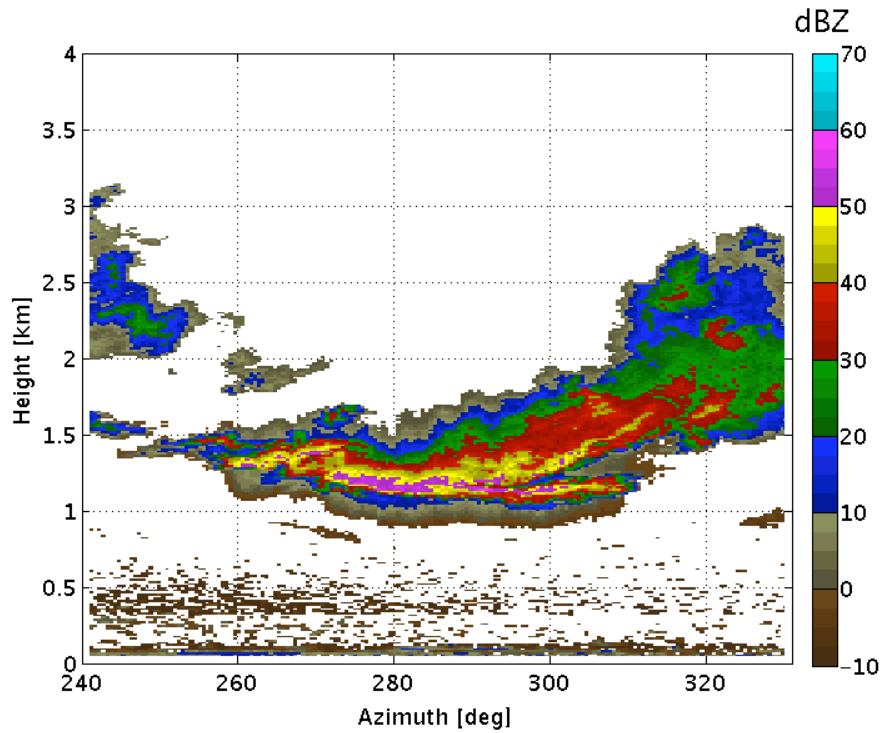


(A)

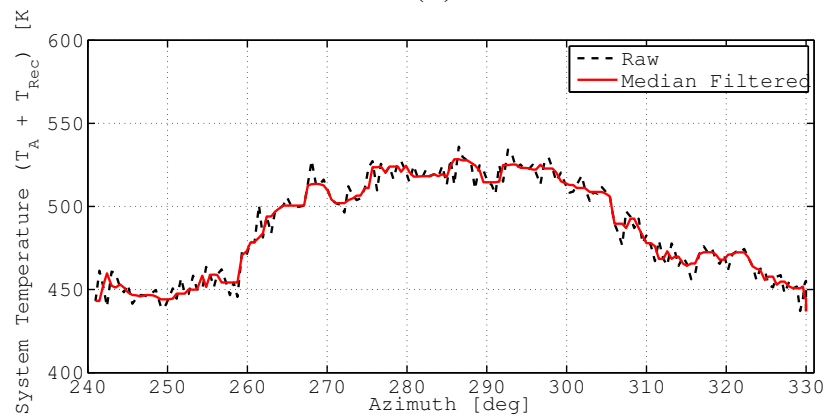


(B)

FIGURE 3.10. Ku-band reflectivity Z (a) and passive channel system temperature T_{SYS} in total-power mode (b) for a PPI scan at elevation angle of 2.36 deg on June 11th, 2014 at 17:42:31 UTC.



(A)



(B)

FIGURE 3.11. Ku-band reflectivity Z (a) and passive channel system temperature T_{SYS} in total-power mode (b) for a PPI scan at elevation angle of 5.27 deg on June 11th, 2014 at 17:42:57 UTC.

CHAPTER 4

DUAL-FREQUENCY DUAL-POLARIZED DOPPLER RADAR SYSTEM (D3R) - ENGINEERING AND FIELD PERFORMANCE

4.1. INTRODUCTION

The Global Precipitation Measurement (GPM) mission is an international partnership aimed primarily at two objectives, 1) the advancement in knowledge of the global water cycle and 2) the improvement of weather, climate, and hydrological prediction capabilities through more accurate and frequent measurements of global precipitation¹. Based on the success of the Tropical Rain Measurement Mission (TRMM), the GPM core satellite carries a Ku-band weather radar with the addition of a Ka-band radar. The Ka-band radar provides higher sensitivity than the Ku-band radar and is useful for measurement of snow and light rain.

The GPM dual-wavelength retrieval methods will be used to characterize two parameters of the raindrop size distribution. Having a similar dual-wavelength radar on the ground with the potential for in-situ and coordinated observations provides an excellent opportunity to develop microphysical models for microphysical retrievals. There are several assumptions used in the algorithms involving dual-wavelength methodologies discussed in the literature [Meneghini et al. \(1992\)](#); [Seto et al. \(2013\)](#); [Le and Chandrasekar \(2014\)](#); therefore, a beam aligned dual-wavelength system consisting of Ku- and Ka-bands will be very useful as a validation tool. In addition, if this system can be dual-polarized, the radar can be a self consistent cross-validation tool.

The considerations and specifications of a ground based dual-wavelength system are quite different from that of a space-borne system. In order for the space-borne dual-frequency retrieval to

¹Chapter content was published in [Vega et al. \(2014\)](#).

be successful, we need to understand the interaction between the microphysics and electromagnetics that generates the space-borne radar observations. The dual-polarization capability will enable additional microphysical insight into the interpretation of the dual frequency observations seen by the space-borne radar. Doppler observations are also becoming an increasingly integral part of microphysical interpretation [Moisseev and Chandrasekar \(2007\)](#). Thus the above discussion points towards a dual-frequency, dual-polarized, Doppler radar as the best candidate for ground validation (GV).

The Dual-Frequency Dual-Polarized Doppler Radar (D3R) was jointly developed by NASA Goddard Space Flight Center, Colorado State University, and Remote Sensing Solutions. This chapter describes the salient features of the D3R developed for the NASA GPM-GV program. It is organized as follows: Section [4.2](#) describes the architecture of the radar designed with the goal of participation in field deployments. Section [4.3](#) describes the subsystems of the D3R, namely the antenna subsystems, digital receiver, control and data processing, and the user interface. Calibration is an integral part of any radar system and those aspects of the D3R are described in Section [4.4](#). Finally, sample results from field deployments are shown in Section [4.5](#).

4.2. SYSTEM ARCHITECTURE

Since the GPM core satellite will be sampling precipitation at high latitudes, GPM-GV instrumentation is expected to be operational during field experiments spanning a wide range of environmental regimes with temperatures ranging from -40° to 40° C and wind loads up to 60 miles/hour. Furthermore, ground instruments need to survive the perils of being assembled and disassembled in less than ideal scenarios involving unexpected weather conditions, utility power loss, high winds, just to name a few.

A combination of requirements such as: widely varying operational temperatures, ease of deployment, ability to control remotely, etc., resulted in a decision to develop the radar using solid-state transmitters. Due to the comparatively low peak power output of solid-state transmitters as opposed to a magnetron or klystron, the radar system requires the use of pulse compression schemes to support the sensitivity requirement. Precipitation radar systems using solid-state transmitters are becoming increasingly viable [Li et al. \(2011\)](#); [Bharadwaj and Chandrasekar \(2012\)](#). Rapid strides made in semiconductor technology in the recent past have enabled the development of solid-state power amplifiers with sufficient power levels to serve as radar transmitters.

For a field deployable radar system, the solid-state transmitter solution offers several advantages including: no hot cathodes which eliminates warm-up time, lower system operating voltages, and improved mean time between failures. More recently, a class of frequency diverse wide-band waveforms were developed to mitigate the low peak power of solid-state transmitters as well as the range blind zone problem associated with pulse compression [Mudukutore et al. \(1998\)](#); [Carswell et al. \(2008\)](#); [Bharadwaj and Chandrasekar \(2012\)](#).

The D3R employs a frequency-diversity waveform consisting of three frequency spaced sub-pulses to achieve its sensitivity and minimum range. The three pulses and their associated pulse duration are: long ($40 \mu s$), medium ($20 \mu s$), and short ($1 \mu s$). The long and medium pulses are nonlinear frequency modulated signals with an overall signal bandwidth of 3.6 MHz. The D3R frequency-diversity waveforms have a restriction requirement on the transmit waveforms' spectra to avoid overlapping of the sub-pulse frequency bands. The digital receiver filter utilizes a minimum integrated sidelobe level (ISL) filter which has been shown to be excellent for weather radar applications [Bharadwaj and Chandrasekar \(2012\)](#). In the D3R system, minimum ISL filters are used for both long and medium pulses.

The D3R system, shown in Figure 4.1, was designed around the needs of the GPM-GV program. The radar system consists of two synchronized and co-aligned radar (one Ku and one Ka) integrated on a common positioning system mounted on a flatbed trailer. The technical specifications of the D3R are summarized in Table 4.1. Both radar systems are dual-polarized and equipped with independent solid-state transmitters and receivers to allow for polarization diverse transmission schemes. The antenna system is composed of two prime focus antennas that are co-aligned and possess well matched beamwidths. The antennas are mounted on an aluminum frame designed to keep angular deflections to within 0.1 degrees in any plane. The frame integrates both antennas, the RF transceivers, and IF analog/digital electronics onto the positioning system which minimized front-end losses and simplified the integration of the slip-ring assembly. These elements comprise the rotating subsystems shown in Figure 4.2. The positioning system consists of an elevation over azimuth configuration with scanning coverage of 360 degrees in azimuth and -0.5-90 degrees in elevation. The elevation limitations are physically set by the D3R design constraints, whereas the positioner design allows for elevation range of 0-180 degrees. The positioning system is equipped with two one-gigabit Ethernet connections as well as a 20A, 208-240 VAC circuit used to communicate and transfer power to the rotating subsystems shown in Figure 4.2. The positioning system also provides six differential signal pairs for timing, control, and housekeeping and an RF rotary joint for GPS signals.

The non-rotating subsystems group, shown in Figure 4.2, is composed of four 1U servers, a 64 TB (raw capacity) RAID storage device, one gigabit network switch, uninterruptible power system (UPS), dehydrator, and a 14 kW propane powered generator equipped with an automatic transfer switch. All servers, network switch, RAID storage, dehydrator, and UPS unit are housed in temperature controlled enclosures. Dry air from the dehydrator unit is cycled through the positioning

TABLE 4.1. Specifications of the Dual-frequency, Dual-polarized, Doppler Radar (D3R)

System	
Frequency	Ku: 13.91 GHz \pm 25 MHz, Ka: 35.56 GHz \pm 25 MHz
Minimum detectable signal	Ku: -8 dBZ, Ka: -3 dBZ. Noise equivalent at 15 km and 150 m range resolution.
Operational range resolution	150 m (nominal)
Minimum operational range	450 m
Maximum operational range	39.75 km
Angular coverage	0° - 360° Azimuth, -0.5° - 90° Elevation (full hemisphere)
Antenna	
Parabolic Reflector Diameter	Ku: 6 ft (72 in.), Ka: 28 in.
Gain	Ku: 45.6 dBi, Ka: 44.3 dBi
Half-power Beamwidth	Ku: 0.86°, Ka: 0.90°
Polarization	Dual linear simultaneous and alternate (H and V)
Maximum side-lobe level	\sim -25 dB
Cross-polarization isolation	< -30 dB (on axis)
Ka-Ku beam alignment	Within 0.1 degrees
Scan capability	0° - 24°/s Azimuth, 0° - 12°/s Elevation
Scan types	PPI sector, RHI, Surveillance, Fixed, Vertical pointing
Transmitter / Receiver	
Transmitter Architecture	Solid State Power Amplifier Modules
Peak Power	Ku: 200 W, Ka: 40 W per H and V channel
Duty cycle	30% maximum
Receiver Noise figure	Ku: 4.8, Ka: 6.3
Receiver dynamic range	\sim 90 dB
Clutter Suppression	GMAP-TD
Data Products	
Standard products	Equivalent reflectivity factor (Z_h), Doppler velocity (Ku unambiguous: 26.97 m/s)
Dual-polarization Products	Differential reflectivity (Z_{dr}), Differential propagation phase (ϕ_{dp}), Copolar correlation coefficient (ρ_{hv}), Linear depolarization ratio (LDR_h , LDR_v) (in alternate mode operation)
Data format	NetCDF

system and all boxes mounted on it to prevent condensation. System control tasks (e.g. on/off control, transmitter enable, digital I/Q time-series acquisition, and antenna control) are handled by the system control and data archiving node. Digital I/Q time-series received from the digital receivers are disseminated to the signal processing and archiving nodes through the time series streaming server. The time-series streaming server enables the processing and archiving of time-series data simultaneously without exceeding the slip-ring data transfer bandwidth. Each radar has its own



FIGURE 4.1. D3R system deployed in North Carolina for IPHEX GPM-GV field campaign.

signal processing node that handles the generation and archiving of data products in real-time. Real-time data products are then made available for display using the communication protocol defined for the VCHILL software [Chandrasekar et al. \(2005\)](#). Any authorized internet-connected user can have access to real-time data by using the platform independent VCHILL display software. The UPS and generator provide automated backup of the entire system in the event of a loss of utility power. They also decouple the setup process from site preparations since the radar can be fully integrated and tested without the need for utility power, which has served very well during deployments. The entire system is powered by a single 50 A, 208-240 VAC, 50-60 Hz circuit. Finally, the trailer is equipped with four outriggers with electric jacks used to level the platform and provide stability during high wind conditions.

In preparation for shipment, the antennas and IF electronics box (rotating subsystems) are disassembled with the assistance of a forklift and stored in crates. Both antennas are kept integrated to the frame during shipment so that co-alignment is maintained. The trailer can then be transported

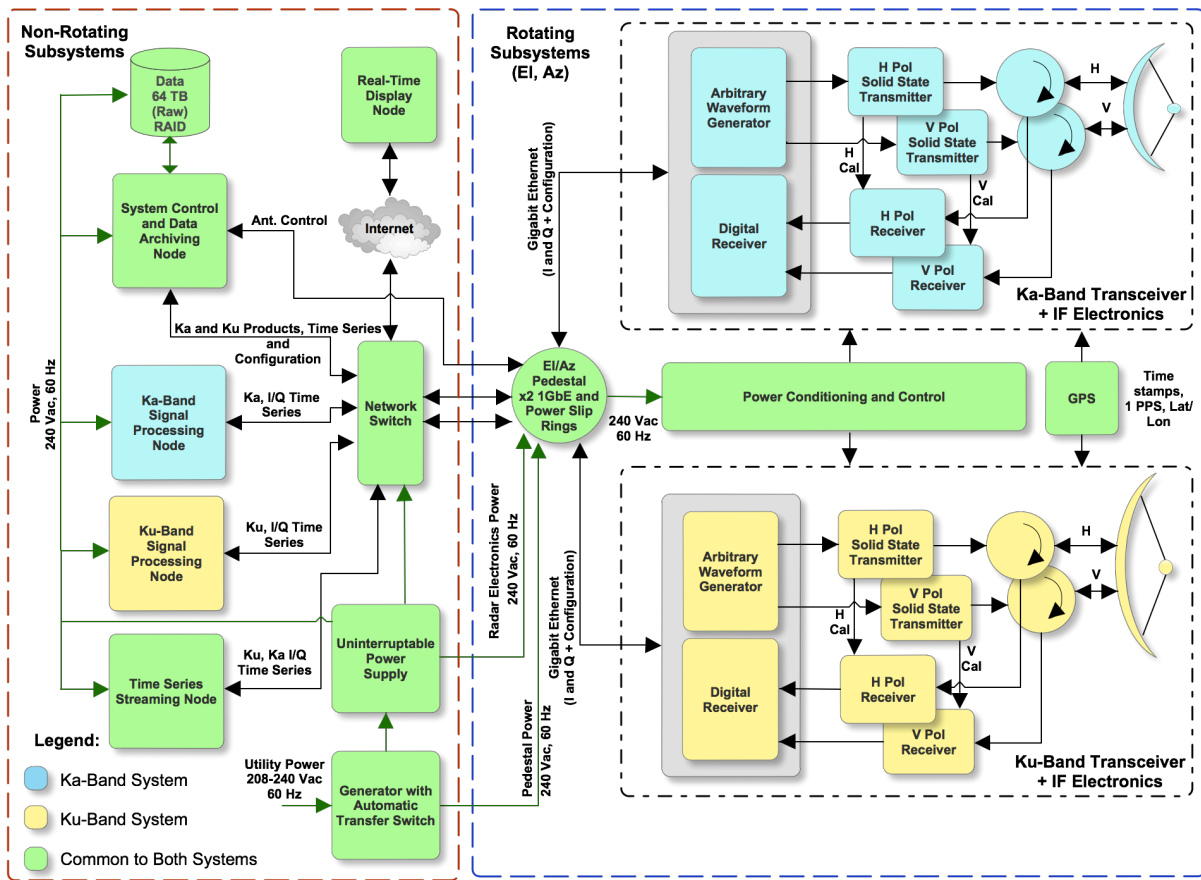


FIGURE 4.2. D3R system architecture diagram.

from site to site using a tow vehicle. The entire setup or teardown process is typically completed in one or two days.

4.3. D3R SUBSYSTEMS

The D3R can be divided into three subsystems, namely a) the antennas, b) waveform and digital receiver subsystem, and c) control and data processing system. The following subsections provide detailed descriptions of each of these subsystems.

4.3.1. Antennas

During the design phase, a dual-frequency, dual-polarized single aperture design was considered. However, estimated development cost and schedule at the time made it unfeasible. The antenna system employed on D3R consists of two dual linearly polarized prime focus parabolic reflector antennas. Four struts, each spaced 90 degrees in the ϕ dimension hold the feed in place. Waveguides are routed from the feed to the back of the reflector along the 45 and 315 degree strut members. The feed was designed to hold 2-3 psi of positive pressure, albeit our application does not require it due to the relatively low peak transmitter power. The reflectors are made of composite material, graphite over honeycomb, which makes them very lightweight and easy to handle when not integrated to the frame. To minimize the effects of wind loading, each antenna also includes an A-sandwich type radome. A hydrophobic coating is regularly applied to the radomes to prevent a water film from forming and therefore minimize attenuation effects as much as possible.

Dual-frequency ratio (DFR) is the difference of the reflectivity, Z , at two different frequency bands. In the case of D3R, DFR is defined as $Z_{Ku} - Z_{Ka}$. Dual-frequency ratio is one of the variables measured by the D3R system and special consideration was given to the beam-matching and co-alignment of the antennas. Figure 4.3 shows the Ku- and Ka-band overlaid H-port co-polarized antenna patterns. The half-power beam-widths for the Ku and Ka-band antennas are on average 0.86 and 0.90 degrees, respectively. This sets the azimuthal resolution at 30 km to approximately 470 m, which satisfied the requirement of it being ≤ 500 m. Overall, the Ku and Ka, peak sidelobe levels were below the required -25 dB level with the exception of the Ka $\phi = 90$ deg plane which had its peak at approximately -24.3 dB. To achieve co-alignment between antennas, provisions were made for four laser targets to be attached to the edges of both reflectors. The targets were used in combination with fine resolution pattern measurements to derive beam offsets using a laser tracker. During integration of the antennas with the frame assembly, laser tracker

measurements were used to determine beam co-alignment and shims were strategically applied to the Ka-band antenna until the Ka matched the Ku-band beam pointing. The final result was a co-alignment within 0.1 degrees in both azimuth and elevation. Please refer to the section on calibration, section 4.4, for co-alignment verification results.

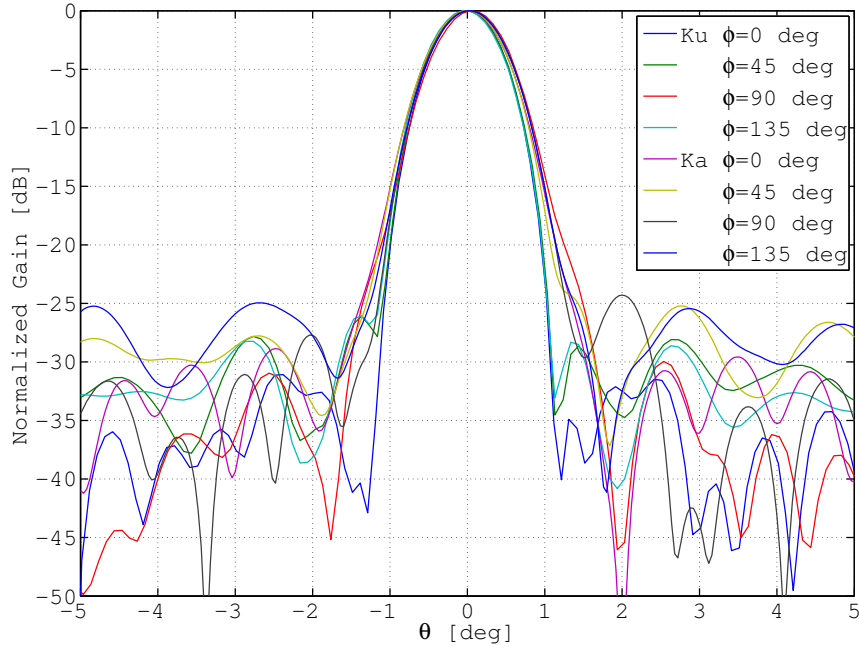


FIGURE 4.3. Ku, Ka-band H-port antenna co-polarized power (normalized) antenna patterns.

In addition to DFR measurements, polarimetric measurements such as differential reflectivity (Z_{dr}), differential propagation phase (ϕ_{dp}), copolar correlation (ρ_{hv}), and linear depolarization ratio (LDR) are all part of the capabilities incorporated into the design. The quality of the polarimetric variables are dependent on the antenna's polarimetric performance. Co-polarized H- and V-port pattern matching, cross-polarization isolation, and differential phase patterns are three parameters that have a significant effect on polarimetric variables [Mudukutore et al. \(1995\)](#); [Bringi and Chandrasekar \(2001\)](#); [Wang et al. \(2006\)](#). Figures 4.4 and 4.5, Ku and Ka respectively, show the co- and cross-polarized antenna pattern for the H- and V-ports in $\phi = 45$ and $\phi = 135$ degree planes

where feed strut blockage is present. Co-polarized beam matching was evaluated by integrating the two-way pattern over the main lobes (null-to-null) for each port and computing the percent difference between ports. A maximum percent difference of the patterns of 3.63% for Ku-band and -3.04% for Ka-band were found.

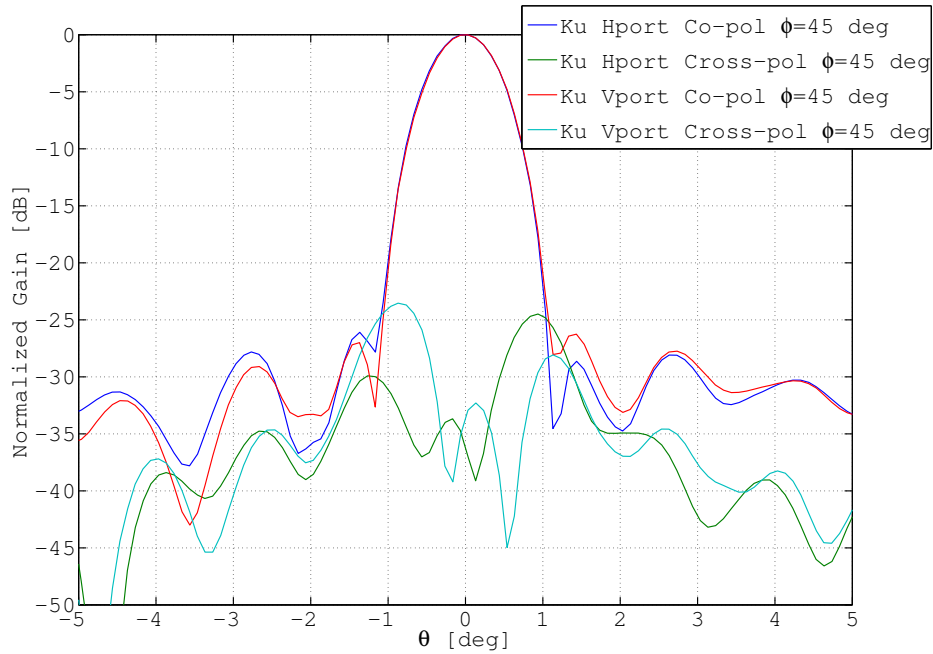


FIGURE 4.4. Ku-band H and V port antenna co- and cross-polarized power (normalized) antenna patterns for worst case cross-polarization plane.

The two-way integrated (main lobe, null-to-null) cross-polarization isolation, $ICPR_2$ Chandrasekar and Keeler (1993) is given by

$$(61) \quad ICPR_2 = 10 \log_{10} \left[\frac{\int f_{co} f_{cx} \sin \theta \, d\theta}{\int f_{co}^2 \sin \theta \, d\theta} \right]$$

where f_{co} and f_{cx} are the normalized co- and cross-polarized antenna power patterns, respectively. The worst-case plane for cross-polarization power of the Ku-band antenna is shown in Figure 4.4. The worst-case cross-polarization isolation is -29.13 dB for the H-port and -29.19 dB for

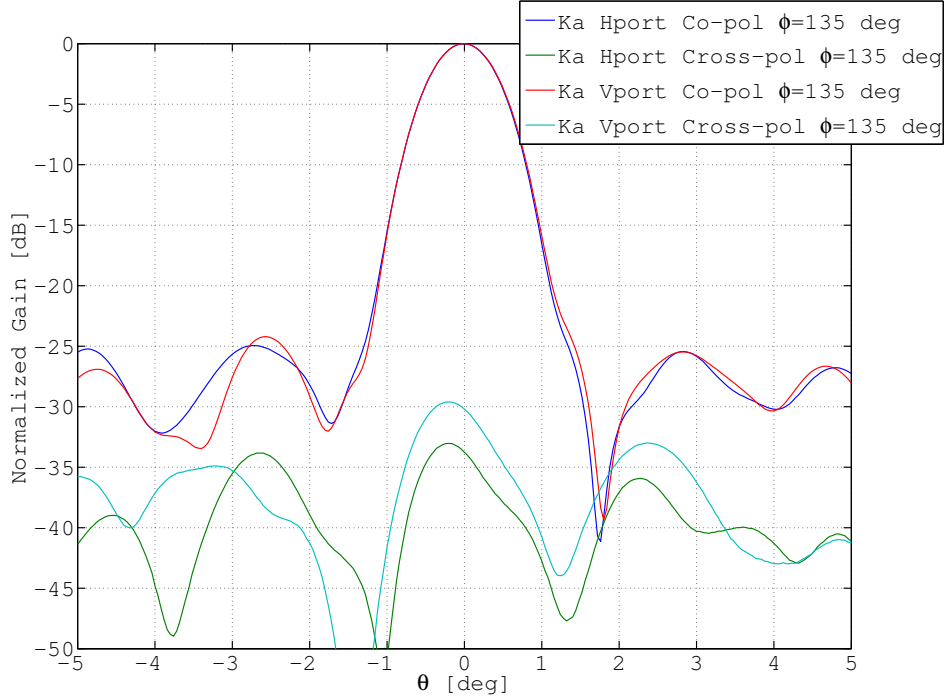


FIGURE 4.5. Ka-band H and V port antenna co- and cross-polarized power (normalized) antenna patterns for worst case cross-polarization plane.

the V-port. Similarly for the Ka-band antenna, Figure 4.5 shows the worst-case plane for cross-polarization isolation with -32.56 dB on the H-port and -29.02 dB for the V-port. Overall, the goal was to not exceed -32 dB cross-polarization isolation. However, after several adjustments and subsequent pattern measurements, both antennas were accepted as described.

Figures 4.6 and 4.7 show the differential phase plots of the Ku and Ka-band antennas respectively. The differential phase function for each plane was normalized to highlight excursions from a constant value along the main lobe. Deviations along the main beam have a detrimental effect on the measured $|\rho_{hv}|$. Equation 62 describes the antenna pattern effect on the measured $|\rho_{hv}|$. It can be seen that the effect is a function of the co-polarized pattern matching and differential phase as well. The antenna imposed $|\rho_{hv}|$ limit using the complex patterns for the D3R system were evaluated using equation 62 and found to be ~ 0.997 and ~ 0.999 , Ku and Ka respectively, which agree very well with measurements (please see section 4.5 for Ku and Ka histograms of $|\rho_{hv}|$).

$$(62) \quad |\rho_{hv}| = \frac{\left| \int \int e^{-j2(\Phi_h - \Phi_v)} f_h f_v d\Omega \right|}{\sqrt{\int \int f_h^2 d\Omega \int \int f_v^2 d\Omega}}$$

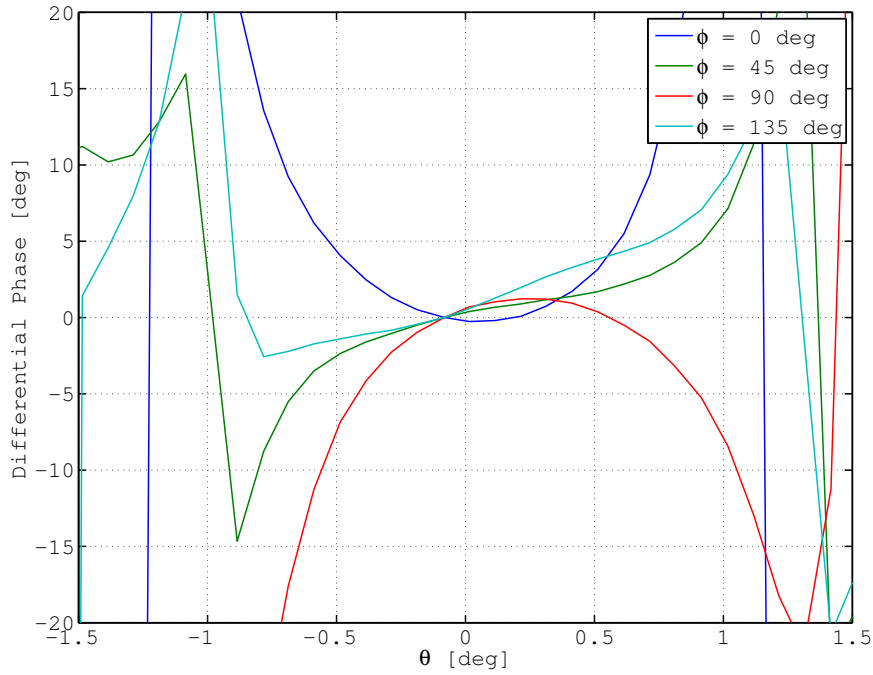


FIGURE 4.6. Ku-band differential phase (normalized) antenna patterns for $\phi = 0, 45, 90$ and 135 degree planes.

4.3.2. Waveform Generation, Transceiver, and Digital Receiver Subsystems

Advances in the area of RF solid-state power amplifiers (SSPAs) coupled with increased logic density in field programmable gate array (FPGA) chips during the definition stage of the D3R presented the possibility of adopting such technologies in the design of the transmitter, digital signal synthesis, and digital signal processing sub-systems. The use of pulse compression techniques becomes necessary in this type of design due to the low peak output power achieved with

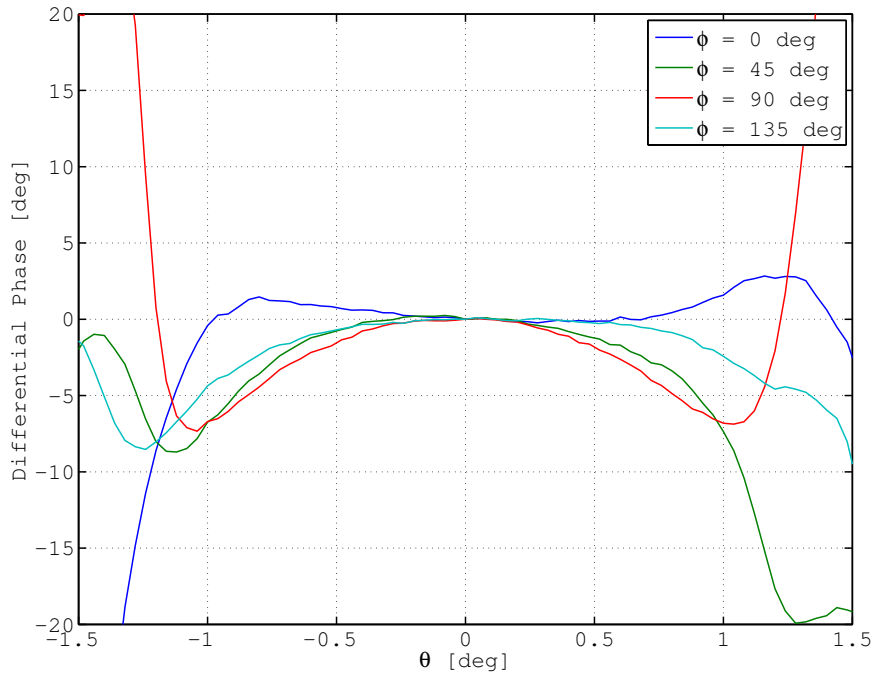


FIGURE 4.7. Ka-band differential phase (normalized) antenna patterns for $\phi = 0, 45, 90$ and 135 degree planes.

SSPAs in comparison to other classes of radar transmitters such as tube amplifiers, magnetrons, and klystrons. The SSPA solution provides wide bandwidth (in the context of weather radar) and allows for high operational duty cycles. This allows the possibility of using multiple frequency spaced and time multiplexed sub-pulses, including frequency modulated pulses, that enable sensitivities and blind ranges comparable to those attained with other types of transmitters requiring the use of high-voltage electronics.

Signal Path Description

Figure 4.8 shows the transceiver architecture implemented in both the Ku- and Ka-band sub-systems. To enable the measurement of all polarimetric scattering matrix elements, a dual-transmitter, dual-receiver configuration was adopted. Digitally synthesized transmit signals, centered at the first intermediate frequency (IF) of 140 MHz for each channel (H and V), are generated in the arbitrary waveform generator (AWG). Timing signals are also generated in the AWGs and will be discussed

in more detail in the following section. The transmit waveform is stored as digital I/Q value pairs at baseband with a sample rate of 50 MHz for each channel. The transmit waveform is downloaded to the AWG's on-board memory via a USB interface using a single-board computer (SBC) which also hosts the digital receiver (DRX). The AWG uses quadrature digital up-converters (DUCs) with built-in 14-bit digital-to-analog converters (DACs) to interpolate and translate the loaded baseband waveform to a center frequency of 140 MHz at a sample rate of 1 GHz. This stage is followed by IF section 1, which includes filtering, amplification, and mixing stages to convert the signal from the 140 MHz IF to the second IF of 220 MHz for Ku-band and 920 MHz Ka-band. The 360 MHz and 780 MHz signals used in the first and last mixing stages are generated by phase-locked coaxial resonator oscillators combined with four way splitters. IF stage 2 is followed by another set of filtering, amplification, and mixing stages arriving at the final operating frequencies of 13.91 GHz for Ku and 35.56 GHz for Ka. The transmitter RF section performs the final filtering stage, with pre-amplifier also included on Ka-band, prior to entering the SSPAs. The mixing signal of 13.69 GHz on the Ku-band transceiver is generated from a phase-locked dielectric resonator oscillator and the 34.64 GHz on the Ka-band is generated from a 17.32 GHz oscillator of the same type which is then split four ways and fed into four x2 multipliers with filtering stages prior to entering the mixers.

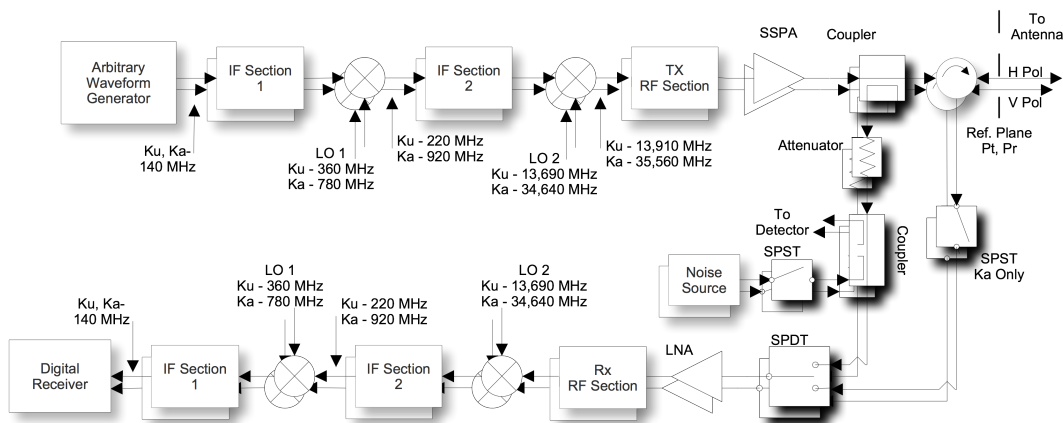


FIGURE 4.8. Ku, Ka-band transceiver architecture block diagram.

The front-end section of both transceivers contains the SSPAs, calibration path components, duplexer and low noise amplifier (LNA). The SSPAs peak output power for each polarization channel is approximately 200 W for the Ku-band and approximately 40 W for the Ka-band. Both sets of SSPAs are equipped with internal temperature compensation for gain and high speed on/off switching. Temperature compensated gain control prevents major drifts in system transmit power due to thermal cycling and the high speed on/off capability provides a means to shutdown the internal bias to all power modules after the transmit period is completed. This has two major advantages over an “always on” approach: 1) less power consumption and therefore less heat generation and 2) thermal noise leakage into the receiver during the receive mode is minimized without the need for additional high power switches.

Once the transmit waveform is amplified by the SSPA, it is coupled into the receiver through a calibration channel which provides a means to track and compensate for gain drifts in the transmitter and receiver [Durden et al. \(1994\)](#); [McLinden et al. \(2008\)](#); [Vega et al. \(2012\)](#); [Ulaby et al. \(2014b\)](#). The selection between the receive and calibration path is performed through a single pole double throw (SPDT) switch implemented using PIN diodes on the Ku and latching circulators on the Ka. Since leakage through the circulator and reflections from the antenna ports will add coherently to the calibration signal, over 40 dB of isolation is needed between the calibration and leakage/reflection signals for a transmit power measurement corruption of less than 0.1 dB. On the Ku, the PIN diode based SPDT provided enough isolation to meet the desired calibration-to-leakage ratio. On the Ka, an additional single pole single throw (SPST) switch (also implemented using latching circulators) was added to meet the isolation requirements. An attenuator is used to set the sampled power level well below the receiver saturation point (approximately 75-80 dB of total calibration path attenuation) followed by another coupler with a square law detector which provides a quick and independent method to measure the transmitter power during system checks.

A noise source with an excess noise ratio (ENR) of 27 dB for Ku and 22 dB for Ka is coupled into the receiver as well for independent receiver gain tracking. During a typical transmit/receive cycle, the SPDT switch is set to the calibration path, the noise source switch is closed for several microseconds followed by the enabling of the SSPAs, and triggering of the AWGs which results in the sampling of the transmitted waveform. The SSPAs are then disabled and the SPDT is returned to the receive path. This process is repeated on a pulse-by-pulse basis.

Received signals are routed from the antenna to the receiving path where they are initially amplified by LNAs with approximate noise figures of 1.2 and 2.6 dB and gains of approximately 26 and 21 dB for Ku and Ka, respectively. The LNAs are followed by several component stages which are in common with the transmitter calibration loop until they reach the digital receivers.

The digital receivers employed are based on a PCI Mezzanine Card (PMC) equipped with four (only two are used) 16-bit analog-to-digital converters (ADCs), signal processing and PCI bridge FPGAs, and general purpose I/O (GPIO). This card is hosted by a compact PCI single board computer (SBC) housed in a 1U, nineteen inch rack mountable chassis. Signals received from all three sub-pulses are digitized and divided into three sub-channels where they are processed by quadrature down-conversion stages, decimating filters and ending in either matched filters or pulse compression filters. Digital I/Q data is then transferred from the DRX to the SBC via a PCI bus where it is tagged with GPS derived time stamps and location, antenna position, scan type, transmitter state, and other metadata required by the signal processing nodes.

Timing and Clock Interface Description

The Ku and Ka band systems are synchronized to a common 10 MHz stable local oscillator (STALO). The 10 MHz STALO clock source is used to generate the radio frequencies (RF), intermediate frequencies (IF), and the digital receiver ADC sampling clock. A diagram of the clock distribution is provided in Figure 4.9. A GPS module provides radar location information, UTC

time-stamp information, and a synchronization pulse at 1 pulse per second (PPS) that is common to both the Ku- and Ka-band receivers. The arbitrary waveform generator (AWG) generates the requisite triggers and timing delay for the transceivers and digital receiver (DRX). The precise timing from the AWG is used to coordinate the calibration sources within the transceiver, SSPA control, and the synthesis of transmit waveforms. The Ka AWG trigger is slave to the Ku AWG trigger to allow synchronized transmission and acquisition of both Ku and Ka radars.

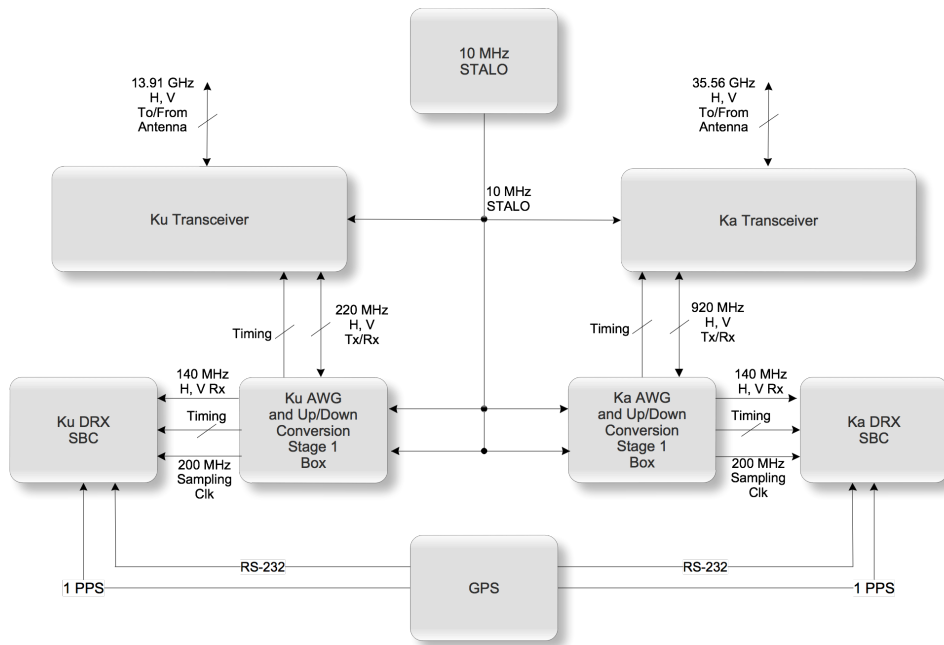


FIGURE 4.9. System timing and clock generation block diagram.

4.3.3. Control and Data Processing System

The radar control and data processing can be subdivided into three subsystems: antenna control, RF control, and data processing. These three subsystems interact with one another and provide state information for data processing. The subsystems are integrated into a single point of control provided as a user interface. Antenna control is common for both Ku and Ka, while the RF control and data acquisition are logically separated for the Ku- and Ka-bands. Synchronous transmission of both frequencies is achieved by operating the Ka trigger generator as a slave device to the Ku

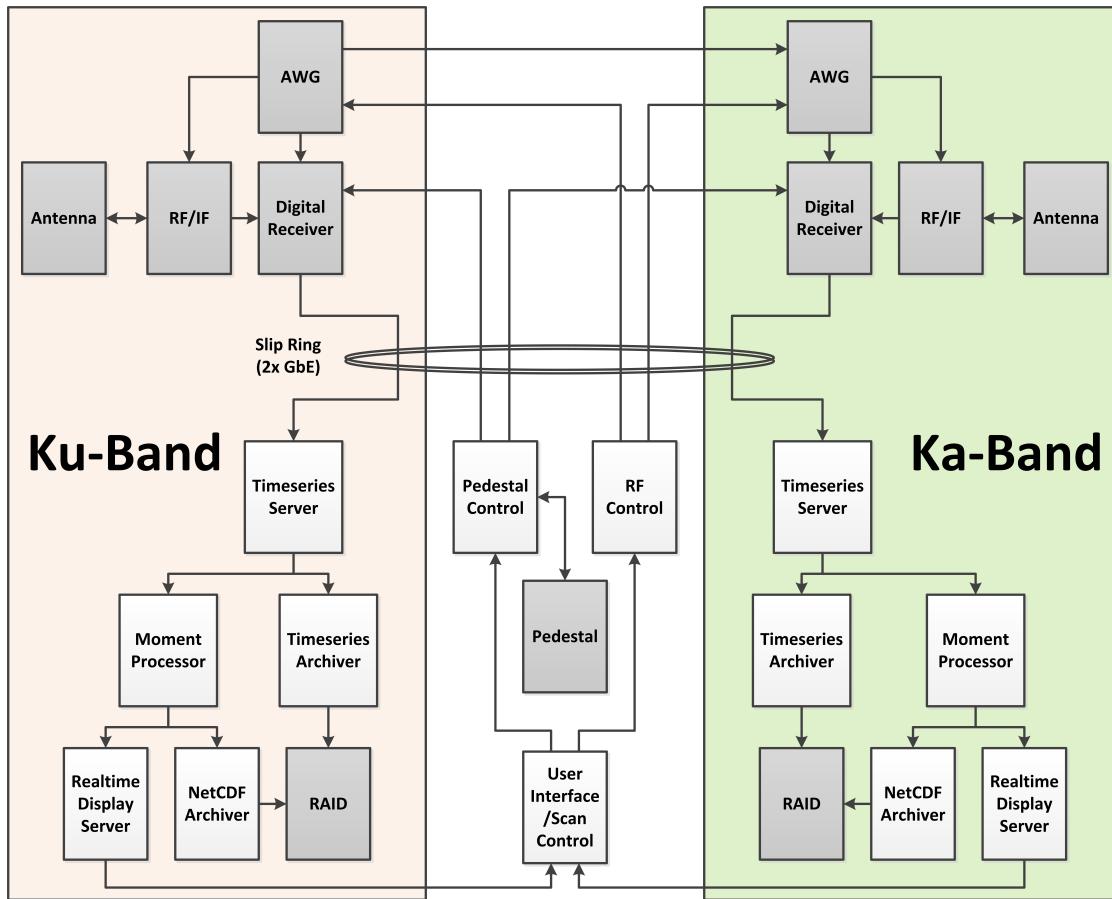


FIGURE 4.10. D3R software system diagram. Dark gray boxes represent hardware or firmware devices. Light gray boxes represent software modules running on general purpose servers.

trigger generator. All hardware devices are individually powered and remotely controlled through an Ethernet-enabled power distribution unit (PDU). The PDU provides power sequencing capability and remote fault recovery in the event of a system power issue. Due to the network-driven architecture, the D3R can be remotely operated, without limitation, via an Internet connection.

In Figure 4.10, the IF box houses the common 10 MHz local oscillator, Ku- and Ka-band arbitrary waveform generators (AWGs), and Ku- and Ka-band digital receivers (DRXs). Both of the DRXs have dedicated gigabit Ethernet connections, via the pedestal slip ring, to their respective data processing servers. RF control and a portion of the housekeeping functions share the gigabit Ethernet connections for control and monitoring of the system. The D3R system uses a redundant

array of inexpensive disks (RAID) to provide both fault tolerance in the archiving of data and to meet the data bandwidth requirements for data archiving time-series I/Q data. The RF/IF hardware is controlled by the precise timing of the AWG. The AWG is responsible for all timing, triggers, and transmit waveform generation. The digital receiver is implemented with an FPGA acquisition board running on a Linux-based single board computer. All movement of the radar system is controlled by the trailer mounted pedestal.

Antenna Positioning

Antenna positioning is accomplished by controlling the pedestal. The pedestal is scanned by providing start and stop azimuth and elevation coordinates, direction of movement, and movement rate. The pedestal state can be queried to monitor the current position and status information. Complex scans can be generated by executing a sequence of move commands. The pedestal hardware provides a serial communication interface for all communications. A serial-to-Ethernet adapter is used to allow pedestal control to be managed from any networked computer. A dedicated service is run on a general purpose Linux server as the pedestal controller. The pedestal controller service provides a managed interface for all other servers or services to access the pedestal state and control the pedestal. This implementation allows for the arbitration of multiple clients to the pedestal resources.

RF Control

All RF control is enabled via the AWG. The AWG allows for detailed timing and trigger generation, the configuration of waveform input, pulse-by-pulse transmit phase control, pulse repetition period (PRT) timing, PRT mode selection, and enabling and disabling transmit triggers. With proper configuration of the AWG timing, various polarization states and PRT sequences are generated to enable any transmit polarization modes with either a uniform PRT or non-uniform PRT scheme, such as a staggered PRT waveform.

D3R operates with the Ku-band AWG as the master trigger source and the Ka-band AWG as a slave device that generates the Ka transmit trigger when the Ku-band trigger is generated. D3R's standard operating mode is simultaneous transmit and receive (STAR) of both polarization channels, with $400\ \mu\text{s}/600\ \mu\text{s}$ staggered PRT. For uniform PRT, a $500\ \mu\text{s}$ period is used.

Data Processing

As discussed previously, the D3R's digital receivers are implemented using an FPGA-based analog acquisition board hosted by a single board computer running Linux. The digital receiver encodes the system status and position in the time-series data structures it sends to the moment processor, however the digital receiver does not use this data itself. The digital receiver also encodes information about the operating mode of the AWG, making information such as the polarization mode and PRT selection available to the moment processor to correctly process the the digital I/Q data.

The data processing is performed using general purpose servers running the Linux operating system with proprietary radar data processing software. Gigabit Ethernet connections are used to share data between the digital receivers and processing servers. The data processing software is divided into functional modules with network-enabled interfaces for data transport. This allows the data processing to be balanced and distributed over multiple servers.

The FPGA-based digital receiver implements a multi-frequency pulse compression design to allow the use of three independent, frequency-separated sub-pulses. The three center frequencies are separated by 15 MHz, with a 10 MHz channel bandwidth each. The typical range side-lobe level is illustrated by the pulse compression filters for the Ku and Ka medium pulse in figures 4.11 and 4.12. It can be seen from this figure that the typical range side-lobe levels are of the order of -49 and -47 dB, Ku and Ka respectively, and they uniformly fall to less than -85 dB at farther range delays. These three sub-pulses are designed to work together to maximize the radar's sensitivity

while mitigating the blind range limitations inherent to pulse compression. The digital receiver acquisition board directly samples the IF frequency and provides a time-series data stream, which includes the radar state information and digital I/Q data of the three sub-pulses for the entire pulse acquisition time.

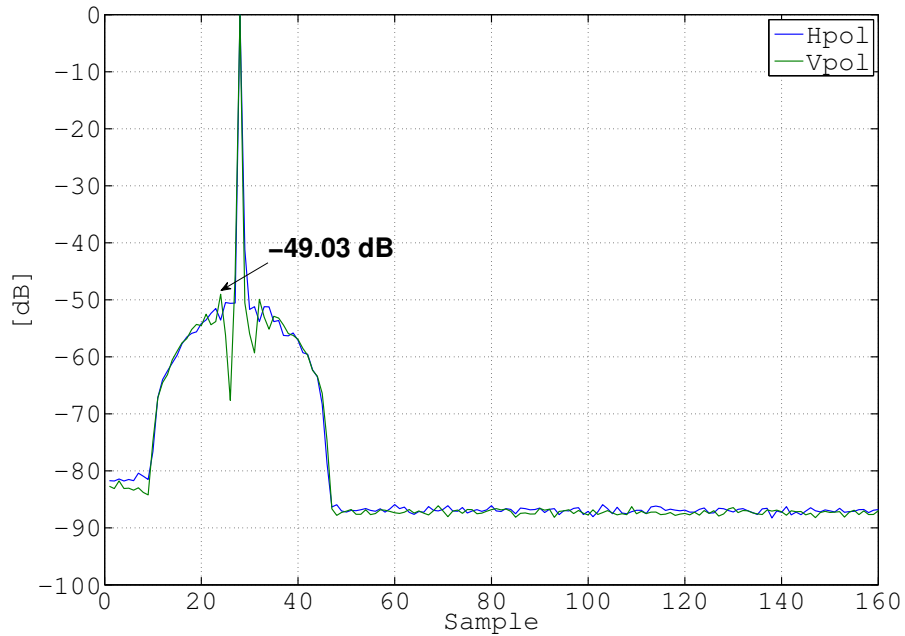


FIGURE 4.11. Ku-band pulse compression waveform and filter response for the medium pulse illustrating range sidelobes.

The digital receiver computer transfers the time-series data via Ethernet through the pedestal slip ring to a time-series server. The time-series server is used as a first-in, first-out buffer between the digital receiver and all time-series consumers. The time-series server provides fan-out of the time-series data to maintain the minimum data bandwidth load through the pedestal slip-ring, which presents a network bandwidth bottleneck. Any consuming software client that requires time-series data can connect to the time-series server without increasing the network load on the digital receiver. The moment processor and time-series archiver are two consumers of the time-series data stream.

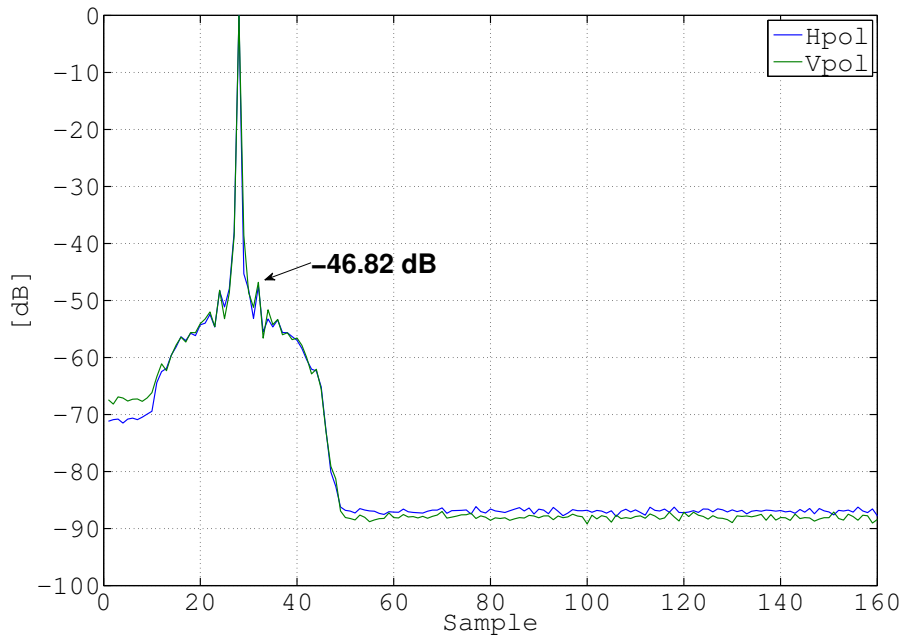


FIGURE 4.12. Ka-band pulse compression waveform and filter response for the medium pulse illustrating range sidelobes.

The radar moment processor uses the Gaussian model adaptive processing in the time domain (GMAP-TD) clutter suppression algorithm [Nguyen and Chandrasekar \(2013\)](#) at its core. The main concept of the GMAP-TD method is to design a time-varying filter matrix to attenuate the clutter signal to a level comparable to the noise. The processing methodology is similar to the original GMAP filter [Siggia and Passarelli \(2004\)](#), but all processing is performed in the time domain. Therefore, it overcomes the disadvantages associated with spectral processing methods, such as the effect of spectral leakage caused by finite data length and the effects of aggressive time domain weighting functions have on the estimation of signal moments. GMAP-TD can be directly extended for use with staggered PRT waveforms with minimum modification. The GMAP-TD algorithm provides a computationally tractable and stable clutter filter solution for staggered PRT operation.

The dual-polarized staggered PRT pulse scheme [Golestani et al. \(1995\)](#) (please see [Zrnich and Mahapatra \(1985\)](#) for the single polarized version) is used to alleviate the range-velocity ambiguity

problem. The maximum unambiguous velocity is determined by $V_a = \frac{\pm\lambda}{4T_u}$. For staggered PRT, $T_u = T_2 - T_1$ with $T_2 > T_1$. For a uniform PRT, $T_u = T$. It is easily shown that for a two-thirds staggered PRT ratio, the unambiguous velocity range is 2.5 times greater than a uniform PRT with the same effective PRT given by $T_e = \frac{(T_1+T_2)}{2}$. The PRT timing modes used on the D3R are shown in figure 4.13. Both staggered and uniform PRT pulse schemes are supported. For staggered PRT, a two-thirds timing scheme is used. The alternate transmit simultaneous receive staggered PRT waveform proposed for the D3R is shown in figure 4.13.

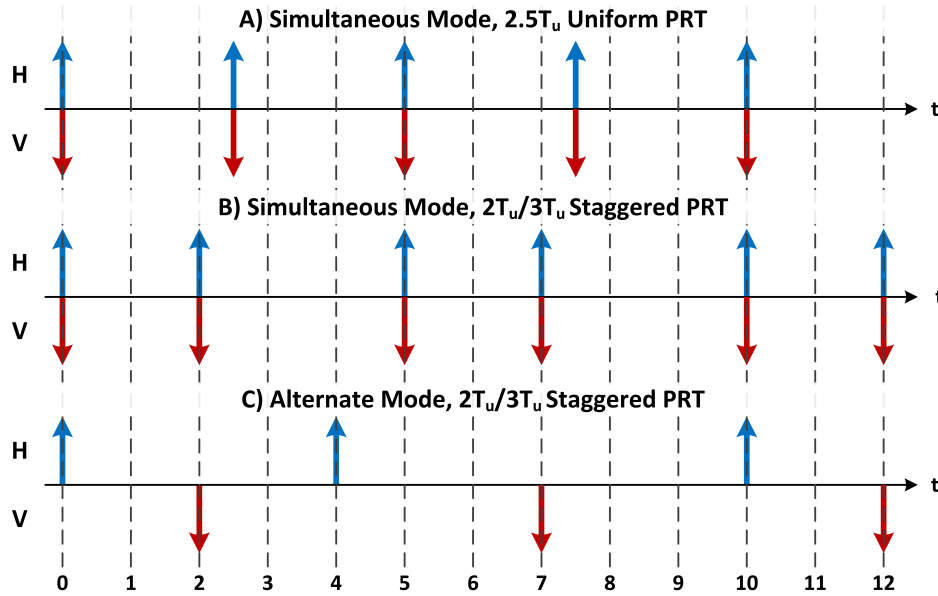


FIGURE 4.13. D3R pulse schemes for simultaneous mode with both uniform PRT (A) and staggered two-thirds PRT (B). The uniform PRT and staggered two-thirds PRT waveforms yield the same effective sampling rate over a ray integration cycle. The alternate mode staggered PRT pulse timing for D3R is illustrated in (C).

The D3R's moment processing code dynamically detects the radar operation mode on a ray-by-ray basis. The radar and processing control parameters are fully customizable. The moment processing allows for online calibration and measurements of an internal RF noise source and measurements of the transmit power via the transceiver calibration mechanisms. The online calibration allows for improved accuracy of reflectivity and Z_{dr} by compensating for system variations.

The radar moment data from the moment processor is archived to disk using the Network Common Data Form (NetCDF) 4 format with a D3R-specific data structure. The radar moments and additional radar state information are archived for each processed ray. Each NetCDF file contains a single radar sweep.

User Interface

The D3R operation is provided by a user computer that interfaces to the radar control software and data streams through a network connection to the appropriate D3R servers. Scan files can be configured and executed via a command line interface or a graphical user interface. All system control and system status information is similarly accessed. The D3R system status information includes component temperature and voltage monitoring, available data storage capacity, pedestal health and telemetry, AWG and transmitter state, and scan progress. Individual sweeps are grouped into a stack or volume scan. Multiple stacks can be dynamically combined to create ever more complex scan profiles. A scan period can be defined to regularly execute scans at a predefined interval.

The real-time display server, as the name implies, provides a real-time look at the generated radar moments and telemetry. The real-time display provides the radar operator a view of current radar observations. The real-time display provides limited data manipulation, such as data filtering and zooming. An example image of the real-time display software control panel is in Figure 4.14. The control panel provides a list of available moments to display as well as configuration for the display. Figure 4.15 is an example of the Ku reflectivity real-time display window available to the radar operator.

4.4. SYSTEM CALIBRATION

System calibration is performed and verified on multiple levels depending on the susceptibility to variation and sensitivity of the system's performance to that variation [Chandrasekar et al.](#)

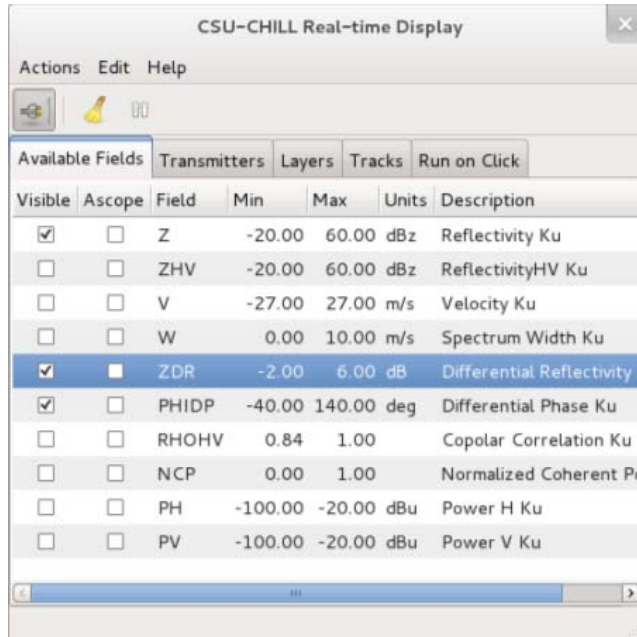


FIGURE 4.14. D3R real-time display control panel. Two control panels are provided; one for Ku and one for Ka.

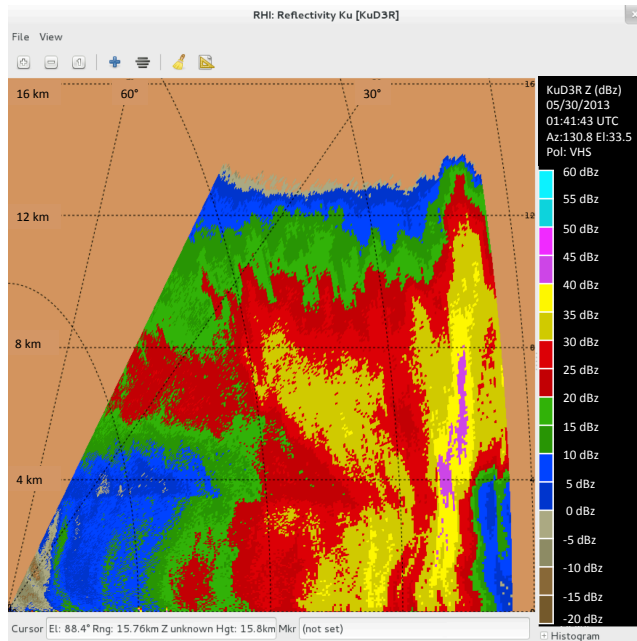


FIGURE 4.15. Example real-time display of Ku-band reflectivity for an RHI scan.

(2013). Electrical and mechanical components undergo parameter variation due to many effects including: aging, temperature, humidity, voltage, and environmental contamination. The following subsections describe antenna co-alignment verification, absolute reflectivity calibration using a

metal sphere, internal transceiver calibration for transmit power variation, and the use of vertically pointing scans to remove Z_{dr} bias.

4.4.1. Antenna Co-alignment

Antenna alignment is determined by the plane of the antenna frame and may be adjusted with shims on four points at the antenna mount points. The co-alignment of the Ku and Ka antennas is periodically verified using the sun as a reference point. This provides a systematic and repeatable method of characterizing and verifying the co-alignment of the two antennas. The solar received power for Ku and Ka as a function of azimuth and elevation relative to the sun's location are shown in Figure 4.16. The data from which these images were generated can be used to determine the absolute pedestal position error as well as evaluate the antenna co-alignment. Figure 4.17 shows 3 dB contour lines generated from a second order polynomial surface fitted to the received power data of Figure 4.17. The contour lines of the Ku and Ka antennas are shown with respect to the pedestal's position relative to the sun. Perfect alignment would have the contour lines concentric. It can be noted that during this solar observation from May 18th, 2013 at approximately 23:50 UTC, the difference between the co-alignment is 0.01 degrees in azimuth and 0.13 degrees in elevation. The bias in the contour's maximum value indicates an absolute pedestal position error.

4.4.2. Sphere Calibration

Sphere calibration data, performed on June 14th, 2013 starting at 00:00 UTC, is shown for Ku-band in Figure 4.19 and Ka-band in Figure 4.20. A 10 inch metal sphere tethered to a weather balloon filled with helium was released and tracked initially using a theodolite until it was detected and tracked using the real-time displayed reflectivity data. The figures present raw results prior to

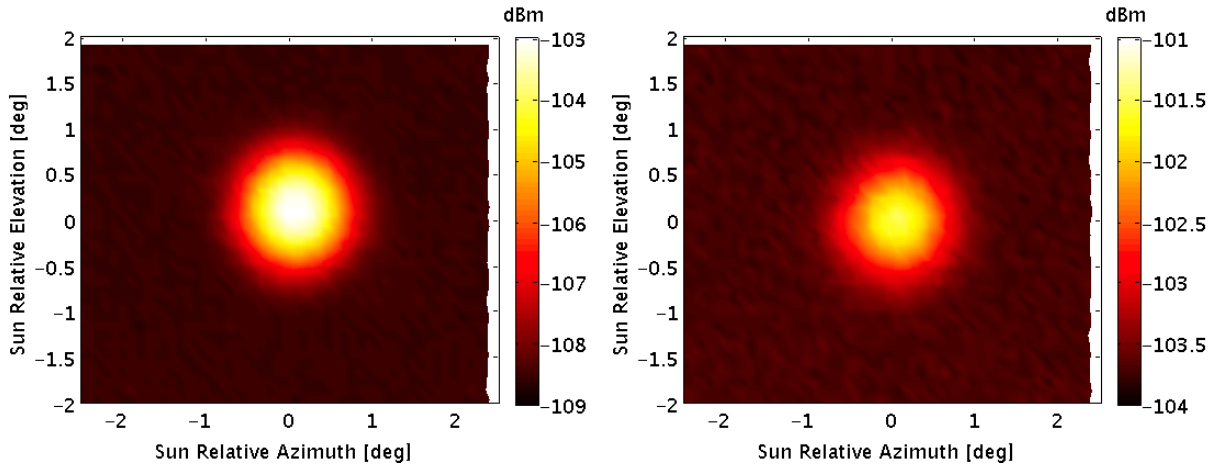


FIGURE 4.16. Ku- (left) and Ka-band (right) solar received power with position relative to the center of the sun.

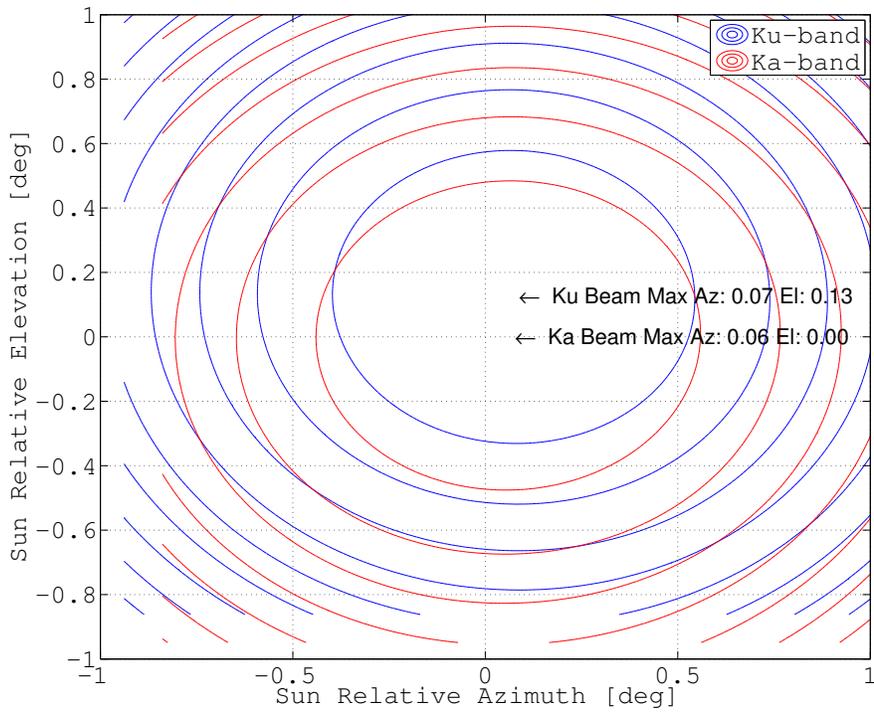


FIGURE 4.17. 3 dB contour lines of the 5 parameter model fitted to the Ku- and Ka-band solar received power. The azimuth and elevation are relative to the center of the sun during the scan. This plot provides information on the absolute pedestal position error as well as co-alignment of the Ku and Ka antennas.

any corrections being made to account for system reflectivity biases. Therefore, they are purely based on previously measured system parameters and the internal calibration channels. Figure 4.19 shows the observed power measurements, given the D3R specifications, of a metal sphere of the same diameter to the one launched at various ranges from the radar. The analytically derived expected power observation for a metal sphere of the same diameter is included as a solid curve. A metallic sphere with a diameter, d , in the optical regime ($\lambda \ll d$) provides a known, constant, isotropic radar cross section that can be used to as a system level calibration of the radar. Figure 4.18 shows the cross section for the sphere used. Note how at D3R wavelengths, oscillations in the optical regime are minimal (≤ 0.1 dB) making the target cross section calculation resilient to errors in dimension measurements. The metal sphere calibration provides a complete end-to-end system calibration for reflectivity [Bringi and Chandrasekar \(2001\)](#). Figure 4.19 shows remarkable agreement with theoretically expected values showing that the radar is well calibrated. The difference error is provided on the right side axis and shows that on average, the radar calibration is accurate to within 0.5 dB. Figure 4.20 shows similar results for Ka-band and that it is also calibrated to within 0.5 dB of accuracy.

4.4.3. Transceivers

The transceivers implement a single pole, double throw (SPDT) switch to allow the receiver to sample a noise source as well as the transmitted waveform. The transmit power measurements are used to compensate for variations in the SSPAs' power output. Variations in transmit power, if not compensated for, directly impacts the accuracy of Z_{dr} as transmit power drift for the H and V polarization channels are not necessarily correlated. The accuracy of reflectivity measurements are similarly affected by variation in transmit power. The implementation of transmit power measurements via the calibration loop also includes gain drift in the receive path. From equation 63,

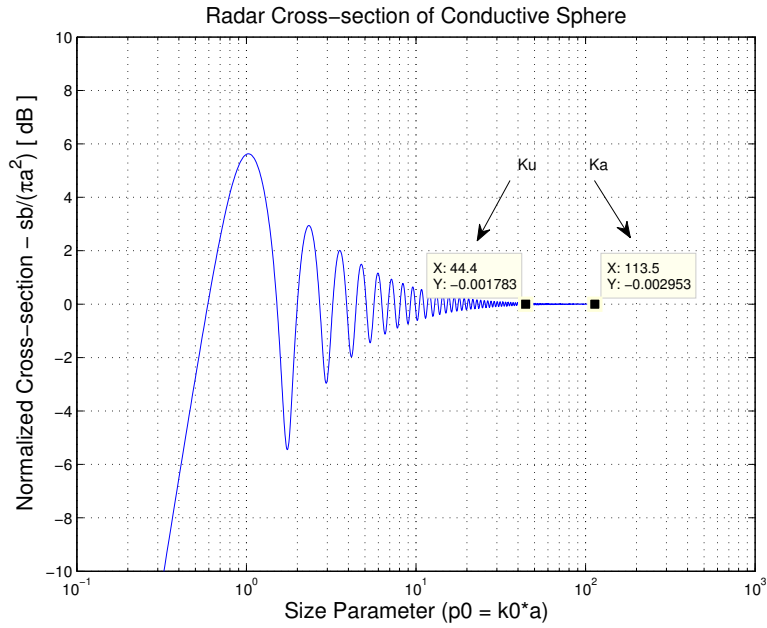


FIGURE 4.18. Conductive sphere radar cross section at D3R wavelengths.

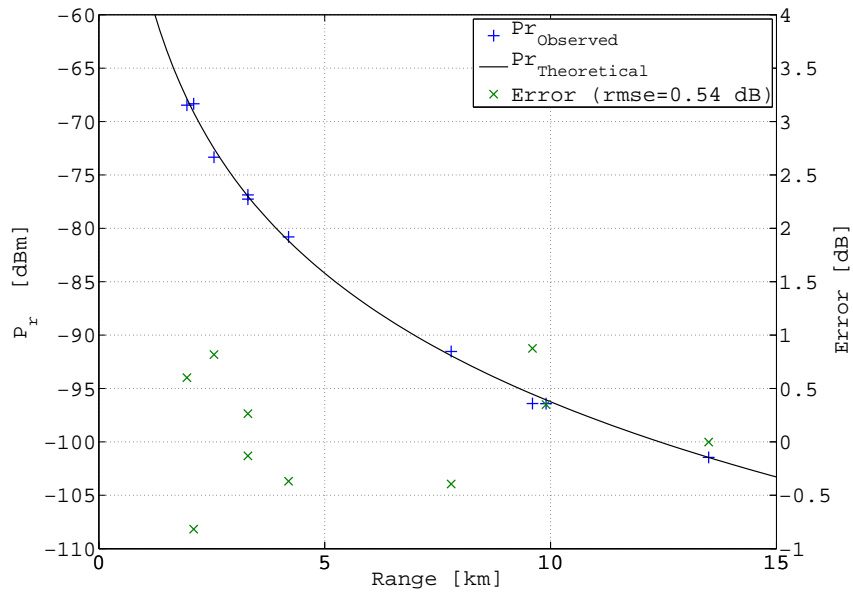


FIGURE 4.19. Ku-band sphere calibration from June 14th, 2013 starting at 00:00UTC. The graph shows measured sphere reflectivity and the theoretical reflectivity curve of a metal sphere of the same diameter. No corrections were made to this data based on calibration results.

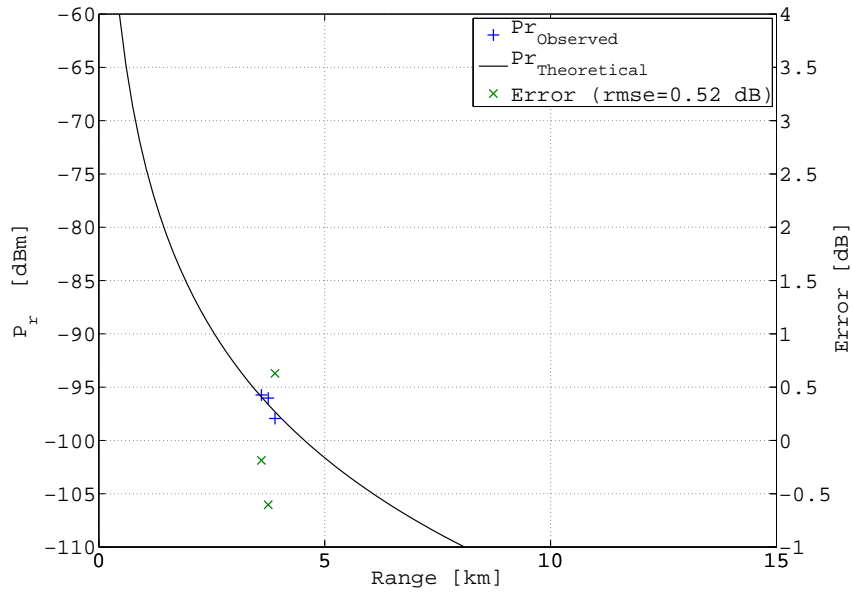


FIGURE 4.20. Ka-band sphere calibration from June 14th, 2013 starting at 00:00UTC. The graph shows measured sphere reflectivity and the theoretical reflectivity curve of a metal sphere of the same diameter. No corrections were made to this data based on calibration results.

it can be seen that the product of the receiver gain G_r and transmit power P_t are in the numerator of the radar constant equation. Therefore, the measured transmit power, via the calibration loop, appropriately accounts for variation in both receiver gain and transmit power. The remaining parameters in equation 63 are: c the speed of light in a vacuum, T_0 the uncompressed pulse width, l_r the receiver finite bandwidth loss, λ the wavelength, G_0 antenna boresight gain, θ and ϕ the antenna half power full width beamwidths in their respective planes.

Any Z_{dr} bias introduced by transmit power or receiver gain drift is similarly compensated for using equation 64. The superscripts h and v represent the respective polarization channel and P_{drx} is the received power measured at the digital receiver.

$$(63) \quad C = \left(\frac{cT_0}{2} \right) \left(\frac{G_r}{l_r} \right) \left(\frac{\lambda^2 P_t G_0^2}{(4\pi)^3} \right) \left(\frac{\pi\theta\phi}{8 \ln 2} \right)$$

$$(64) \quad Z_{dr} = 10 \log_{10} \left(\frac{P_{drx}^h}{P_{drx}^v} \right) - 10 \log_{10} \left(\frac{G_r^h P_t^h}{G_r^v P_t^v} \right)$$

An RF noise source is implemented to provide a stable reference for monitoring the receiver gain drift independent of the transmit power measurements. This provides an independent source for validating system health as extreme component parameter drift can be a precursor to component failure.

4.4.4. Calibration of Polarimetric Variables

The three frequency diverse sub-pulses used by the D3R have different starting system differential phases. With careful calibration, discontinuities in ϕ_{dp} can be removed when changing from one pulse to the next with range. Alignment of the pulse is accomplished by comparing ϕ_{dp} estimates of two pulses for the same range gate in light to moderate rain. The difference between the estimates can be applied as an offset to one of the pulses and continuity of ϕ_{dp} is ensured. The starting ϕ_{dp} at range 0 can similarly be centered to avoid phase wrapping by applying a fixed offset to all pulses after alignment has been completed.

Z_{dr} is sensitive to system parameter variation between the H and V polarization channels. Absolute Z_{dr} calibration is carried out by performing “bird-bath” scans where the antenna is pointed vertically and rotated in integer multiples of 360° during light precipitation [Bringi and Chandrasekar \(2001\)](#). For an unbiased system Z_{dr} , the mean Z_{dr} over the scan should be 0 dB. This method of Z_{dr} calibration is routinely used with example results from May 4th, 2013 presented in [Figure 4.21](#) for Ku and [Figure 4.22](#) for Ka using the short pulse. A height of 1.8km is selected for analysis with the mean copolar correlation for the scan at 0.994 for Ku and 0.993 for Ka. For

Ku, the mean Z_{dr} for the scan is 0.3459 dB with a standard deviation of 0.1784 dB. Similarly for Ka, the mean of the Z_{dr} observations is 0.3439 dB with a standard deviation 0.0755 dB. The mean Z_{dr} values determined from the bird-bath scan are then subtracted from future calculation of Z_{dr} to remove any system bias. The Z_{dr} bias for the medium and long pulses are determined in the same way continuity of ϕ_{dp} is maintained. The Z_{dr} bias from the short pulse is used as a reference to correct the medium and long pulse biases at overlapping range gates with light to moderate rain.

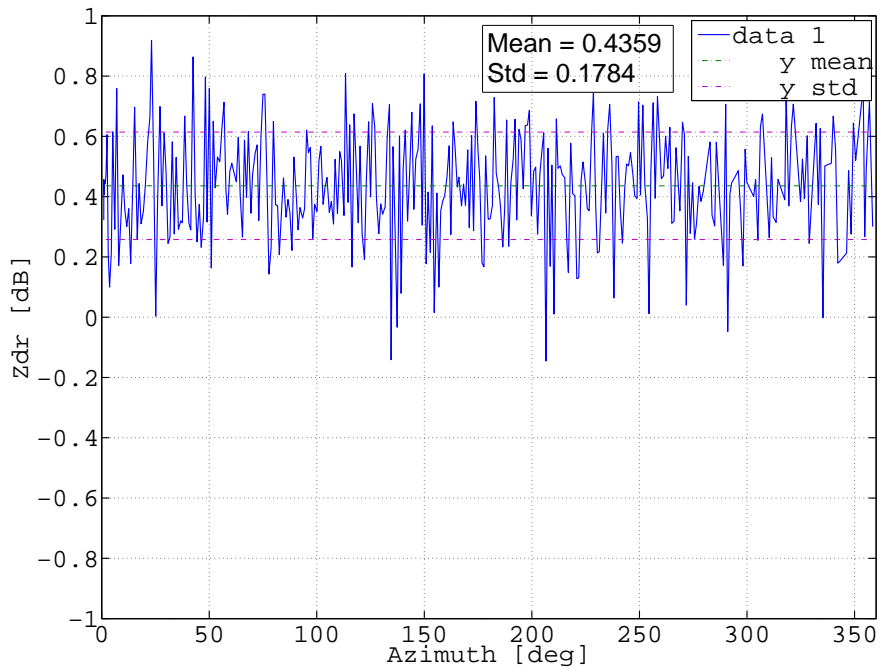


FIGURE 4.21. Ku-band short-pulse observed Z_{dr} vs. azimuth angle on 2013-05-04 at 07:09 UTC during a vertically pointing scan. Z_{dr} observations are from a height of 1.8 km above the radar. The mean $|\rho_{hv}|$ of observation is 0.994. The Z_{dr} mean is 0.4359 dB and standard deviation is 0.1784 dB.

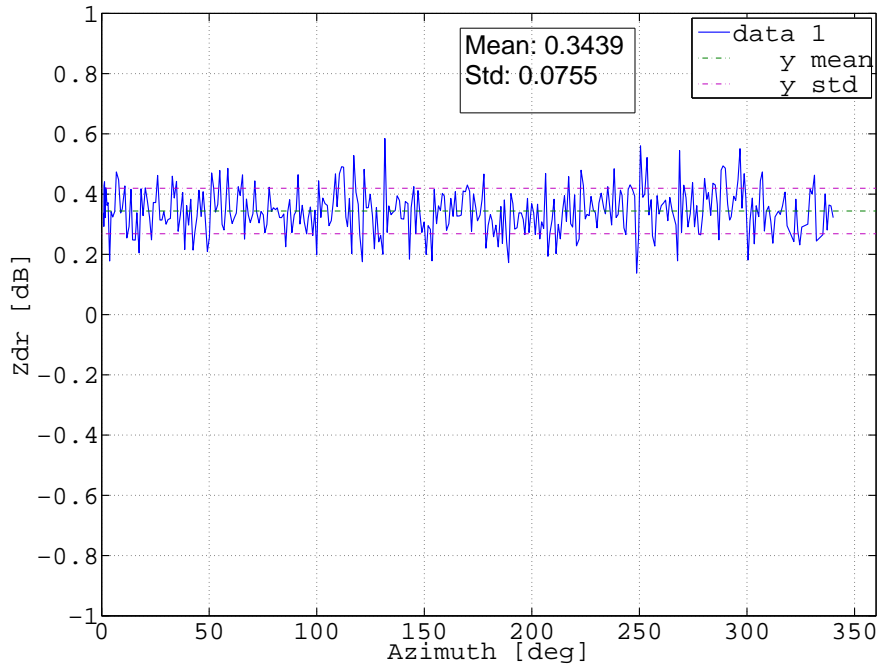


FIGURE 4.22. Ka-band short-pulse observed Z_{dr} vs. azimuth angle on 2013-05-04 at 07:09 UTC during a vertically pointing scan. Z_{dr} observations are from a height of 1.8 km above the radar. The mean $|\rho_{hv}|$ of observation is 0.993. The Z_{dr} mean is 0.3439 dB and standard deviation is 0.0755 dB.

4.5. SAMPLE OBSERVATIONS

The D3R participated in the NASA Iowa Flood Studies (IFloodS) ground validation field campaign between May 1st, 2013 and June 15th, 2013. The field campaign was the first in which the higher power Ka transmitter was deployed in the field. For the sample observations discussed here, the following radar parameters are considered: H-Pol reflectivity (Z_h), differential reflectivity (Z_{dr}), velocity v , spectrum width w , differential phase (ϕ_{dp}), and magnitude of the copolar correlation ($|\rho_{hv}|$). The data presented here is without attenuation correction.

Figure 4.23 shows Ku- and Ka-band range-height indicator (RHI) observations of stratiform rain on May 8th, 2013 at 21:53 UTC. The figure shows eight panel displays of reflectivity, velocity, differential reflectivity, and copolar correlation respectively. A cursory examination of Figure 4.23 shows that Ka-band returned power falls below the system's noise level after a range of 20 km due

to attenuation of the signal from propagation in rain. Additionally $|\rho_{hv}|$, as a function of range, shows a progressive drop off of $|\rho_{hv}|$ below 0.99 as range increases which is indicative of falling signal-to-noise ratio. The purpose of this chapter is to show the direct measurements from the radar. Several techniques are available to correct for attenuation as long as the signal is available [Bringi and Chandrasekar \(2001\)](#). A detailed examination of attenuation correction is beyond the scope of this work. Both the Ku and Ka observations distinctly show the melting layer or “bright band”. This is easily identified by the increase in reflectivity and decrease in copolar correlation at approximately 2.5 km height. The Ka-band unambiguous velocity range is exceeded and velocity folding can be observed.

Figure 4.24 shows Ku- and Ka-band plan position indication (PPI) observation of a line of convection on May 19th, 2013 at 09:18 UTC. The eight panel display includes reflectivity, differential reflectivity, differential propagation phase, and copolar correlation coefficient side-by-side for Ku and Ka-band observations. For both Ku and Ka, the effects of attenuation and differential attenuation is also noticed for ranges beyond points of high reflectivity. The areas of high attenuation correlate to large increases in ϕ_{dp} [Bringi and Chandrasekar \(2001\)](#). The range extent over which the signal exists is shorter for Ka-band compared to Ku-band. This is well known and anticipated. The Ka-band observation for GPM is designed for light rain and snow. Under those operating conditions, the Ka-band observations are available over the full operational range of the D3R [Chandrasekar et al. \(2012\)](#).

Figure 4.24 shows Ku- and Ka-band plan position indication (PPI) observation of a line of convection on May 19th, 2013 at 09:18 UTC. The eight panel display includes reflectivity, differential reflectivity, differential propagation phase, and copolar correlation coefficient side-by-side for Ku and Ka-band observations. For both Ku and Ka, the effects of attenuation and differential attenuation are also noticed for ranges beyond points of high reflectivity. The areas of high

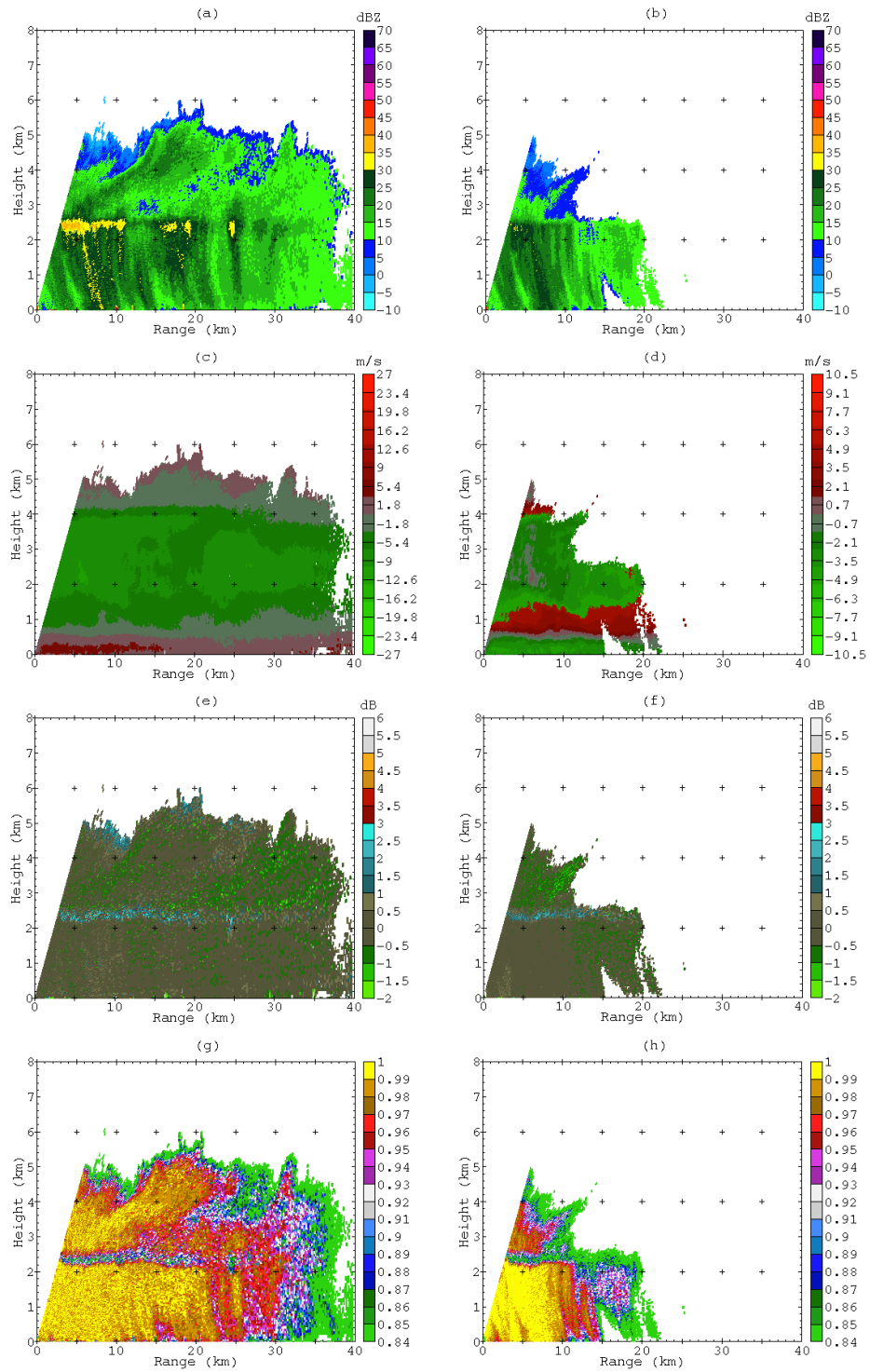


FIGURE 4.23. Ku- and Ka-band observations collected on May 8th, 2013 at 21:53 UTC. Panels are arranged with Ku-band products on the left and Ka-band on the right. Panels (a) and (b) show measured reflectivity's, (c) and (d) show mean Doppler velocities, (e) and (f) show differential reflectivities, finally, (g) and (h) show the magnitude of the co-polar correlation coefficient.

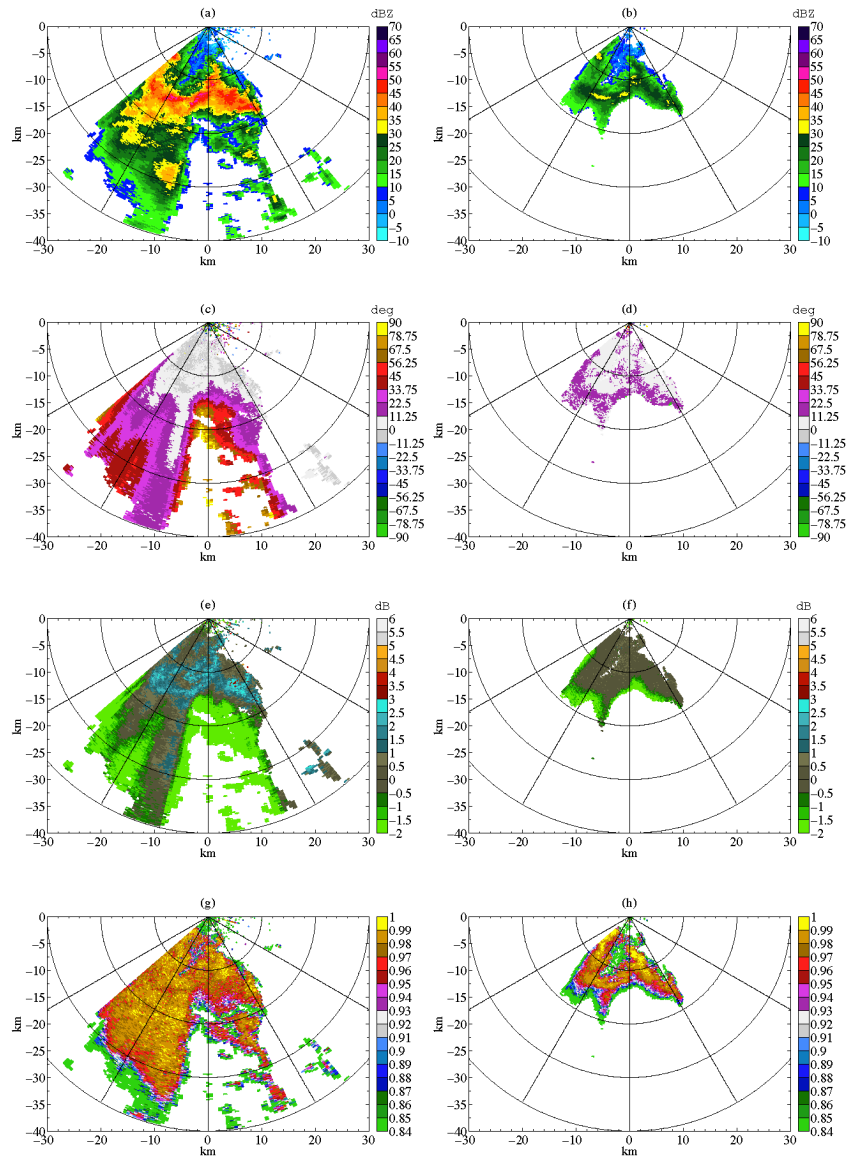


FIGURE 4.24. Ku- and Ka-band PPI observations collected on May 19th, 2013 at 09:18 UTC of a line of convection. Panels are arranged with Ku-band products on the left and Ka-band on the right. Panels (a) and (b) show measured reflectivities, (c) and (d) show differential phase, (e) and (f) show differential reflectivities, finally, (g) and (h) show the magnitude of the co-polar correlation coefficient.

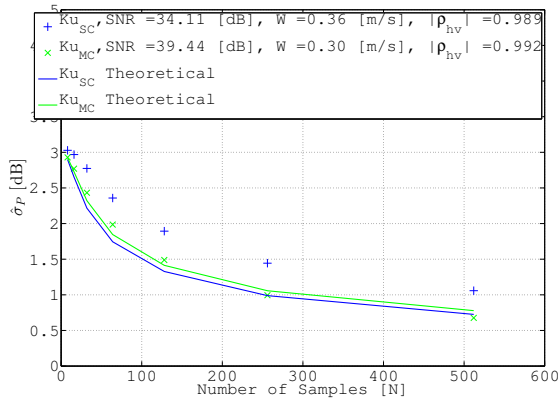
attenuation correlate to large increases in ϕ_{dp} Bringi and Chandrasekar (2001). The range extent over which the signal exists is shorter for Ka-band compared to Ku-band. This is well known and anticipated. The Ka-band observation for GPM is designed for light rain and snow. Under those

operating conditions, the Ka-band observations are available over the full operational range of the D3R Chandrasekar et al. (2012).

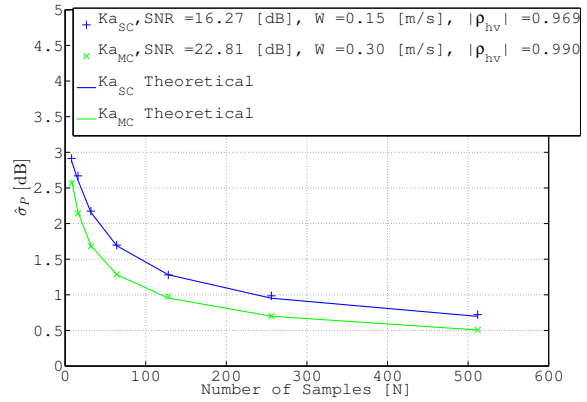
The quality of products retrieved from radar measurements (e.g. raindrop size distribution, rain rates, liquid water content, etc.) is impacted by uncertainties inherent in the measurements Bringi and Chandrasekar (2001). The following section provides quantitative validation of accuracy of Z_h and polarimetric products, namely Z_{dr} , ϕ_{dp} , and $|\rho_{hv}|$. The analysis presented aims to quantify uncertainties associated with the D3R measurements. The analysis consisted of fixed pointing time-series data collection for a light-moderate precipitation event. Simultaneous-transmit, simultaneous-receive mode with a staggered PRT of $400 \mu s/600 \mu s$ was used during the collection. The data set was then processed with a varying number of samples (8 through 512 in powers of 2). Uncertainties were estimated by computing the sample standard deviation across rays (at fixed gates with ranges at 2.4 and 3.6 km). Figures 4.25 through 4.28 show the results obtained plotted against the number of samples used. In the case of Z_h , Z_{dr} , and ϕ_{dp} , theoretical values obtained from expressions provided in Bringi and Chandrasekar (2001) were also included for reference. Estimates of $|\rho_{hv}|$ and spectrum width using the highest number of samples (512) were used as fixed parameters in the theoretical expressions. Dual-polarization moments are shown as these are sensitive to the performance of both H and V polarization channels. The results indicate D3R's accuracy of the polarimetric measurements is consistent with theoretical projections. Finally, figures 4.29 highlight typical values of $|\rho_{hv}|$ measured with the system.

4.6. SUMMARY

The dual-frequency, dual-polarization, Doppler radar is a key instrument in the GPM ground validation program. The D3R is the analogous dual-frequency ground radar counterpart to the DPR radar on the GPM core satellite. However, in addition to being a dual-frequency radar, the

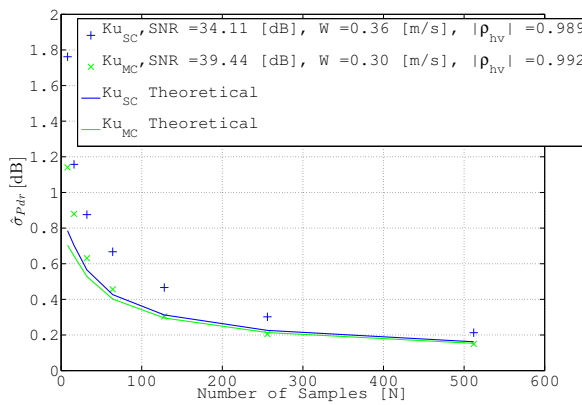


(A)

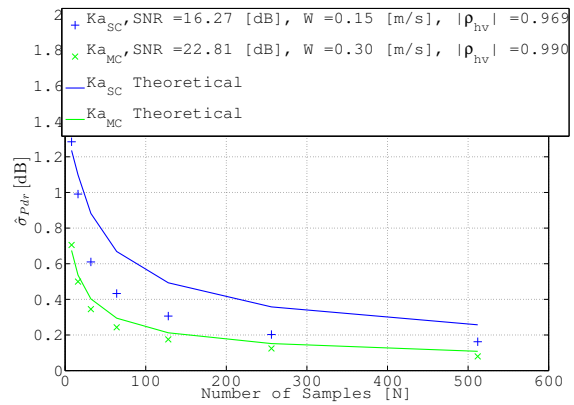


(B)

FIGURE 4.25. Ku (a) and Ka-band (b) Z_h standard deviation as a function of integration time for the short-pulse (SC) and medium-pulse (MC) channels.



(A)

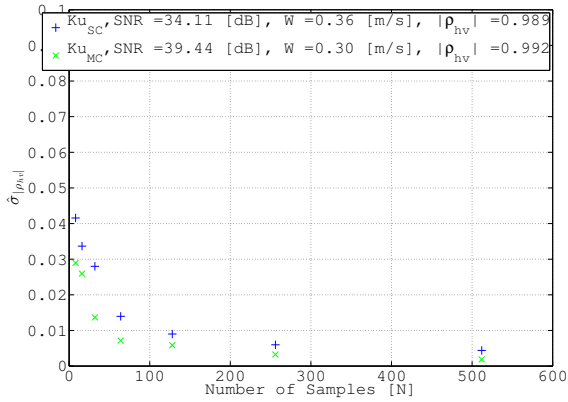


(B)

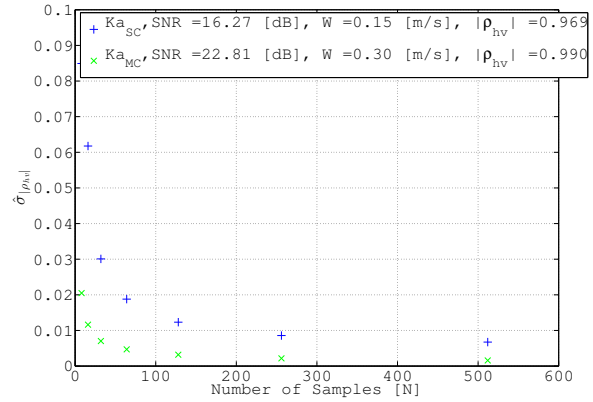
FIGURE 4.26. Ku (a) and Ka-band (b) Z_{dr} standard deviation as a function of integration time for the short-pulse (SC) and medium-pulse (MC) channels.

D3R also provides dual-polarization and Doppler capability enabling collection of self consistent dual-polarization and dual-frequency measurements to assist in the microphysical retrievals and physical validation of GPM observations.

The D3R is meant for extended deployment (on the order of few months) through the United States with potential for overseas operation. Thus the radar was designed with frequent deployment to remote location in mind. Given the diverse climates covered by GPM, the radar is expected to collect data in all forms of precipitation such as snow and rain, winter and summer, being subjected

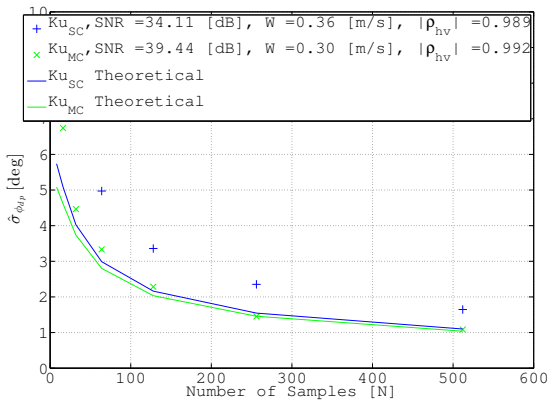


(A)

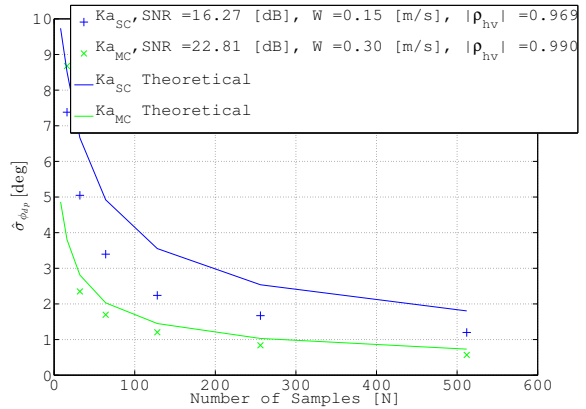


(B)

FIGURE 4.27. Ku (a) and Ka-band (b) $|\rho_{hv}|$ standard deviation as a function of integration time for the short-pulse (SC) and medium-pulse (MC) channels.



(A)



(B)

FIGURE 4.28. Ku (a) and Ka-band (b) ϕ_{dp} standard deviation as a function of integration time for the short-pulse (SC) and medium-pulse (MC) channels.

to a wide range of temperatures and environmental conditions. These scientific and operational demands resulted in a solid-state transmitter design with co-aligned antennas.

This chapter presented the system architecture and the performance of the D3R. The D3R has already been deployed to numerous locations for field observations including: Northern Colorado, Ontario, Canada, Wallops Island, Virginia, Central Iowa, Western North Carolina. Two of these deployments were in coordination with aircraft and all deployments were in coordination with

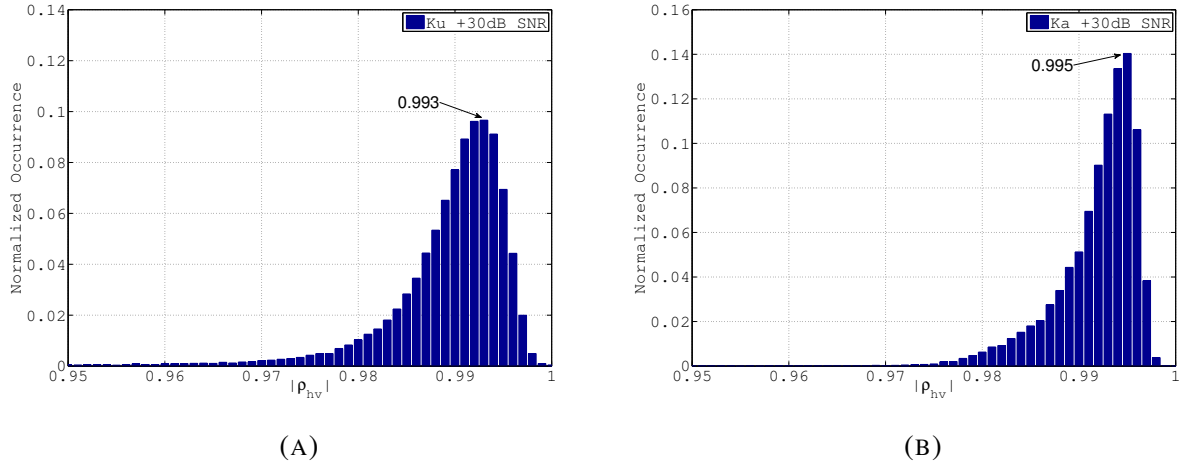


FIGURE 4.29. Ku (a) and Ka-band (b) histograms of measured $|\rho_{hv}|$.

other ground instrumentation including radar, rain gauges, and disdrometers. Overall, the D3R has performed very well yielding good scientific observations.

The D3R is calibrated using multiple techniques including absolute calibration using a metal sphere. The alignment of the antennas is checked each time after re-assembly for deployment using the solar scan technique. The antennas alignment is consistently repeatable and alignment holds within 0.1 degree accuracy.

The standard deviations on the polarimetric measurements were evaluated experimentally by collecting observations of Z_h , Z_{dr} , $|\rho_{hv}|$, and ϕ_{dp} . The standard deviations were compared against theoretical projections and these compare very well indicating good overall system integrity. The experimental copolar correlation observations in light rain was found to be above 0.99 in the RHI scans of stratiform rain, which again shows the overall system integrity. Data from the D3R have been used in detailed coordinated analysis to make quantitative comparison of Ku- and Ka-band observations by [Duffy et al. \(2013\)](#). Airborne comparison show excellent cross validation results with the D3R, demonstrating the quality and usefulness of the D3R observations.

CHAPTER 5

MULTI-FREQUENCY ACTIVE/PASSIVE INSTRUMENT CALIBRATION

5.1. RADAR CALIBRATION

5.1.1. Point target with known radar cross-section

Multi-frequency weather radar systems provide information on the media with which they interact primarily due to wavelength dependence on scattering properties of hydrometeors ¹. However, this approach requires absolute calibration at each frequency to provide meaningful results since it relies on the measurement of reflectivity factor Z . The atmospheric radar equation relates the backscatter cross-section, η , to the average received power \bar{P}_o measured at the receiver output from a volume containing a random distribution of targets as illustrated in figure 2.1 through the radar constant C in equation 65, [Bringi and Chandrasekar \(2001\)](#).

$$(65) \quad \bar{P}_o = \frac{C\eta}{r_0^2}$$

where

$$(66) \quad C = \left[\frac{cT_0}{2} \right] \left[\frac{G_r}{l_r} \right] \left[\frac{\lambda^2 P_t}{(4\pi)^3} \right] \left[\frac{G_0^2}{l_{wg}^2} \right] \left[\frac{\pi\theta\phi}{8\ln 2} \right]$$

¹The computation of scattering properties of spherical and non-spherical water particles is outside of the scope of this work, but the reader is encouraged to see chapter 2 of [Bringi and Chandrasekar \(2001\)](#).

Note that the ratio of receiver gain over finite bandwidth loss $G_r l_r^{-1}$ was included in this definition as measurements are referenced to the antenna port or reference plane by convention. Receiver gain is typically measured by relating the receiver power output P_o to the power of a known signal injected at the reference plane P_i . However, this method still leaves the term l_r unknown. Finite bandwidth loss can be determined through simulation of the transmit waveform and corresponding receiver filter as

$$(67) \quad l_r = \frac{cT_0/2}{\int_0^\infty |W_n(r)|^2 dr}$$

where $W_n(r)$ is the normalized range-time weighting function defined as the convolution between the transmit waveform and receiver filter [Bringi and Chandrasekar \(2001\)](#). The term l_{wg} was also added to account for waveguide loss between the antenna port and the transmitter/receiver reference plane. It essentially reduces the antenna gain and can be combined with the antenna gain since it is also a two-way term.

Generally speaking, radar calibration consists of collecting observations of a target with a known cross-section and correcting the measured received power P_r using the value expected from the known target. In reality, the exercise is compounded by practical issues such as imperfect targets, clutter contamination, range to target and location with respect to the antenna weighting function, range-time sampling period, infrastructure required among others. Following this approach, metal sphere and trihedral corner reflectors are typical targets used. In both cases, the known cross-section, determined from target physical dimensions, comes from a point target rather than distributed (i.e. from a volume or surface). The radar equation for a point target within the peak of the antenna gain and range-weighting functions is

$$(68) \quad P_r = \frac{\lambda^2 P_t G_0^2 \sigma_t}{(4\pi)^3 l_{wg}^2 r_t^4}$$

where σ_t is the target cross-section and r_t is the range to the target. Note that for a point target, the received power P_r drops with the fourth power of range and in the case of multi-frequency radars, the shorter wavelengths will see a reduction in P_r with λ^2 . This becomes important since a target that is detectable at long wavelengths may not be a shorter or at least the signal-to-noise ratio will suffer and so will the precision of the power estimates. Also note that P_r is implicitly defined at the reference plane and therefore receiver gain is already accounted for, but l_r still needs to be determined as well as the antenna pattern correction. On the antenna pattern correction, the Probert-Jones correction is typically used, however if antenna patterns are available, these can be used to compute the antenna pattern correction or judge how well the Probert-Jones term approximates the antennas employed in the instrument.

An example on the application of a metal sphere tethered to a helium filled balloon to calibrate the D3R system was provided in chapter 4 section 4.4. Figures 4.19 and 4.20. Note how the number of samples is somewhat limited by the system's sensitivity, specially on the Ka-band. The following section, will focus on using a trihedral corner reflector mounted on a tower as the calibration target using the D3R system.

5.1.2. Tower calibration

In the case of a trihedral corner reflector, the radar cross-section in m^2 , σ_t can be estimated based on the inside edge dimension L as (Bharadwaj et al. (2011))

$$(69) \quad \sigma_t = \frac{4\pi L^4}{3\lambda^2}$$

For the D3R calibration exercise, the target used had an inside edge dimension of 6.4 inches as illustrated in figure 5.1. To assess the spatial function of the target’s cross section and correctness of equation 69, simulations in HFSS at the D3R were performed Marrero (2015a). Figure 5.2 shows simulation results. The boresight cross section from equation 69 was found to be within 0.2 dB at Ku and 0.6 dB at Ka-band when compared to the simulation. However, spatially, the patterns show a significant dependence with θ which warrants careful alignment to ensure the peak cross-section is sampled during calibration. Note that the target exhibits a very good cross-pol response (> 30 dB isolation) when properly aligned.

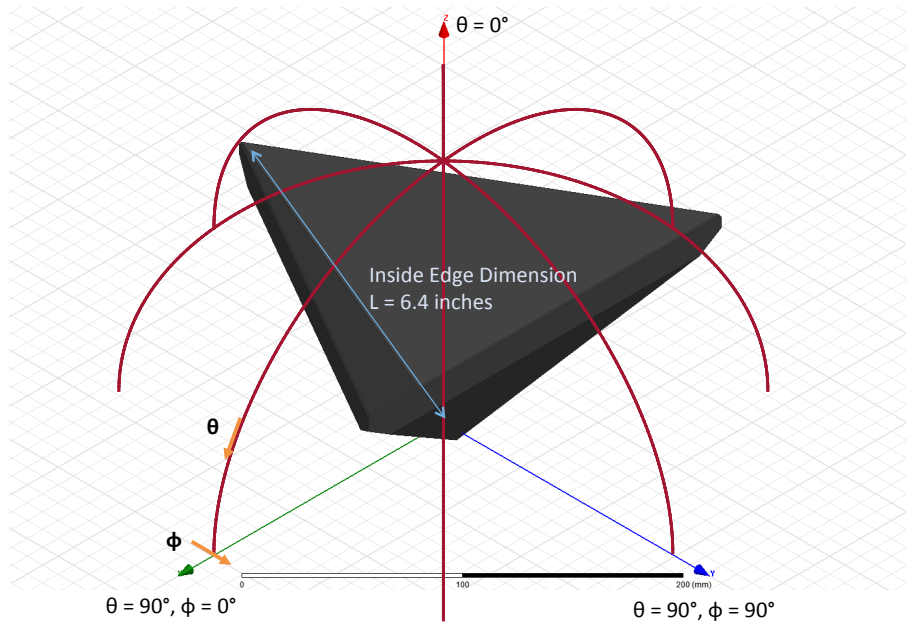
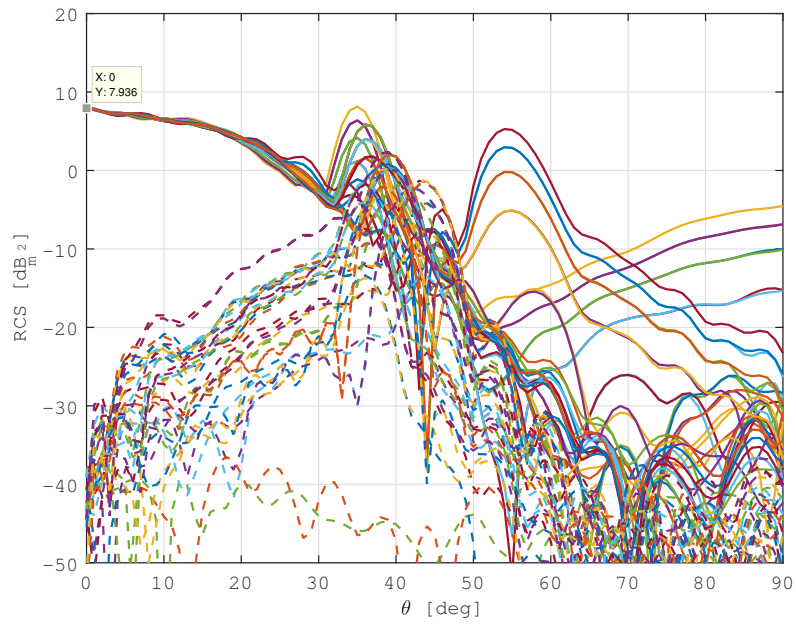
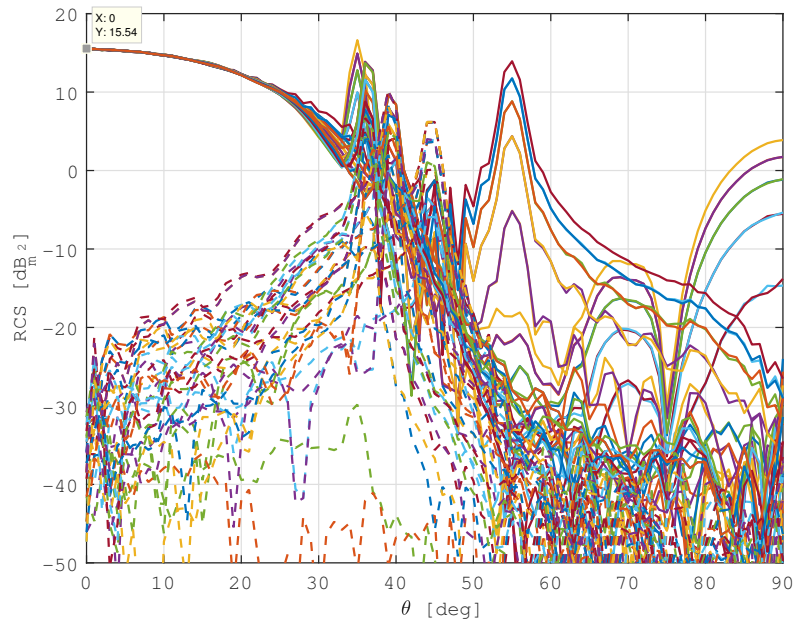


FIGURE 5.1. Trihedral corner reflector model showing inside edge dimension, simulation coordinate system and spatial pattern cuts computed from Marrero (2015a).



(A)



(B)

FIGURE 5.2. Ku (A) and Ka (B) 6.4 inch trihedral corner reflector HFSS simulation results ($\phi = (0, 350)$ in 10 deg increments) for co (solid lines) and cross-polarized (dashed lines) cross sections from Marrero (2015a).

On the other hand, the corner reflector exhibits an inverse λ^2 dependence that when substituted into equation 68 cancels out the wavelength dependence on P_r . In the case of multi-frequency radars, where we are interested in measuring dual-frequency ratios (DFR) as $Z_{Ku} - Z_{Ka}$, one may pose the calibration of DFRm as the measurement of the ratio of received powers at both frequencies P_{rKu}/P_{rKa} . In the case of a corner reflector target, the difference is purely due to different antenna and receiver gains, transmitted power and waveform characteristics such as the finite bandwidth loss l_r . In the case of the D3R system, waveforms and corresponding filters are matched so l_r should have no effect and side-lobe clutter contributions together with system drift are possibly the largest sources of error.

Figures 5.3 and 5.4 show general layout of the experimental setup at Wallops Flight Facility Virginia (WFF) and calibration tower highlights respectively. The radar system was located approximately 480 meters from the tower and the tower height is approximately 30 meters. The height sets the elevation angle of the antennas to approximately 3 degrees and applies to both Ku and Ka-band since both are co-aligned to within a tenth of a degree. At 480 meters, with a 6.4 inch corner reflector, the backscattered power is expected to be 6 and 14 dB below the Ku and Ka-band receiver 1 dB saturation points so no linearity issues were expected. Regarding target pointing, the tower is equipped with an azimuth rotator. In preparation for the exercise, the radar is pointed towards the tower and the target's azimuth is adjusted until the maximum return power is achieved.

The antenna beams are expected to spread to approximately 7.5 meters at 480 meters which makes the carbon mast slightly on the short side. Ideally it would be desired for the mast to cover the entire half section of the main beam down to the first null to minimize its contribution to the return signal. Figure 5.5 shows the upper and lower error bounds arising from the coherent addition of two signals. This is the case for the tower calibration approach where the radar is not only receiving a signal from the calibration target, but all surroundings weighted by the antenna



FIGURE 5.3. Radar calibration setup at Wallops Flight Facility. D3R system indicated by yellow pin on top and calibration tower located at bottom yellow pin.

pattern. From this figure, we could get an idea of what level of accuracy we can expect from this calibration approach. To achieve a calibration accuracy within 0.5 dB, the target signal-to-clutter ratio needs to be at least 25 dB. Scans with and without the calibration mounted to the tower were performed to assess the level of signal-to-clutter ratio and was found to be approximately 25 dB for both Ku and Ka-band systems. So calibration accuracy within ± 0.5 dB is not unreasonable to expect.

Figure 5.6 shows the maximum equivalent reflectivities observed from the tower calibration experiment. The observations shown span about two hours worth of continuous PPI scans configured to ± 5 deg in azimuth at 2 deg/s and ± 0.5 deg in elevation with 0.1 deg elevation steps centered at the expected target angular location. The scan rate of 2 deg/sec and dwell time of 64 ms yields an azimuth resolution of approximately 0.13 degrees and ensures the target's cross section weighted

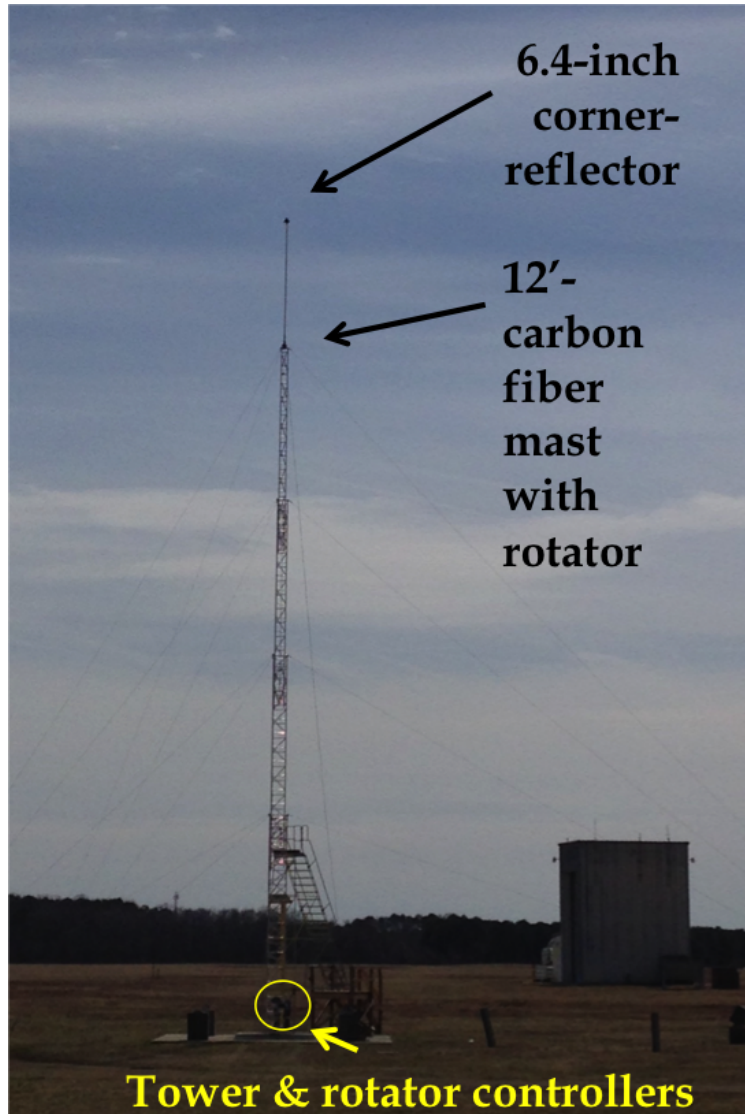


FIGURE 5.4. Radar calibration tower at Wallops Flight Facility. Target height is approximately 30 meters.

by the antenna pattern function is oversampled. Note that returns over the period of two hours remained quite stable although the calibration loop was not enabled during the exercise.

The expected equivalent reflectivity values derived from the laboratory measured system parameters were 59.55 and 53.43 dBZ for Ku and Ka respectively. These values minus to the mean of the observations represented an offset of -1.91 and 2.12 dB for the Ku and Ka respectively. To test out the new calibration offsets, the new calibration was applied retrospectively to a prior snow event in February 26th of 2016.

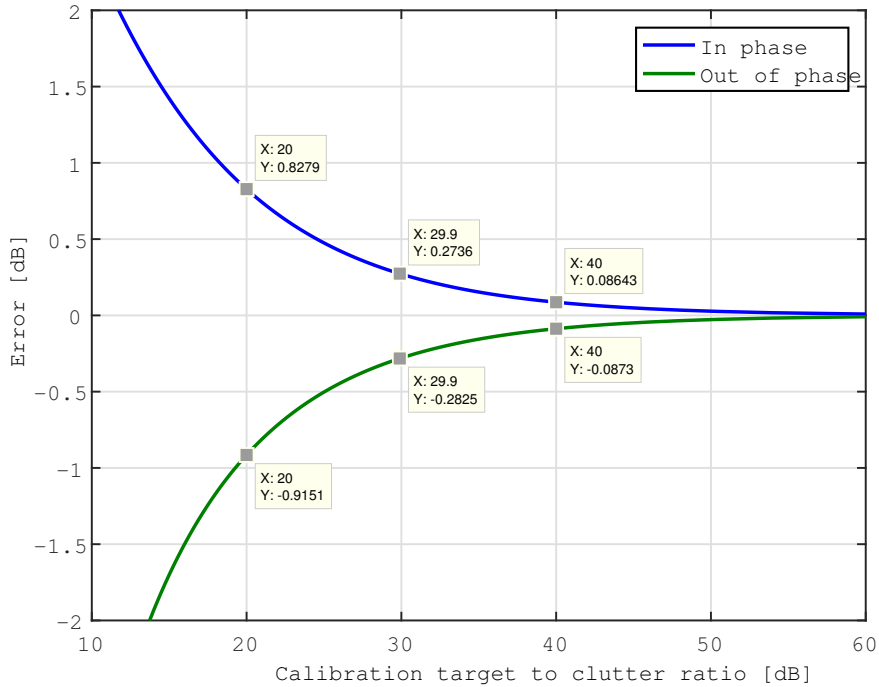
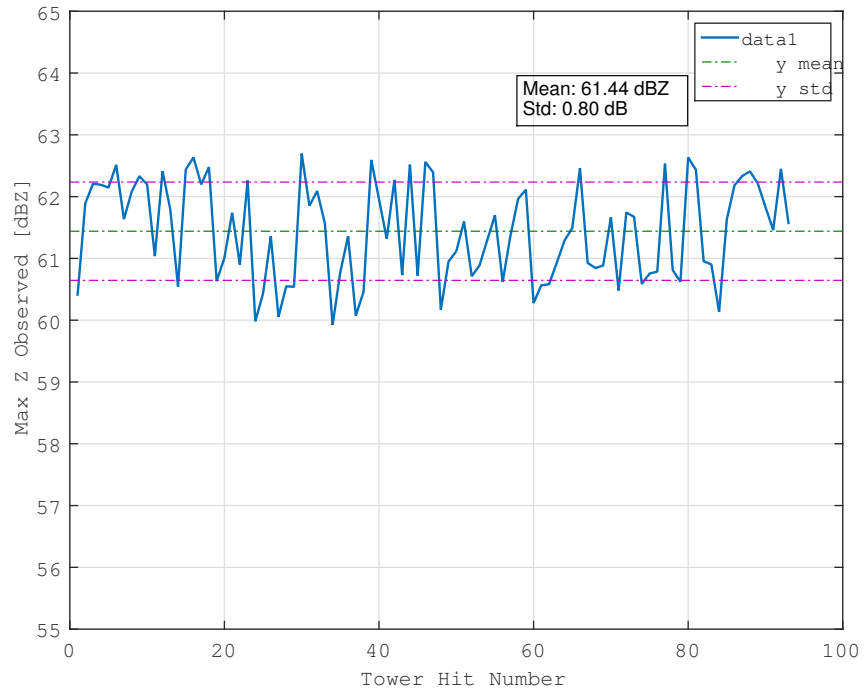


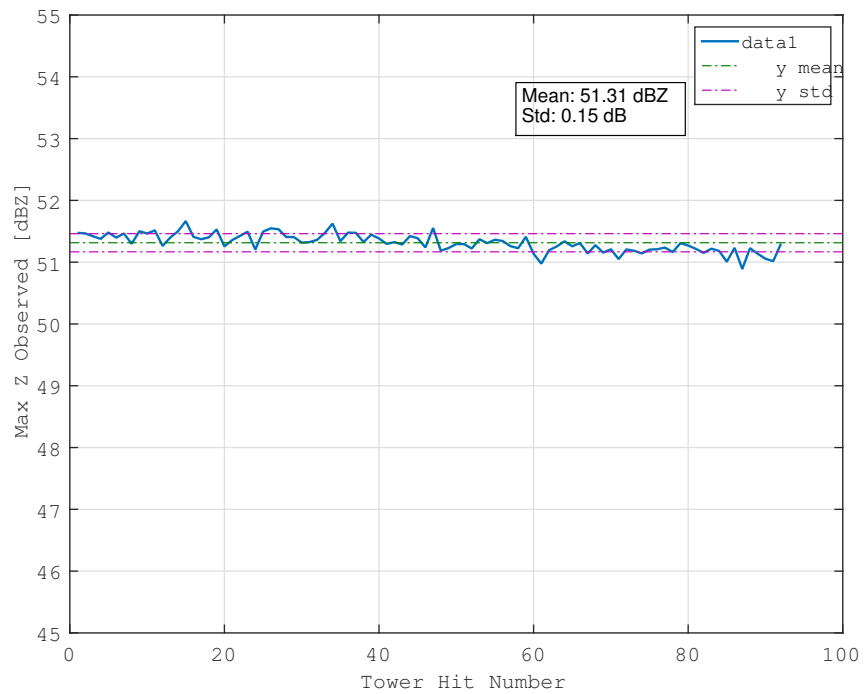
FIGURE 5.5. Calibration error bounds vs signal to clutter ratio. Equivalent result to that shown in Bharadwaj et al. (2011)

Figure 5.7 shows the Z_{Ku} versus DFRm near the beginning of a snow event at WFF. The mean DFRm for the observations was found to be -0.44 dB for $Z_{Ku} = 0$ dBZ. This result is consistent with Tyynelä and Chandrasekar (2014), Kneifel et al. (2015) and Liao et al. (2016) and support a successful absolute calibration of both reflectivity factors. Figure 5.8 shows Z_{Ku} and DRFm plots for the RHIs used to generate the scatter plot.

Finally, it is worth showing the other fields such as Doppler spectra and velocity, co-polar correlation coefficient, differential phase and Z_{dr} values from observations of the corner reflector. No attempt on using these for system characterization were performed as part of this work. However, since the target practically serves as mirror for the radar to look at itself, extraction or characterization of the system differential phase offset, Doppler velocity bias, co-polar correlation limit and Z_{dr} stability may be the theme of future research. Figures 5.9, 5.10, 5.11, 5.12 and 5.13 show these fields obtained from the same exercise dataset.



(A)



(B)

FIGURE 5.6. Ku (A) and Ka (B) maximum reflectivity observations from calibration exercise at WFF April, 2015.

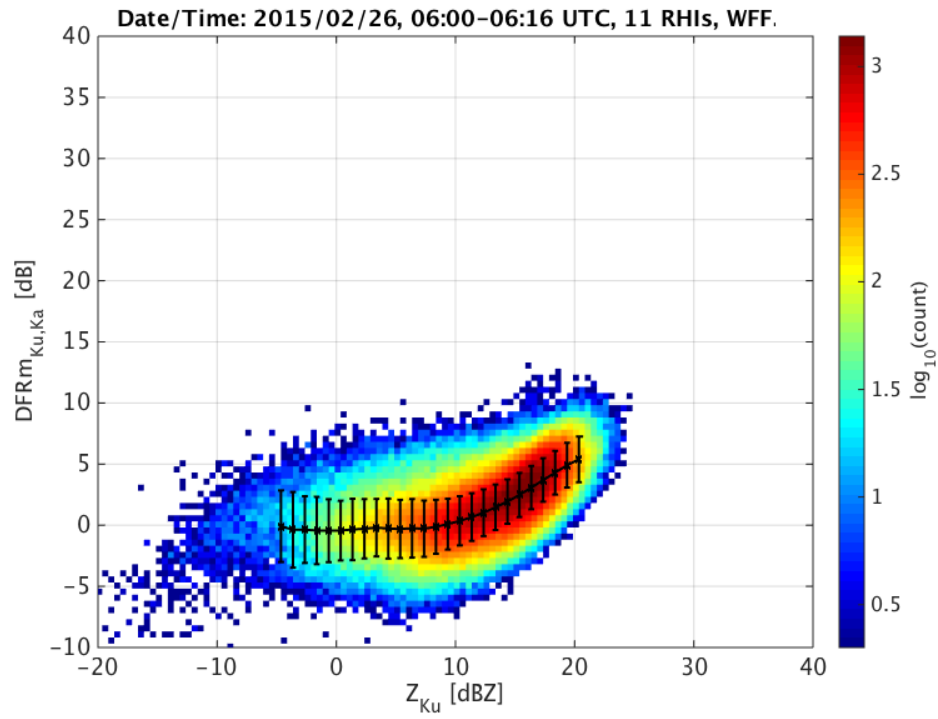


FIGURE 5.7. DFRm vs Z_{Ku} histogram for beginning of snow event in February 26th, 2015 using RHI observations from 06:00 to 06:16 UTC.

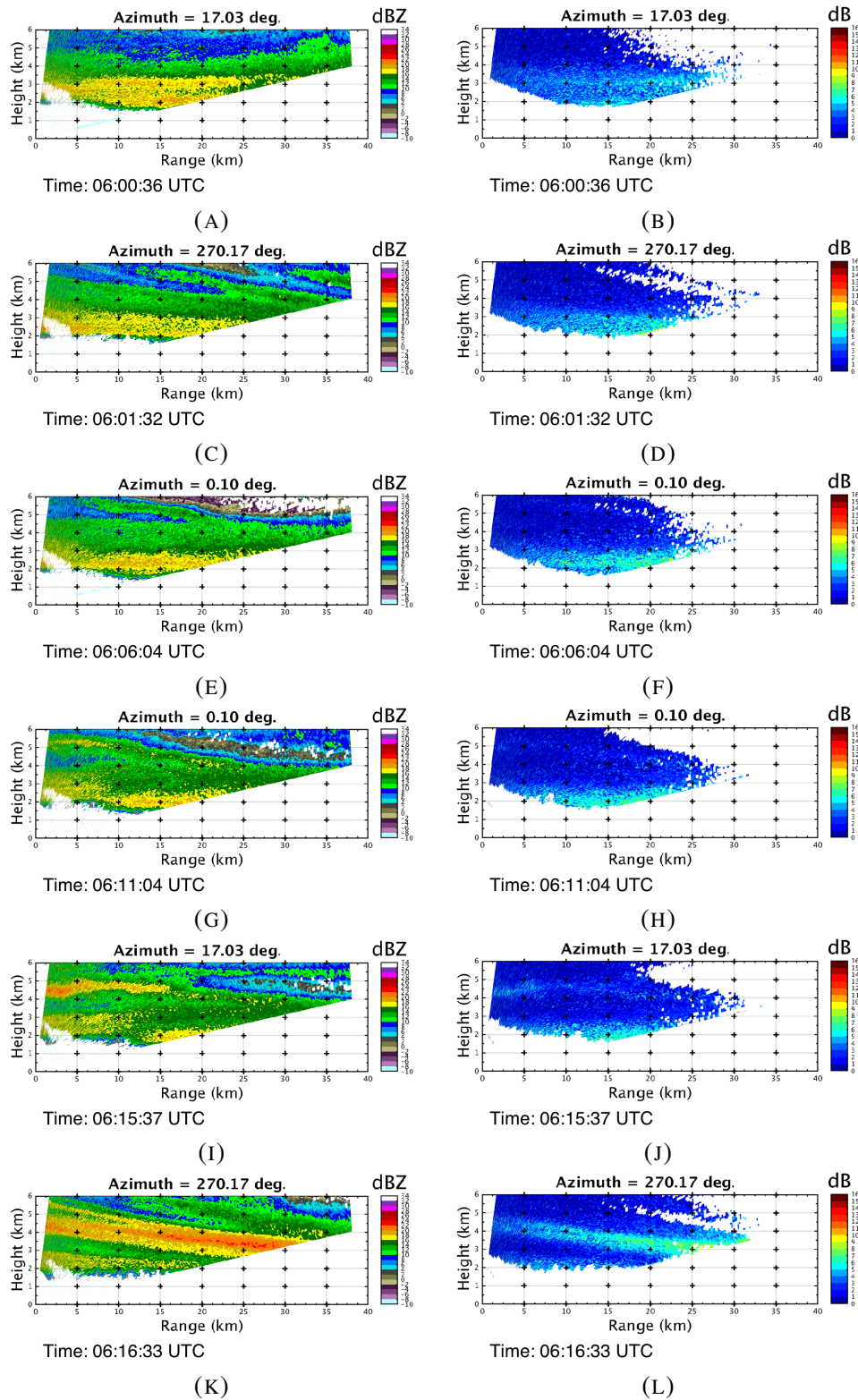
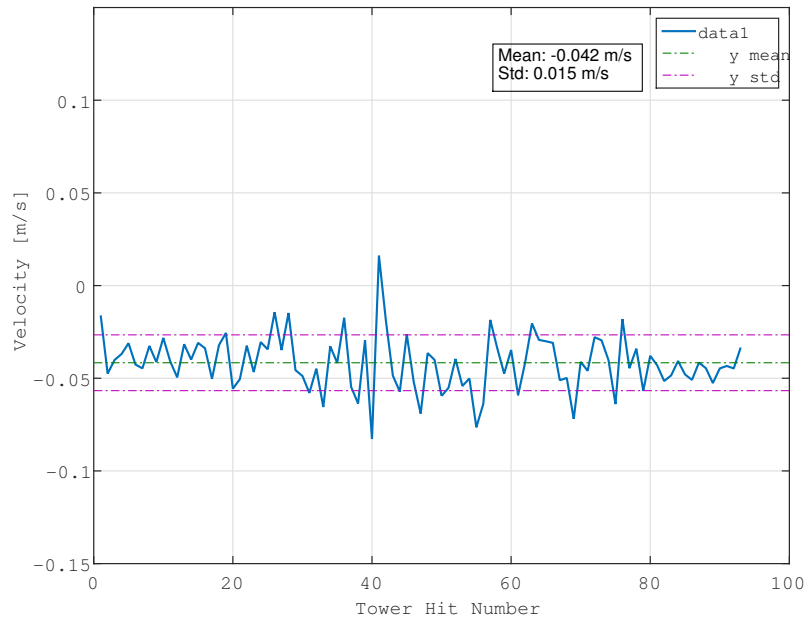
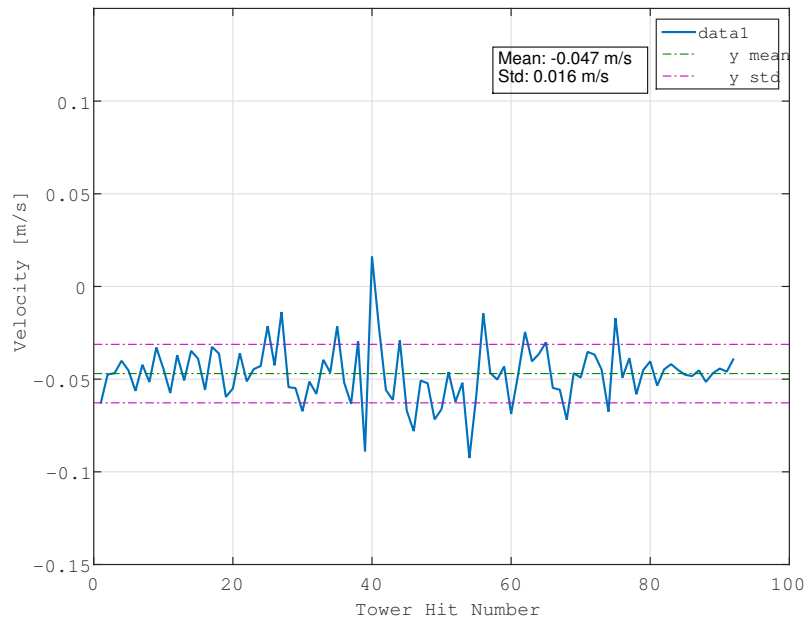


FIGURE 5.8. Sample of Ku reflectivity (left) and Ku/Ka measured dual-frequency ratio (DFR_m) (right) RHIs for snow event in February 26th, 2015. Used to generate histogram.

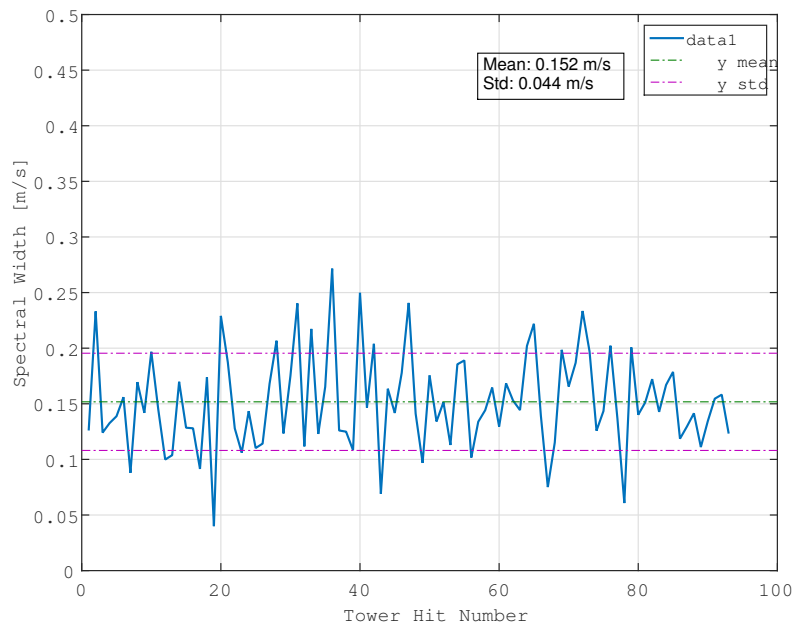


(A)

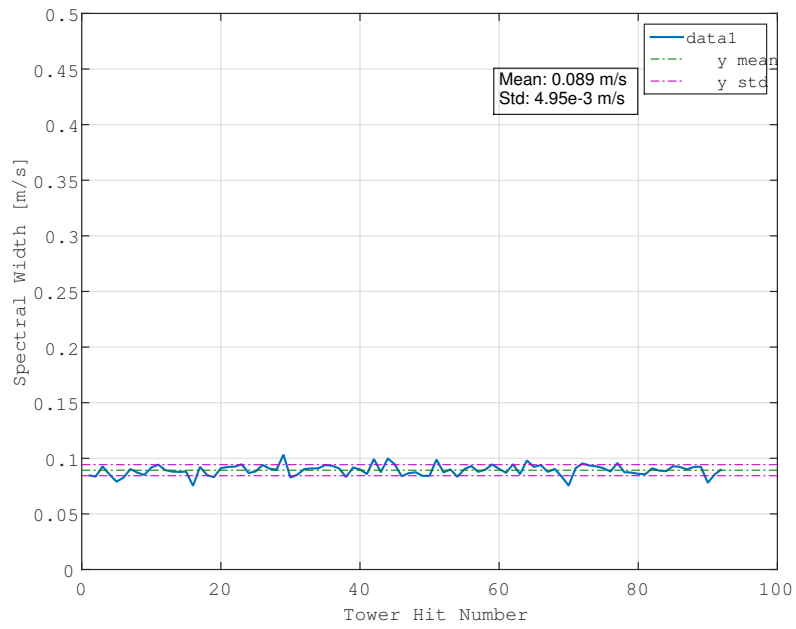


(B)

FIGURE 5.9. Ku (top) and Ka (bottom) Doppler velocity from calibration exercise. Note a slight mean negative bias $< 0.05 m.s^{-1}$ for both systems.

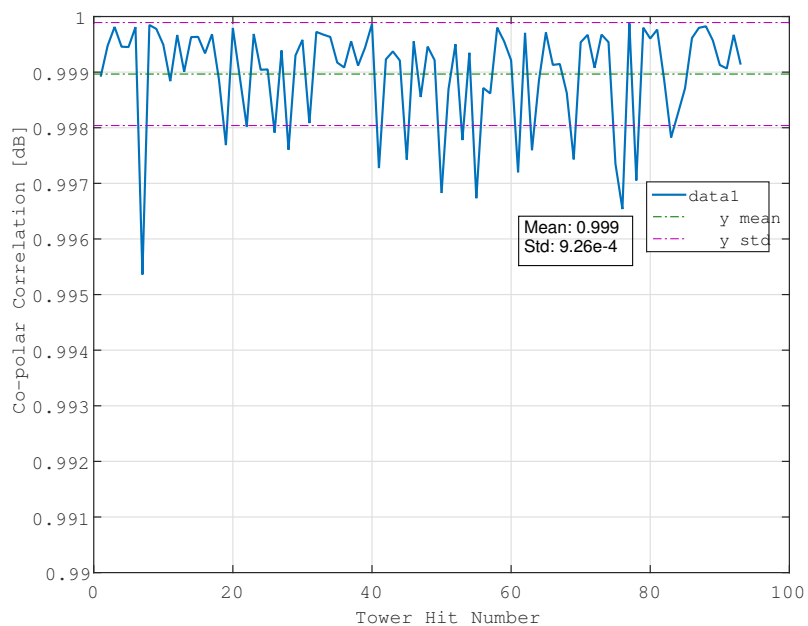


(A)

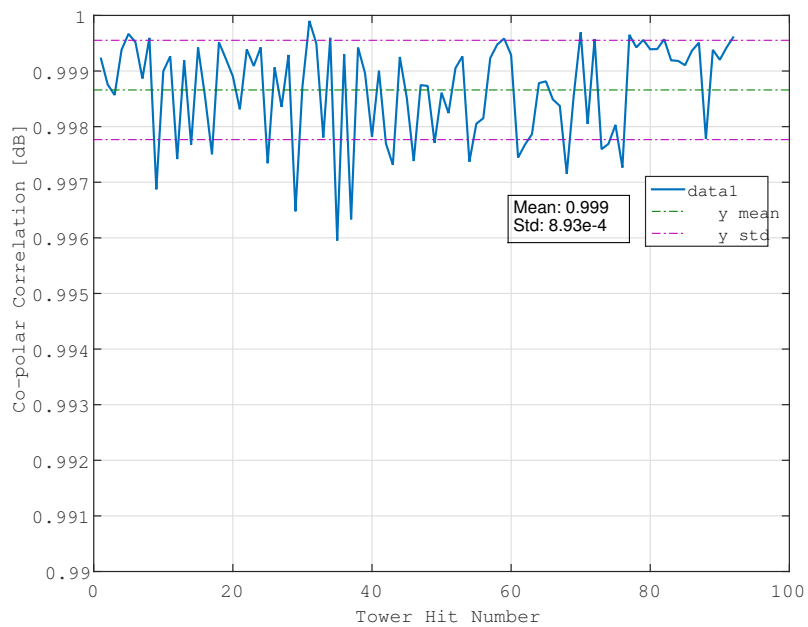


(B)

FIGURE 5.10. Ku (top) and Ka (bottom) spectral width from calibration exercise.

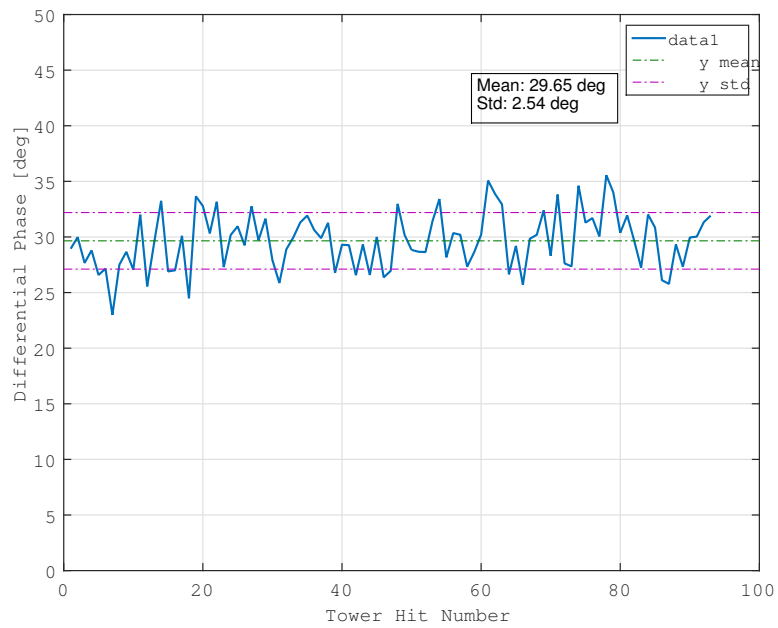


(A)

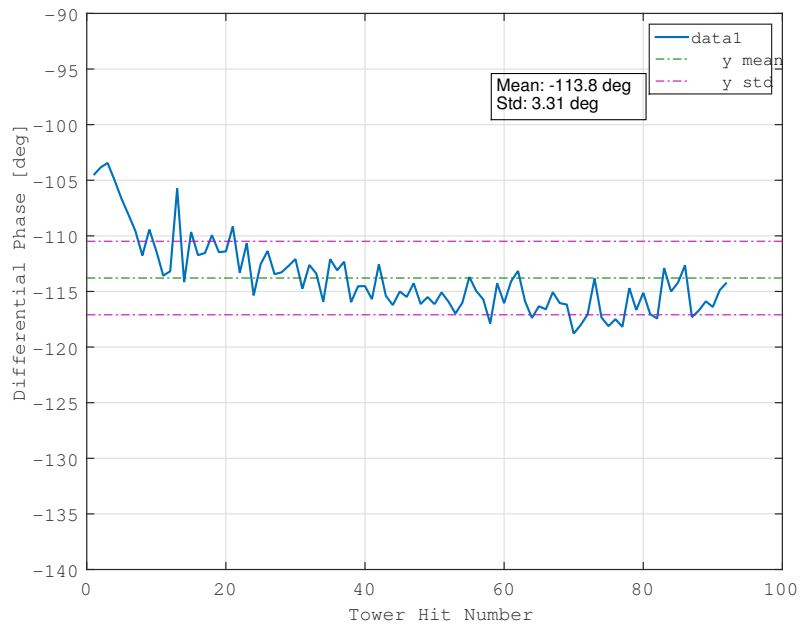


(B)

FIGURE 5.11. Ku (top) and Ka (bottom) $|\rho_{HV}|$ from calibration exercise. Both systems exhibit a mean $|\rho_{HV}| \approx 0.999$.

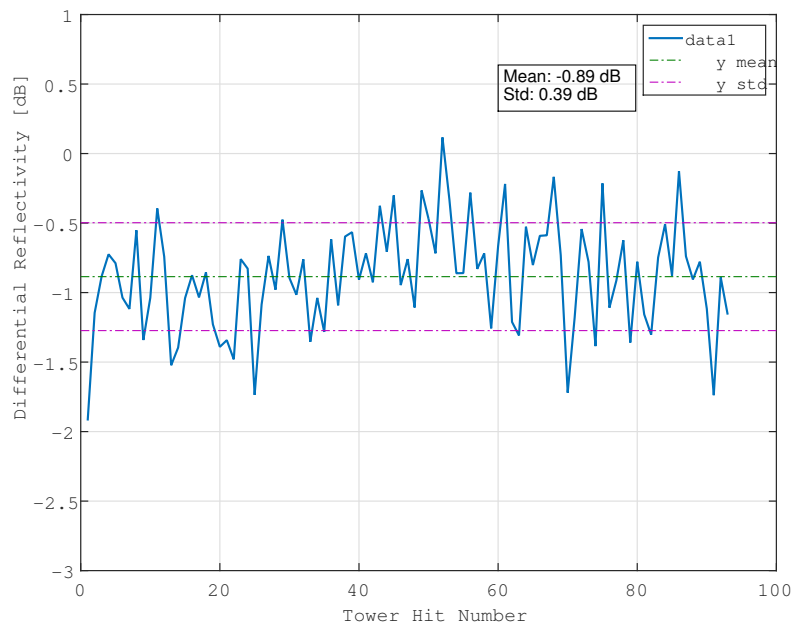


(A)

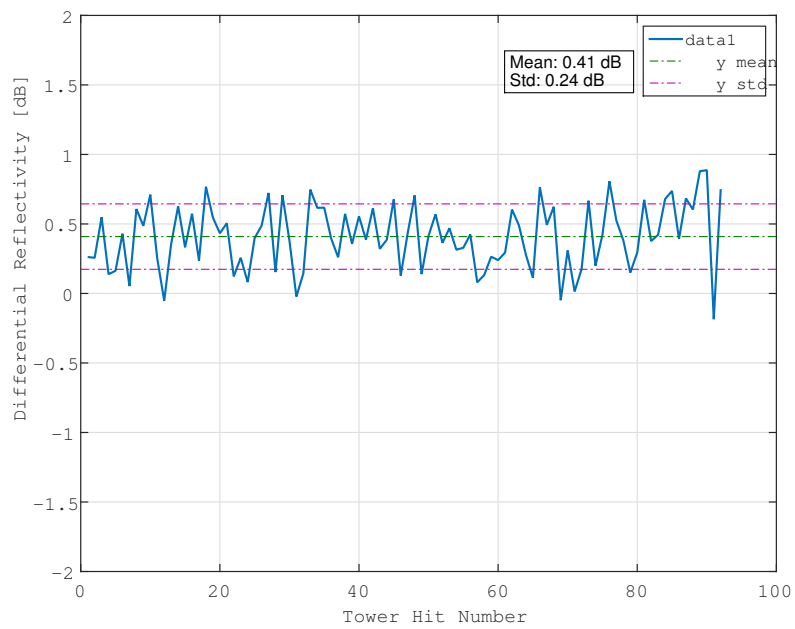


(B)

FIGURE 5.12. Ku (top) and Ka (bottom) ϕ_{dp} from calibration exercise.



(A)



(B)

FIGURE 5.13. Ku (top) and Ka (bottom) Z_{dr} from calibration exercise.

5.2. RADIOMETRIC CHANNEL CALIBRATION

5.2.1. *Tipping curve calibration*

To refresh some of the salient system features in our approach to attempting an active/passive atmospheric measurement platform, the D3R system uses a single aperture or antenna and receiver chain with sufficient bandwidth to take advantage of frequency diversity in achieving multiple sensing strategies. One of them being the monitoring of thermal emissions from atmospheric constituents in the path defined by the antenna angular pattern, pointing direction and system location. Chapter 3 introduced important aspects in the design of a radiometer system such as antenna beam efficiency, receiver architecture, radiometric resolution dependence on bandwidth, observation time and receiver temperature with discussions on how these reflect on the D3R system. In this section, the focus shifts into the calibration of the passive channels together with an observation case study using the end-to-end system calibration function determined from clear day measurements.

[Han and Westwater \(2000\)](#) describes the process of tier 3 calibration (i.e. end-to-end calibration using external reference, [Racette and Lang \(2005\)](#)) of ground-based radiometer systems along with possible sources of error and methods to identify, evaluate and/or mitigate them. In particular, the tipping calibration method couples atmospheric radiative transfer with received measurements obtained through a radiometer system. On this work, our focus is on calibrating a passive channel on the D3R system described in chapter 3.

The tipping calibration method stems from specific atmospheric conditions that can be modeled by planar strata in thermodynamic equilibrium with pure absorption and emission. In this case the solution to the differential radiative transfer equation $dI_f = -I_f\alpha ds + S ds$, where I_f is the specific radiation intensity in $Wm^{-2}Hz^{-1}Sr^{-1}$, α is an absorption coefficient and S a source term can be written as

$$(70) \quad I_f(0) = I_f(s_0)e^{-\tau(s_0)} + \int_0^{s_0} B_f(T)e^{-\tau(s)}\alpha ds$$

where s_0 represents a boundary point in space where I_f has a known value (e.g. cosmic background for up-looking radiometer), 0 is the observation origin, τ is the optical thickness or opacity defined in equation 71 and B_f is the Planck radiation function defined in section 2.5, Jansenn (1993). Note that up to this point only non-scattering media is assumed. Planar, uniform strata will follow when working with opacities at different elevation angles.

$$(71) \quad \tau(s) = \int_0^s \alpha(s') ds'$$

For frequencies below 300 GHz, the Planck radiation law can be approximated using the Rayleigh-Jeans equation (RJE from now on and repeated below for convenience, equation 72). Note that in this approximation the radiation intensity is linearly related to the physical temperature and gives rise to the definition of a brightness temperature $T_b(f) \equiv \frac{\lambda^2}{2k}I_f$, which is a scaled spectral intensity in units of degrees Kelvin.

$$(72) \quad B_f \approx \frac{2f^2kT}{c^2}$$

Using this approximation, a ratio of the RJE and Planck law function can be defined as $\mathfrak{R}(f, T) = B_{f,RJE}B_f^{-1}$ and shown in equation 73.

$$(73) \quad \mathfrak{R}(f, T) = \frac{kT}{hf} (e^{\frac{hf}{kT}} - 1)$$

which, in turn, is equivalent to TT_b^{-1} arising from scaling of the Planck equation by $\lambda^2(2k)^{-1}$ or more simply $T_b = \frac{hf}{k} (e^{\frac{hf}{kT}})^{-1}$.

In the case where $\mathfrak{R}(f, T) = 1$ (i.e. RJE equivalent to the Planck intensity which is valid for the microwave frequency range and temperatures above the cosmic background) used in equation 70, the radiative transfer equation can be written as typically seen in literature and shown in equation 74.

$$(74) \quad T_b(f) = T_{b0}(f)e^{-\tau(s_0)} + \int_0^{s_0} \frac{T(s)}{\mathfrak{R}(f, T(s))} e^{-\tau(s)} \alpha ds$$

No that we have the basic (i.e. scattering omitted) radiative transfer equation to compute the brightness temperature in units of degrees Kelvin, T_b , we can continue to develop the tipping calibration method explanation. First, let us define the term airmass, $a(\theta)$, as the ratio of opacities

$$(75) \quad a(\theta) = \frac{\tau(\theta)}{\tau(90^\circ)}$$

where $\tau(\theta)$ and $\tau(90^\circ)$ are the optical thicknesses at elevation angle θ and at zenith pointing $\theta = 90^\circ$. Note that we have written opacity as a function of elevation angle. This stems from the fact that the propagation path changes with the elevation angle. For a planar stratified (i.e. homogeneous layers) atmosphere and neglecting refraction, the airmass follows a well defined function of the elevation angle θ

$$(76) \quad a(\theta) = \frac{1}{\sin(\theta)} = \csc(\theta)$$

This relationship forms the basis of the tipping curve calibration method. Using a ground-based radiometer system, one can measure a set of brightness temperatures corresponding to different elevation angles (antenna or uncalibrated system temperatures really, T_a or T_u), map them into opacities, and derive a correction/calibration factor or function for the system under test (SUT) by extrapolating the linear relationship to zero airmass where the opacity should equal zero as well. One major highlight is that this method takes into account the full system and not just some portions of the receiving system (tier 3 as defined in [Racette and Lang \(2005\)](#)).

As mentioned previously, the tipping curve calibration method relies on knowledge of airmass function, or ratio of opacities at different zenith angles over the zenith opacity. The mapping of brightness temperatures to opacity is achieved by defining a mean radiating brightness temperature T_{mr} ([Westwater \(1993\)](#)) as

$$(77) \quad T_{mr} = \frac{\int_0^{s_0} T(s) \alpha e^{-\tau(0,s)} ds}{1 - e^{-\tau(0,s_0)}}$$

Using equation 77 for T_{mr} in the radiative transfer equation 74 yields

$$(78) \quad \tau(0, s_0) = -\ln \left(\frac{T_{mr} - T_b}{T_{mr} - T_{b0}} \right)$$

which enables a simple mapping of brightness temperature to opacity. In general, the mean radiating brightness temperature is computed from climatological time-scale datasets of radiosonde profiles for the location of interest. Han and Westwater (2000) suggests the subsetting of T_{mr} estimates from radiosondes into seasons to reduce uncertainty as well as estimation from surface temperature T_s measurements through a regression of T_{mr} estimates. The authors also caution on the use of T_s during atmospheric temperature inversions since it may cause large deviations from the truth. For the current work, estimates of T_{mr} were obtained from a collection of over 15,000 soundings from Wallops Flight Facility in Virginia. The absorption coefficient was determined as $\alpha = k_{H_2O} + k_{O_2}$ using equations 79 and 81 where k_{H_2O} and k_{O_2} are the specific absorptions in $dBkm^{-1}$ for water vapor and oxygen respectively. These expressions have been widely used throughout the remote sensing community and can be found in Waters (1976); Rosenkranz (1975); Ulaby et al. (1981); Iguchi et al. (2010). The ensemble of soundings spans approximately twenty years, 1996 to 2016, of twice daily launches obtained in NetCDF format from <http://esrl.noaa.gov/raobs/>. Figure 5.14 shows the estimates derived from the soundings near zenith at the D3R passive channel frequencies. Note that the standard deviation is lowest during the summer (Ku 4.8K, Ka 4.2K) and increases during the spring (Ku 10.8K, Ka 10.4K), fall (Ku 12.6K, Ka 12.1) and winter (Ku 11.1K, Ka 10.9K) seasons. Soundings were thresholded based on height information content. Profiles without data within 0.2 to 8 km heights were discarded as the tropospheric layer is assumed to have the majority of water vapor and oxygen and therefore contribute the most to T_{mr} . On the other hand, soundings with layers of air saturated with water vapor were also discarded. This was done by applying a threshold based on the dew point depression defined as $t_p - t_d$, where t_p and t_d are the physical and dew point temperatures from the sounding respectively. Regarding the seasonal variability, the increase may be due to precipitation events during soundings. No attempt to discard this type of event from calculations was performed and can be considered as a future step.

The following section describes the application of the tipping curve calibration to the D3R passive channels.

$$(79) \quad k_{H20}(f) = 2f^2 \rho_v \left(\frac{300}{T}\right)^{3/2} \gamma_l \left[\left(\frac{300}{T}\right) e^{-644/T} \frac{1}{(494.4 - f^2)^2 + 4f^2 \gamma_l^2} + 1.2 \times 10^{-6} \right]$$

where f is frequency in GHz, ρ_v is water vapor content in gm^{-3} , γ_l is the parameter line width in GHz and T is temperature in K. Line parameter, γ_l , is given as

$$(80) \quad \gamma_l = 2.85 \left(\frac{P}{1013}\right) \left(\frac{300}{T}\right)^{0.626} \left(1 + 0.018 \frac{\rho_v T}{P}\right)$$

$$(81) \quad k_{O2}(f) = 1.1 \times 10^{-2} f^2 \left(\frac{P}{1013}\right) \left(\frac{300}{T}\right)^2 \gamma \left[\frac{1}{(f - f_0)^2 + \gamma^2} + \frac{1}{f^2 + \gamma^2} \right]$$

where f is frequency in GHz, f_0 , γ is a parameter of line width in GHz and T is temperature in K.

Line parameter γ as follows

$$(82) \quad \gamma = \gamma_0 \left(\frac{P}{1013}\right) \left(\frac{300}{T}\right)^{0.85}$$

where

$$(83) \quad \gamma_0 = \begin{cases} 0.59 & 333 \leq P \text{ (hPa)} \\ 0.59[1 + 3.1 \times 10^{-3}(333 - P)] & 25 \leq P < 333 \text{ (hPa)} \\ 1.18 & P < 25 \text{ (hPa)} \end{cases}$$

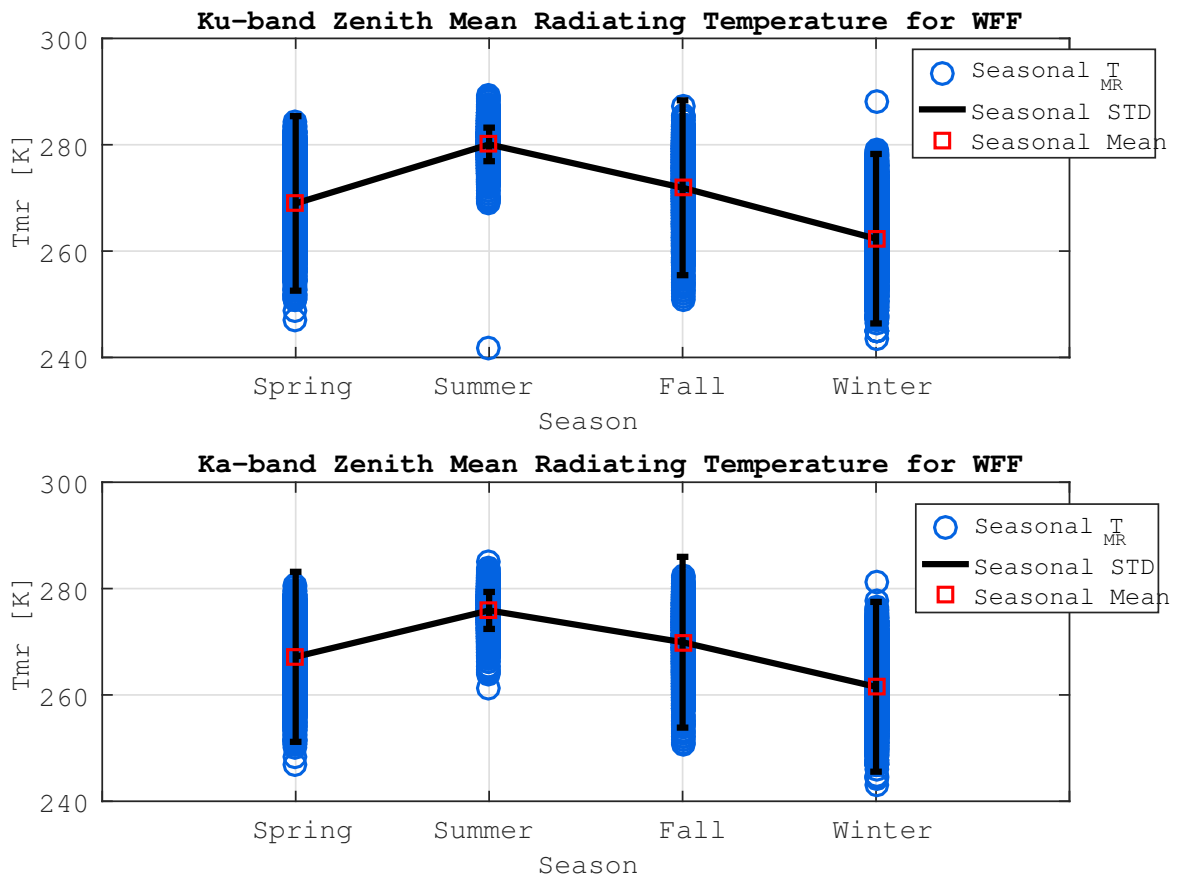


FIGURE 5.14. Seasonal zenith mean radiating temperature T_{mr} from radiosonde soundings at D3R frequencies. Ku-band (top) and Ka-band (bottom). Seasons defined as: spring - March 1st to May31st, summer - June 1st to August 31st, fall - September 1st to November 30th and winter - December 1st to February 28th or 29th.

5.2.2. Tipping curve calibration experiment with the D3R system

The radiative transfer equation for absorptive media and its simplification for a planar stratified atmosphere were explained in the previous section within the context of the tipping curve calibration method. In this section, the focus shifts towards implementation of the method using the D3R passive channels.

Recently, the D3R scan control software was updated to collect observations with dwell times in the order of seconds. The antenna pointing can be set by vectors of azimuth and elevation followed by dwell time, in seconds, for all pairs of angles. This update is intended to enable calibration of the passive channels at Ku and Ka-band using the tipping curve method and operations in a profiling mode. The experiment was run while deployed at WFF during April 2016. The system ran for approximately 44 hours collecting data at 7 elevations corresponding to airmass 1.5 to 3.0 in 0.25 intervals for a total of 358 scans. Figure 5.15 shows a visible image indicating very low cloud coverage near the deployment site within the Delmarva peninsula.

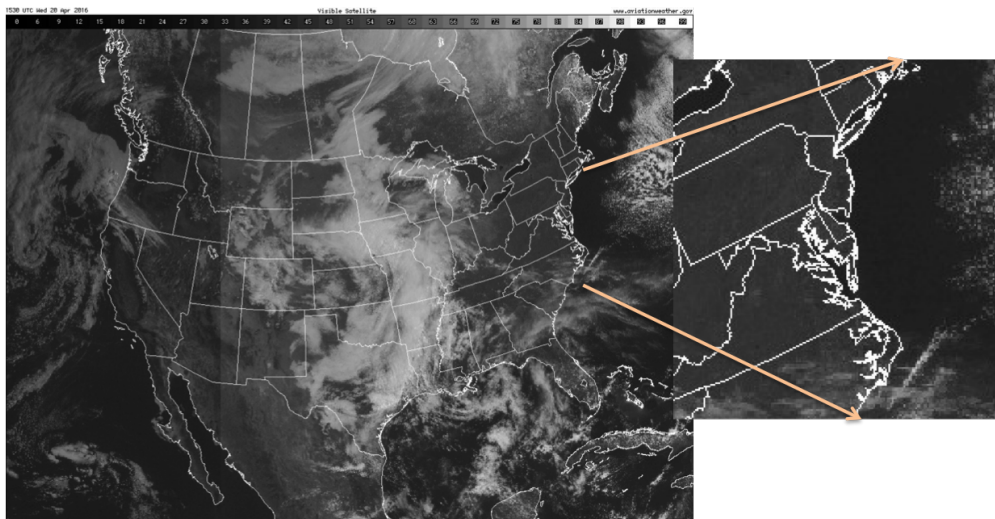


FIGURE 5.15. GOES-13 or East visible image for April 20th, 2016 at 16:00 UTC.

Since the D3R system was primarily designed as a radar system, precision thermal control of the RF front-end and antennas was not a primary goal. Furthermore, given the antenna diameters

(i.e. 1.8 and 0.7 m), volume scanning requirement and slip-ring size limitations, thermal control of all components was impractical. This is a major difference when compared to typical radiometer systems, which typically employ various layers of insulation coupled with tight temperature control of the majority of system components. In an attempt to overcome this, temperature measurements of key components such as the antenna feeds, LNAs, noise sources and mounting plate temperatures are measured and recorded with a period of approximately 5 seconds. Figure 5.16 shows the three thermal zones related to the transceiver system. The antennas and portions of the waveguides are exposed to ambient temperatures within thermal zone 1 (green in figure 5.16), the receiver and transmitter front-ends are enclosed together and mounted to a quarter inch aluminum plate within thermal zone 2 (red in in figure 5.16). This enclosure drifts with ambient temperature as denoted by component temperatures shown in 5.17. Finally, thermal zone 3 (blue in figure 5.16) houses the IF electronics and its temperature if controlled by a pair of 1,500 BTU thermoelectric coolers.

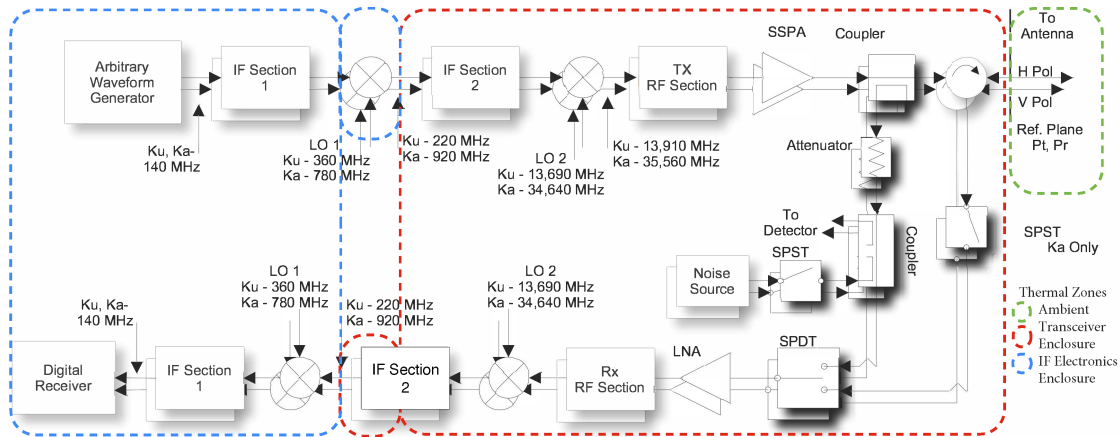
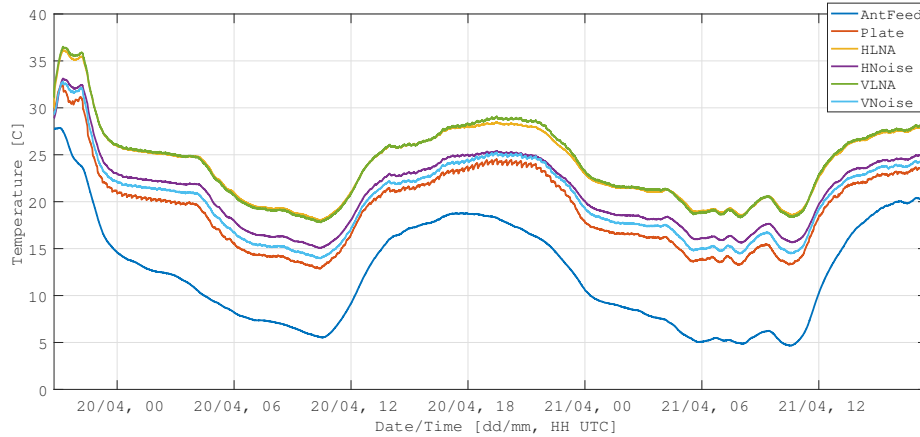


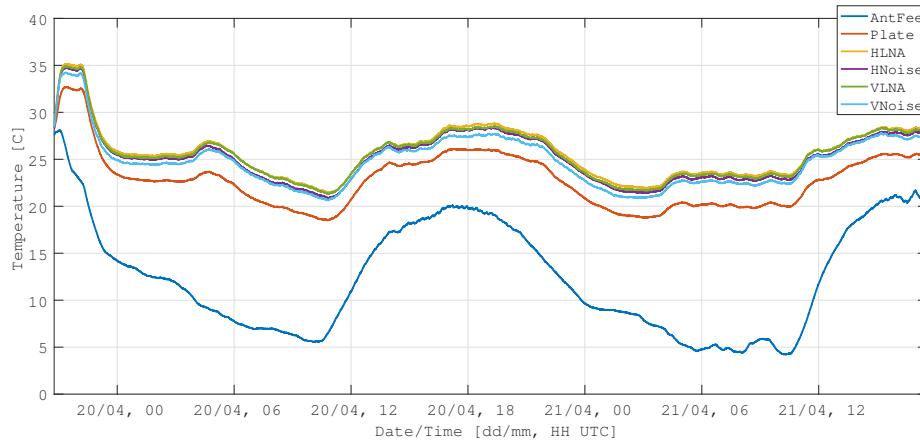
FIGURE 5.16. D3R transceiver system thermal zones.

Since the system is expected to drift with ambient conditions, the goal is to use system temperatures together with calibration coefficients obtained from the tip curve calibration method to define a calibration function that can be applied during operations. Figure 5.17 shows the measured system temperatures during the passive calibration experiment. Note how the component temperatures

track ambient temperature (taken as the antenna feed readings). The range of ambient temperatures during the experiment was 4.7 to 27.9 C (23.2 C range). In a sense, the environment served as a thermal chamber for the whole system.



(A)



(B)

FIGURE 5.17. Ku (A) and Ka-band (B) RF front-end component temperatures during tipping curve calibration experiment at WFF April, 2016.

Given the receiver architecture employed on the D3R system (i.e. total power with noise injection, see figure 5.16), the following system radiometer equation was used to compute uncalibrated antenna temperature estimates, T_u .

$$(84) \quad T_u = \frac{T_{out}}{G_{rec}\Delta G_{rec}} - T_{rec}$$

where T_{out} is the output temperature estimated as power estimates from the autocorrelation lag 0 of digitizer samples VV^* , where $*$ denotes complex conjugation, scaled by $(kB)^{-1}$ (k is Boltzmann's constant and B is the system bandwidth), G_{rec} and ΔG_{rec} are the receiver gain and gain drift estimates, respectively. Finally, T_{rec} is the receiver temperature estimated from the receiver noise figure as $(F-1)T_0$. The receiver gain drift is estimated from the noise injection ratio $T_{nd}T_{ndc}^{-1}$ where T_{nd} is the noise diode (or noise source) temperature and T_{ndc} is the noise diode temperature at receiver gain calibration. In other words, the noise injection values serve as gain drift estimates. Note that equation 84 is expected to yield an uncalibrated estimate of T_a since the receiver temperature T_{rec} and gain G_{rec} are obtained through laboratory measurements not necessarily representative of field conditions, thus termed T_u .

To perform the calibration, each scan was processed to compute the uncalibrated antenna estimate T_u using equation 84. Once this process was completed, the calculation of opacity $\tau(\theta)$ followed. During this step, it was noticed that some values of T_u were greater than the mean radiating temperature T_{mr} therefore causing the opacity values to be complex due to the natural logarithm in the calculation (see equation 77). To overcome this, T_u was scaled down so that all uncalibrated temperatures did not exceed T_{mr} . At this point, a linear least squares fit was performed to each scan. The uncalibrated opacity vector for each scan was defined as $\tau_{\mathbf{u}} = [\tau_u(\theta_1), \tau_u(\theta_2), \dots, \tau_u(\theta_n)]^t$ where n in our case was equal to 7 airmass values for different zenith angles θ used for each fit. The design matrix \mathbf{A} containing the airmass values in the first column as $a(\theta_n) = [sec(\theta_1), sec(\theta_2), \dots, sec(\theta_n)]^t$ and second column vector of ones. With these defined, the linear fit coefficient vector $\beta = [a_1, a_2]^t$ was determined as

$$(85) \quad \beta = (\mathbf{A}^t \mathbf{A})^{-1} \mathbf{A}^t \tau_{\mathbf{u}}$$

Once the linear fits were performed, the coefficient vector β was used to evaluate the linear model down to airmass $a = [-1, 0]$. Airmass equal to -1 was only computed for ease of reading plots. Figure 5.18 illustrates the goodness of fit parameter R^2 and root mean square error (RMSE) for each of the scans performed for the Ku and Ka-band H and V channels. Note that on average the RMSE was about 2.8 degrees for both systems. This may be improved in the future by using a larger channel bandwidth. In some cases the RMSE spiked due to unknown reasons. Results for these were filtered out by applying a threshold on R^2 of 0.92 and 0.97 for the Ku and Ka respectively. Next the uncalibrated antenna temperatures T_u were adjusted by adding a calibration offset r until the zero airmass opacity from each fit was $\leq 10^{-4}$. The vector of calibration factors was defined as $\mathbf{r} = [r_1, r_2, \dots, r_n]^t$ where $r_1 = T_{b0} - (\min(T_u - 0.5))$ and $r_n = T_{mr} - \max(T_u)$ and step resolution of approximately 0.1 degrees.

Figure 5.19 shows the retrieved calibration factors for the Ku and Ka-band H and V polarized channels. A median filter with a six sample window corresponding to approximately 1 minute in time was applied for ease of visualization of the trend. The Ku-band Vpol channel appears to have some instability denoted by the sharp gradient between 4/21 00 hr and 4/21 04 hr. These may be caused by faulty components in the receiver chain. Typically these are caused thermal expansion and contraction within the components as not all materials have matching coefficients of thermal expansion (CTE). The Ka-band shows a somewhat consistent behavior between the H and V pol channels.

As verification of the calibration results, histograms of the corrected antenna temperatures were created. Both H and V pol channels should match since clear skies are a source of unpolarized

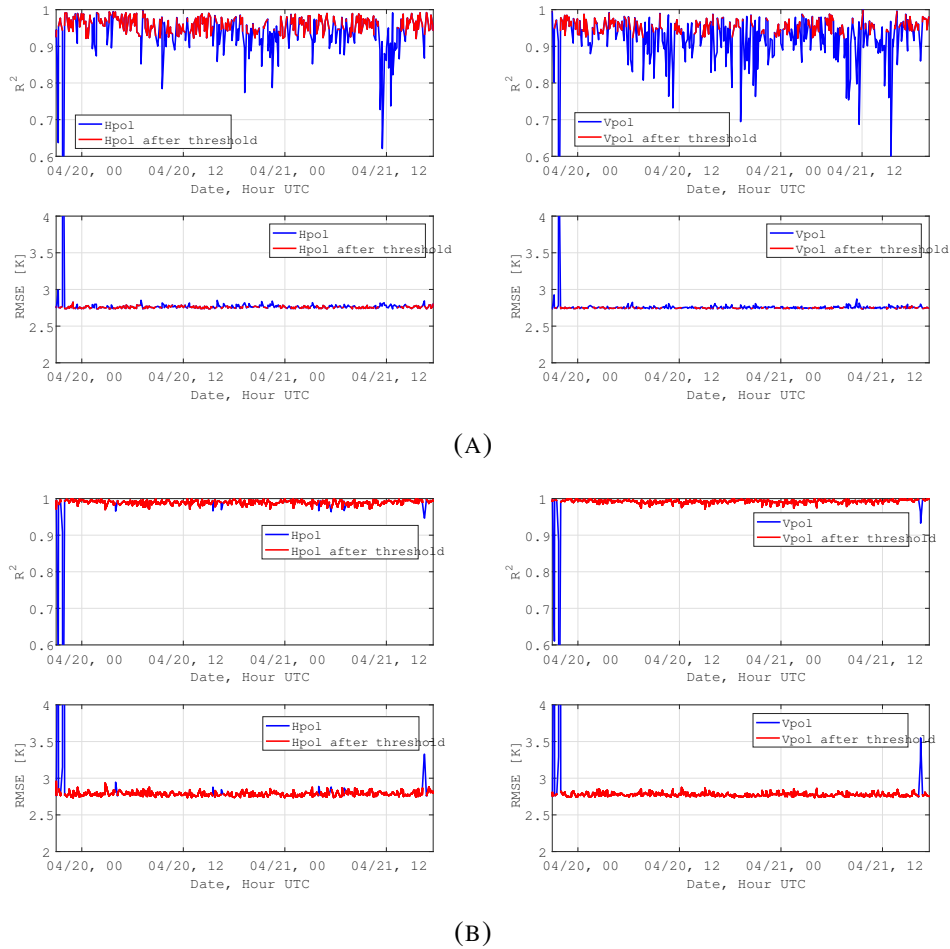
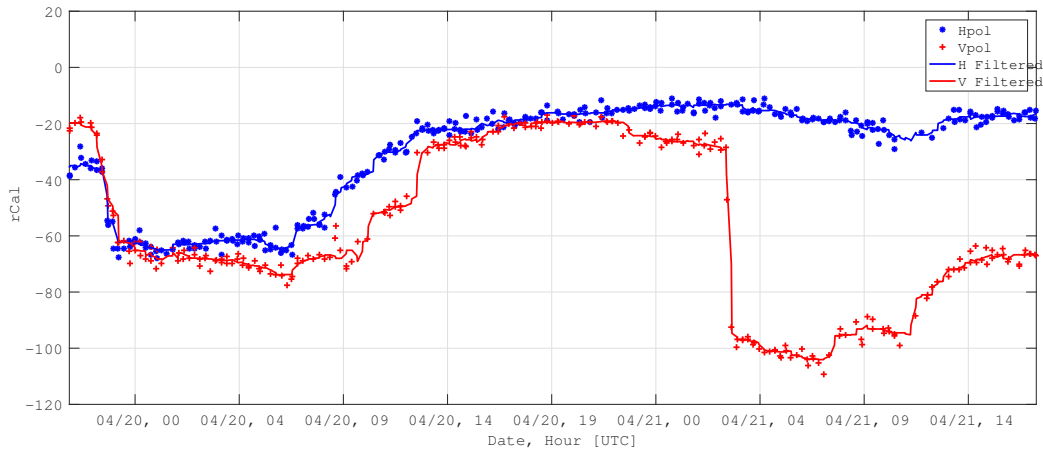


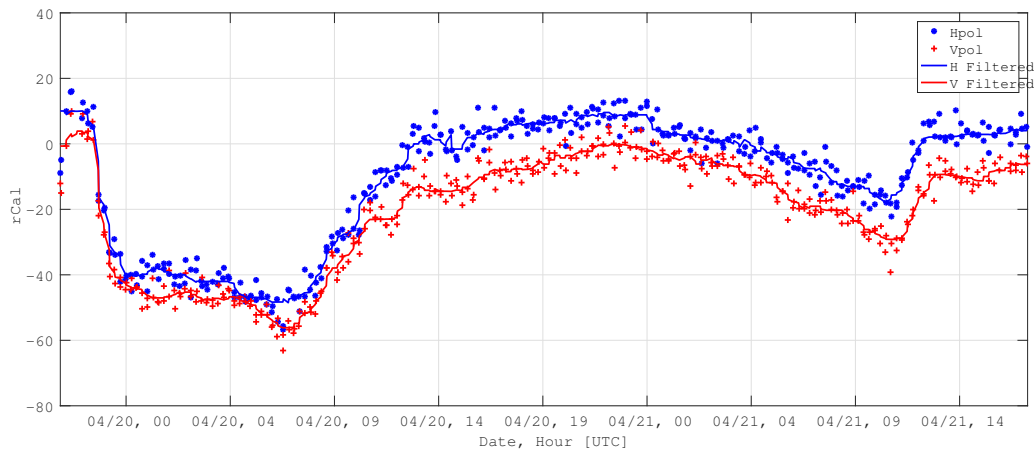
FIGURE 5.18. Ku (A) and Ka-band (B) H and V polarized channel linear fit parameters derived from tipping curve calibration experiment at WFF April, 2016.

radiation. Figure 5.20 shows the histograms with fits assuming a gamma distribution. From these the difference between the mean of each polarization channel was estimated to be 2.05 K and -1.25 K for the Ku and Ka systems respectively. These values are reasonable considering the bandwidth, thermal drift and antennas being used. Nonetheless, they confirm the calibration process appears to be working in a relative sense.

Finally, the absolute calibration was verified by comparing the Ku and Ka-band brightness temperatures with values computed from atmospheric soundings. Fortunately, WFF is an official sounding station and radiosondes are launched twice a day at 00 and 12Z. A total of four soundings were within the calibration experiment period. Figure 5.21 illustrates the results. The RMSE was



(A)



(B)

FIGURE 5.19. Ku (A) and Ka-band (B) H and V polarized channel calibration functions, $r_H(t)$ and $r_V(t)$, derived from tipping curve calibration experiment at WFF April, 2016.

found to be 8.97 K and 6.60 K for Ku and Ka respectively. This serves as proof the calibration process was successful once again considering system limitations. Note how the Ku-band brightness temperatures are in general lower since it isn't as sensitive to water vapor as the Ka-band. Ku-band is typically used as a rain channel. The Ka-band shows evidence of a possible increase in water vapor towards the end. A rain event followed this period about 22 hours after the end.

Since the calibration of the passive channels can only be performed under clear skies and the system calibration will drift with temperature, a neural network using Bayesian regularization with

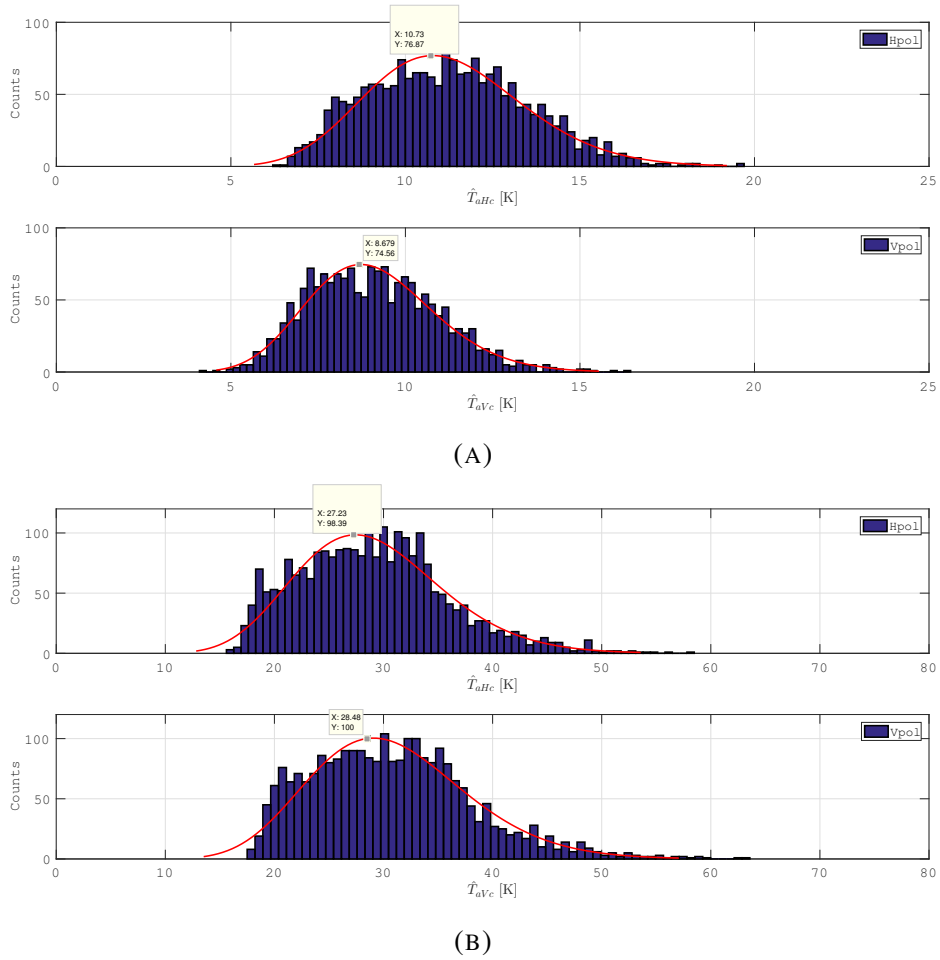
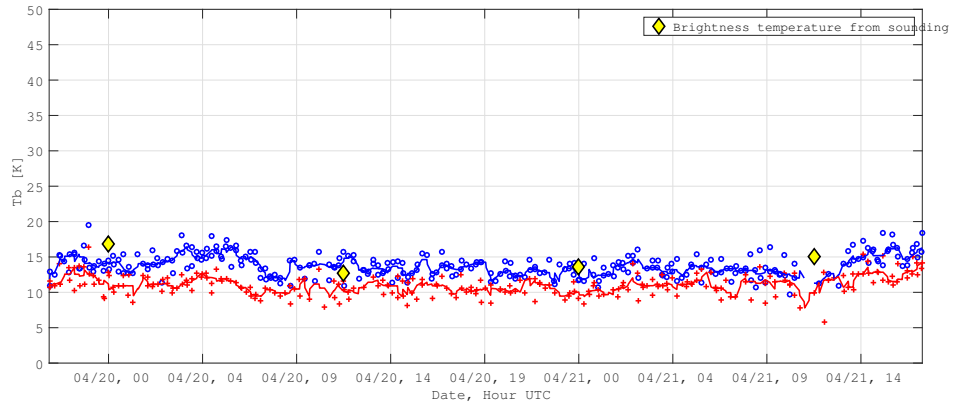


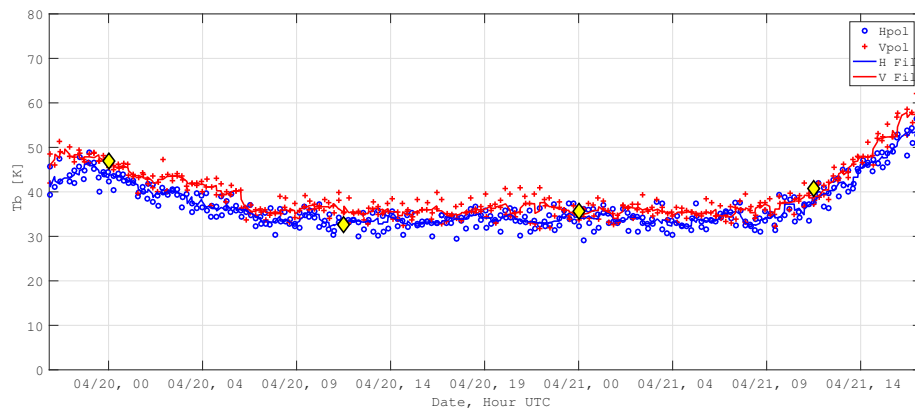
FIGURE 5.20. Ku (A) and Ka-band (B) H and V polarized channel brightness temperatures after calibration.

8 inputs, 40 hidden layers and 2 outputs was trained using the calibration dataset retrieved from the tipping scans and used to predict the calibration factor vectors outside of clear conditions. The inputs were the system temperatures, the target functions were the calibration factor vectors \mathbf{r} for each polarization.

Figures 5.23, 5.24, 5.26, 5.25 and 5.22 show plots of simultaneous active/passive, dual-polarized measurements from the D3R as well as the range of system temperatures throughout the event. Note the correspondence between radar derived parameters (Z , DFR_m and ϕ_{dp}) and brightness temperatures.

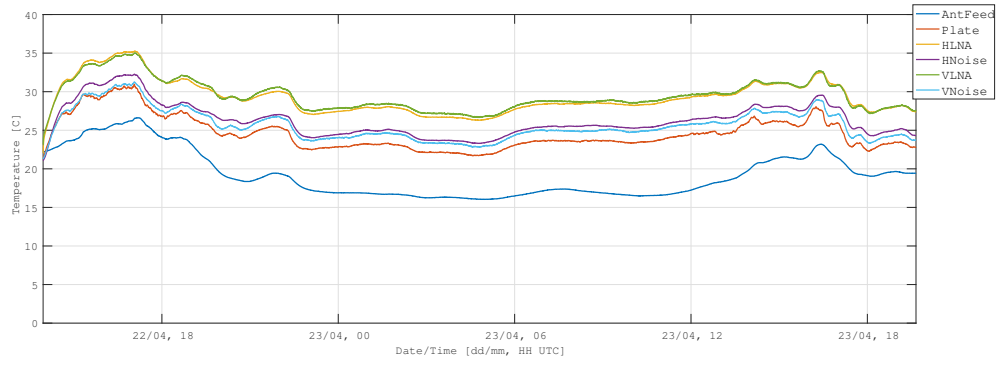


(A)

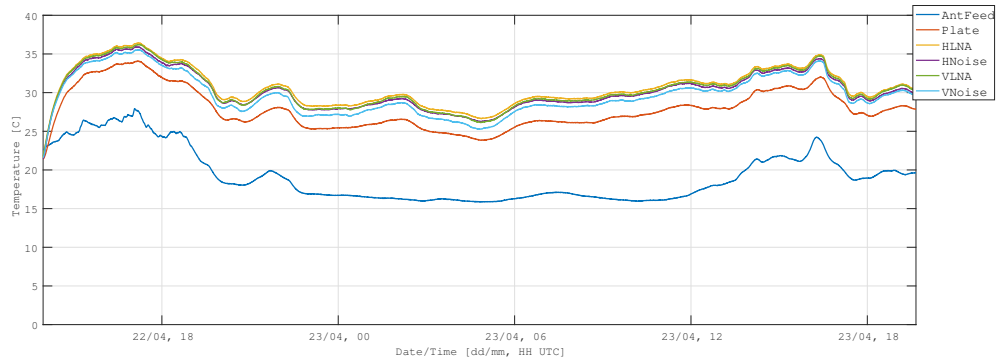


(B)

FIGURE 5.21. Ku (A) and Ka-band (B) H and V polarized channel calibrated brightness temperatures derived from tipping curve calibration experiment at WFF April, 2016.



(A)



(B)

FIGURE 5.22. Ku (A) and Ka-band (B) RF front-end component temperatures during April 22-23rd, 2016 event.

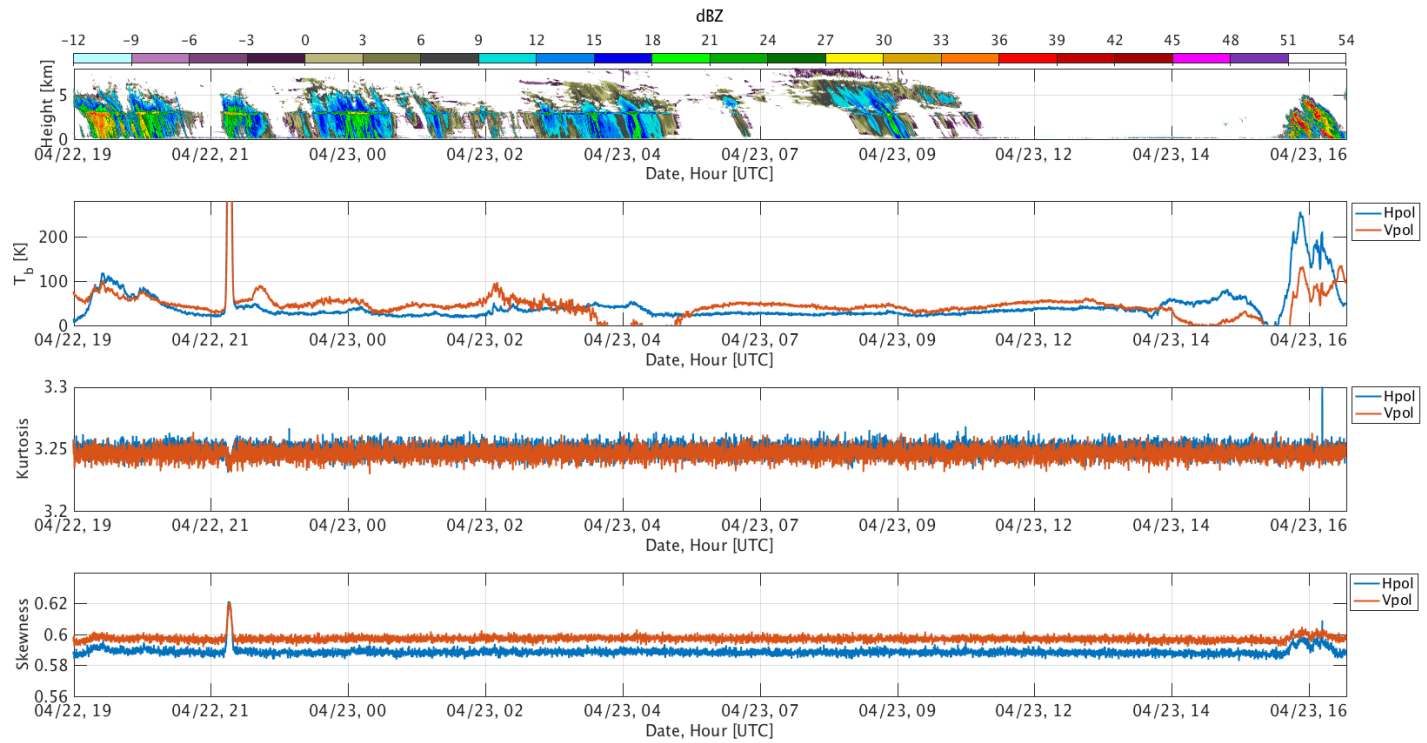


FIGURE 5.23. Ku reflectivity, H and V polarized brightness temperatures, kurtosis and skewness for April 22-23rd, 2016 case. Passive channel calibration function derived from system temperatures and neural network.

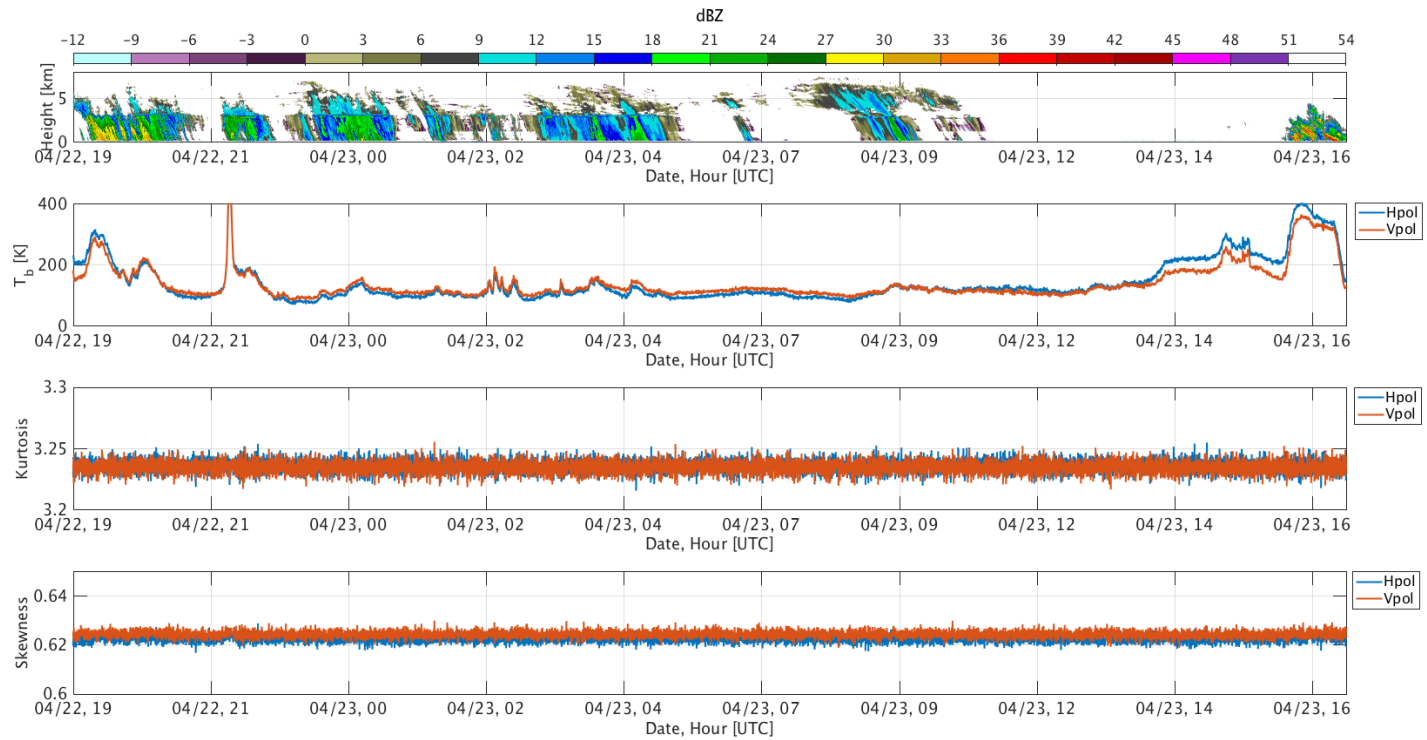


FIGURE 5.24. Ka reflectivity, H and V polarized brightness temperatures, kurtosis and skewness for April 22-23rd, 2016 case. Passive channel calibration function derived from system temperatures and neural network.

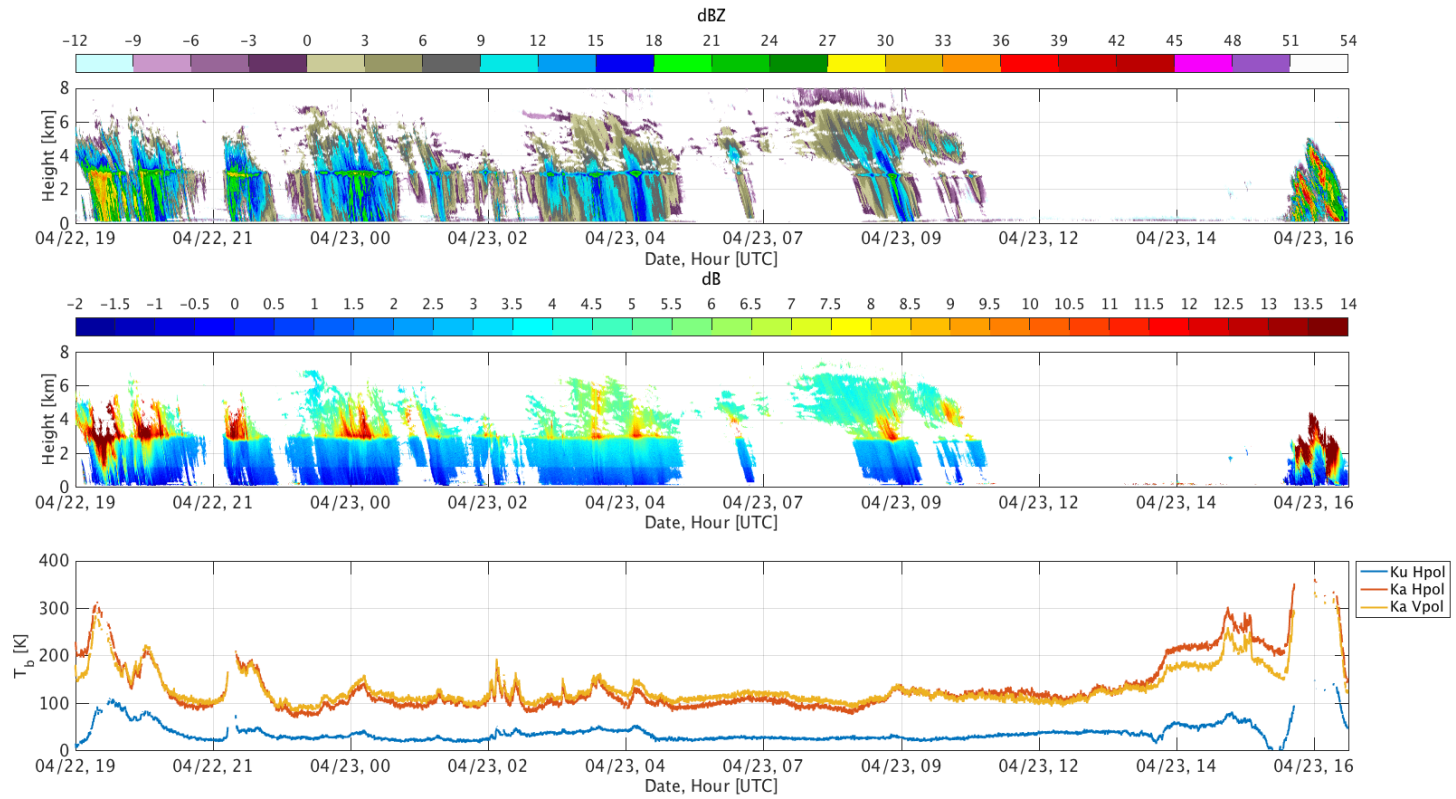


FIGURE 5.25. Ku reflectivity, measured dual-frequency ratio (DFRm), Ku H and Ka HV polarized brightness temperatures for April 22-23rd, 2016 case.

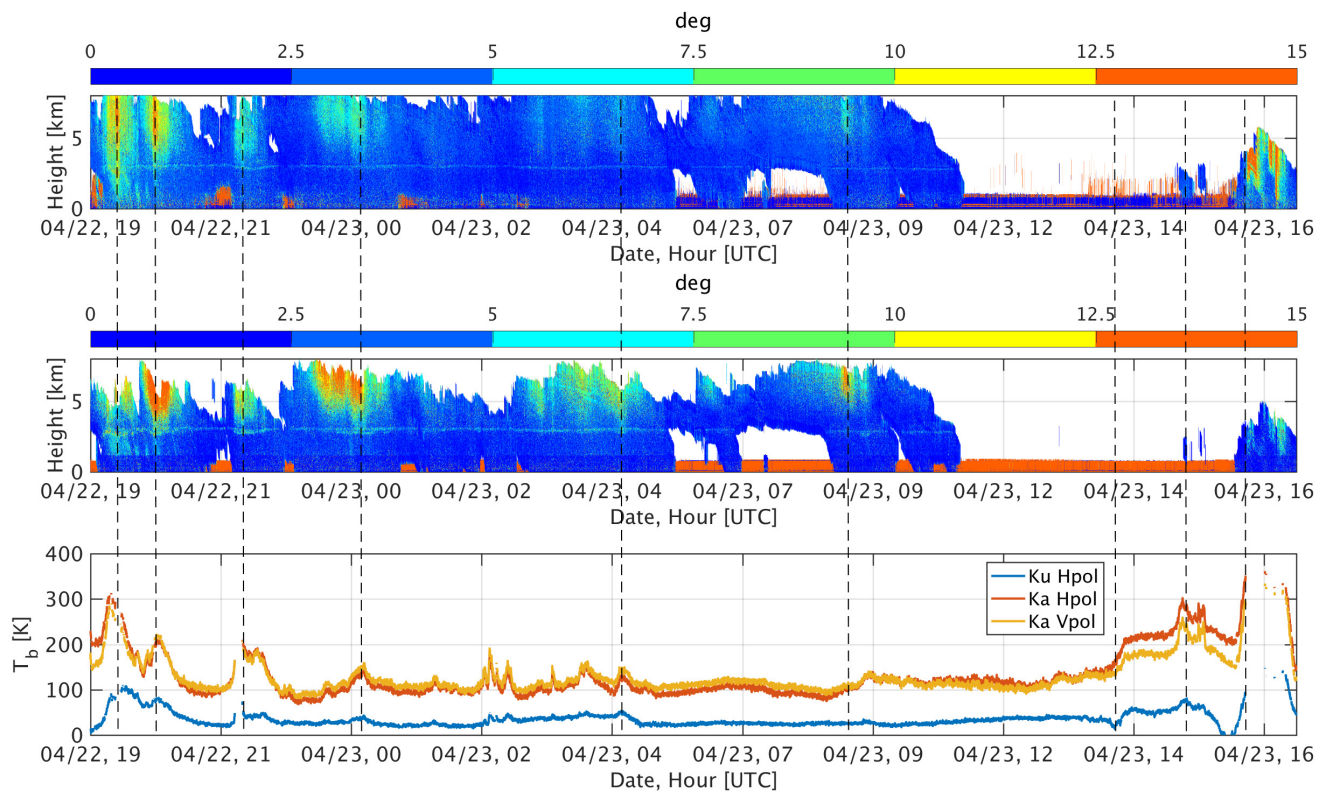


FIGURE 5.26. Ku, and Ka differential phase and Ku H and Ka HV polarized brightness temperatures for April 22-23rd, 2016 case.

CHAPTER 6

SUMMARY, CONCLUSIONS AND FUTURE WORK

6.1. SUMMARY AND CONCLUSIONS

As described in chapter 1, the focus of this work was 1) engineering aspects in the design of an active/passive remote sensing platform, 2) the design of a solid-state, dual-polarized, multi-frequency, Doppler radar system and performance characterization and 3) calibration approach for a ground based, multi-frequency, radar/radiometer system and first calibrated observations in this mode of operation.

Engineering aspects in the design of a combined active/passive platform were covered in chapter 3. The effects of antenna beam and radiation efficiency were discussed and estimated for the D3R antennas. Given the nature of the definition of beam efficiency, the antenna patterns were modeled and high resolution patterns were generated to estimate beam efficiencies. Beam efficiencies of 78.5% and 85.1% were calculated for the Ku and Ka antennas respectively.

The design of the D3R system in support of GPM GV was presented in chapter 4. Salient features of the design and measurement capabilities were discussed along with discussions on reasoning for design choices. Calibration approach was explained and results shown. Absolute calibration was found to be within ± 0.5 dB. Finally, sample observations were presented along with validation on the performance of measured fields. These showed good agreement with theoretical expressions provided in [Bringi and Chandrasekar \(2001\)](#).

Radar calibration results using an alternative approach to the free flying balloon carrying a metallic sphere was presented in chapter 5. Results were validated using snow observations of DFRm and found to be within ± 0.5 dB. The tipping curve calibration method was applied to the passive channels over a period of 44 hours and widely varying ambient temperatures. During this

process, it was discovered that the Ku-band Vpol receiver is unstable and showed large gradients of ≈ 0.7 dB. A neural network approach was employed in the prediction of the system calibration function using measured temperatures from the antennas and receiver front-end components. Finally, sample observations applying the neural network correction were presented. These showed that in some cases the calibration offset was drastically underestimated in the Ku-band.

Regarding what frequencies that could be added to gain sensitivity to water vapor and CLW, one could add an additional radiometer at K-band which is within the peak of the water vapor absorption line. However, another frequency (Ka) possibly two (Ku, Ka) would still be required to separate contributions by water vapor, rain and cloud liquid water contributions (Saavedra et al. (2012)). In this work, the approach taken was to attempt the implementation of Ku/Ka-band active/passive, dual-polarized measurements using a completely shared system therefore leaving room for future additions. This combination by itself does provide sensitivity to water in all three of its states. The opportunity arose from the implementation of the D3R system using solid-state transmitters coupled with a multi-frequency digital waveform and receiving subsystem. Being a solid-state design, the risk of interference from backscatter from the active channels or EMI within the system is lowered since peak powers are greatly reduced through the use of waveform compression techniques and no high voltage electronics are required. The architecture is comprised of dual-receivers for H and V polarizations at both frequency bands. The radiometer mode was implemented using noise injection which is commonly used in radar systems as well for receiver gain monitoring.

From the passive perspective, the sub-channel bandwidth is one of the largest limitations encountered. The available bandwidth used in the current implementation was only 1 MHz. This in turn translates to a small number of independent samples and therefore poor sensitivity when compared to a traditional radiometer system using tens to hundreds of MHz bandwidth. The estimated

sensitivity obtained from the tipping calibration dataset was ≈ 2.8 K for both systems while using 8 seconds of integration at each elevation. Due to the high integration times required, no scanning was attempted or deemed possible with the current configuration.

6.2. FUTURE WORK

The addition of passive measurements to the already existing Ku and Ka-band radars represents a unique capability since the radar is capable of estimating rain liquid water content and the passive measurements would be sensitive to rain, water vapor and CLW. On the other hand, coincident active/passive measurements of snow could also prove useful in the detection of super-cooled water droplets which may not be detectable through backscatter by the radar. For light rain cases, brightness temperatures could easily be used to provide path integrated attenuation (PIA) estimates which could be compared to PIA estimates from differential phase. This may show differences caused by water vapor and CLW through the propagation path.

However, a few steps to improve the quality of the passive data are required. First, the passive sub-channel bandwidth should be increased as much as possible. This will require a trade between the radar occupied bandwidth if simultaneous measurements are desired or time division for sequential active/passive measurements. Second, the Ku-band Vpol channel instability needs to be investigated and repaired. Third, more temperature measurements throughout the system could help improve generalization performance on the neural network approach. Fourth, an attempt to stabilize front-end components or at least slow down drifting with ambient conditions would reduce the corrections needed to maintain calibration. Fifth, a single split noise source (correlated noise source) would improve tracking of the differential drift between receivers.

BIBLIOGRAPHY

- Allan, D. W., 1966: Statistics of Atomic Frequency Standards. *Proceedings of the IEEE*, **54**, 221–230.
- Baldini, L., V. Chandrasekar, and D. Moiseev, 2012: Microwave radar signatures of precipitation from s band to ka band: Application to gpm mission. *European Journal of Remote Sensing*, **45**, 75–88, doi:10.5721/EuJRS20124508.
URL <http://www.aitjournal.com/articleView.aspx?ID=525>
- Barnes, J. A., S. Member, A. R. Chi, S. Member, L. S. Cutler, J. A. Mullen, S. Member, W. L. Smith, R. L. Sydnor, R. F. C. Vessot, and G. M. R. Winkler, 1971: Characterization of Frequency Stability. *IEEE Transactions on Instrumentation and Measurement*, **IM-20**, 105–120.
- Bharadwaj, N. and V. Chandrasekar, 2012: Wideband Waveform Design Principles for Solid-State Weather Radars. *Journal of Atmospheric and Oceanic Technology*, **29**, 14–31, doi:10.1175/JTECH-D-11-00030.1.
URL <http://journals.ametsoc.org/doi/abs/10.1175/JTECH-D-11-00030.1>
- Bharadwaj, N., K. Widener, A. Lindenmaier, and V. Venkatesh, 2011: Calibration System for ARM Radars. *AMS Radar Conference 2011*.
- Born, M. and E. Wolf, 2002: *Principles of Optics*. Cambridge University Press, Cambridge, 7th (expanded) edition.
- Bringi, V. N. and V. Chandrasekar, 2001: *Polarimetric Doppler Weather Radar: Principles and Applications*. Cambridge University Press, 636 pp.
- Camps, A. and J. M. Tarongí, 2010: Microwave Radiometer Resolution Optimization Using Variable Observation Times. *Remote Sensing*, **2**, 1826–1843, doi:10.3390/rs2071826.
URL <http://www.mdpi.com/2072-4292/2/7/1826/>

- Carswell, J., S. Bidwell, and R. Meneghini, 2008: A novel solid-state, dual-polarized, dual-wavelength precipitation doppler radar/radiometer. *International Geoscience and Remote Sensing Symposium (IGARSS)*, number 508, 1014–1017.
- Chandrasekar, V., L. Baldini, N. Bharadwaj, and P. Smith, 2013: *AMS Short Course on Weather Radar Calibration*. American Meteorological Society.
- Chandrasekar, V. and N. Bharadwaj, 2010: *Principles of Waveform Diversity and Design*, SciTech Publishing Inc., Raleigh, NC, chapter 20. 357–393.
- Chandrasekar, V., Y.-G. Cho, D. Brunkow, and A. Jayasumana, 2005: Virtual CSU-CHILL Radar : The VCHILL. *Journal of Atmospheric and Oceanic Technology*, 979–987.
- Chandrasekar, V. and J. Keeler, 1993: Antenna pattern analysis and measurements for multiparameter radars. *Journal of atmospheric and oceanic technology*, **10**, 674–683.
- Chandrasekar, V., M. Schwaller, M. Vega, J. Carswell, K. V. Mishra, A. Steinberg, C. Nguyen, M. Le, J. Hardin, F. Junyent, and J. George, 2012: Dual-frequency dual-polarized doppler radar (d3r) system for gpm ground validation: Update and recent field observations. *International Geoscience and Remote Sensing Symposium (IGARSS)*, Ieee, 346–349.
- URL <http://ieeexplore.ieee.org/lpdocs/epic03/wrapper.htm?arnumber=6351567>
- Chandrasekhar, S., 1960: *Radiative Transfer*. Dover Publications, Inc.
- Doviak, R. J. and D. Zrnicek, 2006: *Doppler Radar and Weather Observations*. Dover Publications, Inc, Mineola, New York, 2nd edition.
- Duffy, G., S. W. Nesbitt, G. M. McFarquhar, M. Poellot, C. V. Chandrasekar, and D. R. Hudak, 2013: In Situ Microphysical and Scattering Properties of Falling Snow in GPM-GCPEX. *AGU Fall Meeting Abstracts*, A5.

- Durden, S. L., E. Im, F. K. Li, A. Ricketts, A. Tanner, and W. Wilson, 1994: ARMAR: An Airborne Rain-Mapping Radar. *Journal of Atmospheric and Oceanic Technology*, **11**, 727–737.
- Farrar, S. and W. L. Jones, 2012: Preliminary analysis of the aquarius/sac-d microwave radiometer (mwr) antenna temperature: Possible antenna pattern issue. *Southeastcon*, IEEE, 1–4.
- Gasiewski, A. J., 1993: *Atmospheric Remote Sensing by Microwave Radiometry*, John Wiley & Sons, chapter 3. 91–144.
- Golestani, Y., V. Chandrasekar, and J. Keeler, 1995: Dual Polarized Staggered PRT Scheme for Weather Radars: Analysis and Applications. *IEEE Transactions on Geoscience and Remote Sensing*, **33**.
- Greco, M. and E. N. Anagnostou, 2008: Combined radar – radiometer retrievals from satellite observations. *Precipitation: Advances in Measurement, Estimation and Prediction*, S. Michaelides, ed., chapter 9, 219–228.
- Greco, M. and W. S. Olson, 2008: Precipitating Snow Retrievals from Combined Airborne Cloud Radar and Millimeter-Wave Radiometer Observations. *Journal of Applied Meteorology and Climatology*, **47**, 1634–1650, doi:10.1175/2007JAMC1728.1.
- URL <http://journals.ametsoc.org/doi/abs/10.1175/2007JAMC1728.1>
- Han, Y. and E. R. Westwater, 2000: Analysis and Improvement of Tipping Calibration for Ground-Based Microwave Radiometers. *IEEE Transactions on Geoscience and Remote Sensing*, **38**, 1260–1276.
- Hou, A. Y., G. Skofronick-Jackson, C. D. Kummerow, and J. M. Shepherd, 2008: Global precipitation measurement. *Precipitation: Advances in Measurement, Estimation and Prediction*, S. Michaelides, ed., Springer, chapter 6, 131–164.
- Iguchi, T., S. Seto, R. Meneghini, N. Yoshida, J. Awaka, and T. Kubota, 2010: GPM/DPR Level-2 Algorithm Theoretical Basis Document. Technical Report December.

- Iturbide-Sanchez, F., S. C. Reising, and S. Padmanabhan, 2007: A Miniaturized Spectrometer Radiometer Based on MMIC Technology for Tropospheric Water Vapor Profiling. *IEEE Transactions on Geoscience and Remote Sensing*, **45**, 2181–2194.
- Jansenn, M. A., 1993: *Atmospheric Remote Sensing by Microwave Radiometry*, John Wiley & Sons.
- Kneifel, S., A. von Lerber, J. Tiira, D. Moisseev, P. Kollias, and J. Leinonen, 2015: Observed relations between snowfall microphysics and triple-frequency radar measurements. *Journal of Geophysical Research: Atmospheres*, 6034–6055, doi:10.1002/2015JD023156.
URL <http://doi.wiley.com/10.1002/2015JD023156>
- Land, D., A. Levick, and J. Whand, 2010: The use of the Allan deviation for the measurement of the noise and drift performance of microwave radiometers. *Measurement Science and Technology*, **18**, 1917–1928, doi:10.1088/0957-0233/18/7/018.
URL <http://eprints.gla.ac.uk/28720/>
- Le, M. and V. Chandrasekar, 2014: An Algorithm for Drop-Size Distribution Retrieval From GPM Dual-Frequency Precipitation Radar. *IEEE Transactions on Geoscience and Remote Sensing*, 1–16, doi:10.1109/TGRS.2014.2308475.
URL <http://ieeexplore.ieee.org/lpdocs/epic03/wrapper.htm?arnumber=6813630>
- Li, L., G. Heymsfield, J. Carswell, D. Schaubert, M. Mclinden, M. Vega, and M. Perrine, 2011: Development of the NASA High-Altitude Imaging Wind and Rain Airborne Profiler. *IEEE Aerospace Conference*, 1–8.
- Liao, L., R. Meneghini, A. Tokay, and L. F. Bliven, 2016: Retrieval of snow properties for Ku- and Ka-band dual-frequency radar. *Journal of Applied Meteorology and Climatology*, **55**, 1845–1858, doi:10.1175/JAMC-D-15-0355.1.

- Marrero, V., 2015a: D3r corner reflector patterns, internal report.
- 2015b: Dual-frequency dual-polarized doppler radar (d3r) global precipitation mission (gpm) antenna model patterns, internal report.
- Marzano, F. S., A. Mugnai, G. Panegrossi, N. Pierdicca, E. A. Smith, J. Turk, and A. Member, 1999: Bayesian Estimation of Precipitating Cloud Parameters from Combined Measurements of Spaceborne Microwave Radiometer and Radar. *IEEE Transactions on Geoscience and Remote Sensing*, **37**, 596–613.
- McLinden, M., P. Siqueira, and N. Majurec, 2008: Calibration of the umass advanced multi-frequency radar (amfr). *International Geoscience and Remote Sensing Symposium (IGARSS)*, 105–108.
- Meneghini, R., T. Kozu, H. Kumagai, and W. C. Boncyk, 1992: A Study on Rain Estimation Methods from Space using Dual-Wavelength Radar Measurements at Near-Nadir Incidence over Ocean. *Journal of Atmospheric and Oceanic Technology*, **9**, 364–382.
- Meneghini, R., H. Kumagai, J. R. Wang, T. Iguchi, and T. Kozu, 1997: Microphysical Retrievals over Stratiform Rain Using Measurements from an Airborne Dual-Wavelength Radar-Radiometer. *IEEE Transactions on Geoscience and Remote Sensing*, **35**, 487–506.
- Moisseev, D. N. and V. Chandrasekar, 2007: Nonparametric estimation of raindrop size distributions from dual-polarization radar spectral observations. *Journal of Atmospheric and Oceanic Technology*, **24**, 1008–1018, doi:10.1175/JTECH2024.1.
- URL <http://journals.ametsoc.org/doi/abs/10.1175/JTECH2024.1>
- Mott, H., 1992: *Antennas for Radar and Communications: A Polarimetric Approach*. John Wiley, New York.
- Mudukutore, A., V. Chandrasekar, and E. A. Mueller, 1995: The differential phase pattern of the csu chill radar antenna. *Journal of Atmospheric and Oceanic Technology*, **12**, 1120–1123.

URL <http://journals.ametsoc.org/doi/abs/10.1175/1520-0426%281995%29012%3C1120%3ATDPPOT%3E2.0.CO%3B2>

Mudukutore, A. S., V. Chandrasekar, and R. J. Keeler, 1998: Pulse Compression for Weather Radars. *IEEE Transactions on Geoscience and Remote Sensing*, **36**, 125–142.

Nguyen, C. and V. Chandrasekar, 2013: Gaussian model adaptive processing in time domain (gmap-td) for weather radars. *Journal of Atmospheric and Oceanic Technology*, **30**, 2571–2584.

Nyquist, H., 1928: Thermal agitation of electric charge in conductors. *Physical Review*, **32**, 110–113.

Olson, W. S., H. Masunaga, and GPM Combined Radar-Radiometer Algorithm Team, 2010: GPM Combined Radar-Radiometer Precipitation Algorithm Theoretical Basis Document (Draft 1). Technical Report Draft 1.

Racette, P. and R. H. Lang, 2005: Radiometer design analysis based upon measurement uncertainty. *Radio Science*, **40**, 1–22, doi:10.1029/2004RS003132.

URL <http://www.agu.org/pubs/crossref/2005/2004RS003132.shtml>

Rosenkranz, P. W., 1975: Shape of the 5 mm oxygen band in the atmosphere. *IEEE Transactions on Antennas and Propagation*, **AP-23**, 498–506.

Saavedra, P., A. Battaglia, and C. Simmer, 2012: Partitioning of cloud water and rainwater content by ground-based observations with the Advanced Microwave Radiometer for Rain Identification (ADMIRARI) in synergy with a micro rain radar. *Journal of Geophysical Research*, **117**, 1–18, doi:10.1029/2011JD016579.

URL <http://www.agu.org/pubs/crossref/2012/2011JD016579.shtml>

Schieder, R., G. Rau, and B. Vowinkel, 1985: Characterization and Measurement of System Stability. *SPIE Instrumentation for Submillimeter Spectroscopy*, **598**, 189–192.

Schreier, P. J. and L. L. Scharf, 2010: *Statistical Signal Processing of Complex-Valued Data: The Theory of Improper and Noncircular Signals*. Cambridge University Press.

Seto, S., T. Iguchi, and T. Oki, 2013: The Basic Performance of a Precipitation Retrieval Algorithm for the Global Precipitation Measurement Mission's Single/Dual-Frequency Radar Measurements. *IEEE Transactions on Geoscience and Remote Sensing*, **51**, 5239–5251, doi:10.1109/TGRS.2012.2231686.

URL <http://ieeexplore.ieee.org/lpdocs/epic03/wrapper.htm?arnumber=6459585>

Siggia, A. D. and R. E. Passarelli, 2004: Gaussian model adaptive processing (gmap) for improved ground clutter cancellation and moment calculation. *European Conference on Radar in Meteorology and Hydrology*, 67–73.

Skofronick-Jackson, G., J. R. Wang, G. M. Heymsfield, R. Hood, W. Manning, R. Meneghini, and J. Weinman, 2003: Combined Radiometer – Radar Microphysical Profile Estimations with Emphasis on High-Frequency Brightness Temperature Observations. *Journal of Applied Meteorology*, **42**, 476–487.

Srivastava, R. C., A. R. Jameson, and P. H. Hildebrand, 1979: Time-Domain Computation of Mean and Variance of Doppler Spectra. *Journal of Applied Meteorology*, **18**, 189–194.

Tiuri, M., 1964: Radio astronomy receivers. *IEEE Transactions on Antennas and Propagation*, **12**, 930–938.

Tragl, K., 1990: Polarimetric radar backscattering from reciprocal random targets. *IEEE Transactions on Geoscience and Remote Sensing*, **28**, 856–864, doi:10.1109/36.58973.

URL <http://ieeexplore.ieee.org/lpdocs/epic03/wrapper.htm?arnumber=58973>

- Tyynelä, J. and V. Chandrasekar, 2014: Characterizing falling snow using multifrequency dual-polarization measurements. *Journal of Geophysical Research: Atmospheres*, **119**, 8268–8283, doi:10.1002/2013JD021369.Received.
- Ulaby, F. T., D. G. Long, W. Blackwell, C. Elachi, A. Fung, C. Ruf, K. Sarabandi, H. Zebker, and J. van Zyl, 2014a: *Microwave Radar and Radiometric Remote Sensing*. University of Michigan Press.
- 2014b: *Microwave Radar and Radiometric Remote Sensing*, University of Michigan Press, chapter 13. 639–641.
- Ulaby, F. T., R. K. Moore, and A. K. Fung, 1981: *Microwave Remote Sensing: Active and Passive*, volume Fundamentals and Radiometry. Artech House.
- Vega, M. A., V. Chandrasekar, J. Carswell, R. M. Beauchamp, M. R. Schwaller, and C. Nguyen, 2014: Salient Features of the Dual-frequency, Dual-polarized, Doppler Radar for Remote Sensing of Precipitation. *Radio Science*, **49**, 1–19, doi:10.1002/2014RS005529.1.
- Vega, M. A., V. Chandrasekar, C. Nguyen, K. V. Mishra, and J. Carswell, 2012: Calibration of the nasa dual-frequency , dual-polarized , doppler radar. *Geoscience and Remote Sensing Symposium (IGARSS)*, volume 2, 4625–4628.
- Wang, Y., V. Chandrasekar, and V. N. Bringi, 2006: Characterization and Evaluation of Hybrid Polarization Observation of Precipitation. *Journal of Atmospheric and Oceanic Technology*, **23**, 552–572, doi:10.1175/JTECH1869.1.
- URL <http://journals.ametsoc.org/doi/abs/10.1175/JTECH1869.1>
- Waters, J., 1976: *Absorption and Emission by Atmospheric Gases*, Elsevier, volume 12, Part B of *Methods in Experimental Physics*, chapter 2.3. 142–176.
- Westwater, E. R., 1993: *Atmospheric Remote Sensing by Microwave Radiometry*, John Wiley & Sons, chapter 4.

Zrnic, D. S. and P. Mahapatra, 1985: Two Methods of Ambiguity Resolution in Pulse Doppler Weather Radars. *IEEE Transactions on Aerospace and Electronic Systems*, 470–483.